



This work is protected by copyright and other intellectual property rights and duplication or sale of all or part is not permitted, except that material may be duplicated by you for research, private study, criticism/review or educational purposes. Electronic or print copies are for your own personal, non-commercial use and shall not be passed to any other individual. No quotation may be published without proper acknowledgement. For any other use, or to quote extensively from the work, permission must be obtained from the copyright holder/s.

Pre-main-sequence populations and young stellar variability in the Large Magellanic Cloud

Viktor Zivkov

Doctor of Philosophy

Faculty of Natural Sciences, Keele University

March 2020

Abstract

Detailed studies of intermediate- and low-mass pre-main-sequence (PMS) stars outside the Galaxy have so far been conducted only for small targeted regions harbouring known star formation complexes. This work presents a comprehensive analysis of the PMS population in a $\sim 1.5 \text{ deg}^2$ area located in the gas-rich Large Magellanic Cloud (LMC). The identification and classification of the populations was achieved by statistical analysis of the $K_s/(Y - K_s)$ colour–magnitude distribution of stars using a PSF photometric source catalogue of the VISTA Survey of the Magellanic Clouds (VMC). The analysis reveals ~ 2260 PMS candidates with ages $\lesssim 10 \text{ Myr}$ and masses $\lesssim 4 M_\odot$. The young populations exhibit non-uniform spatial distributions and appear to be hierarchically organized with large structures containing smaller and denser substructures. Regions containing only intermediate/low-mass PMS stars are more scattered and usually located in the outskirts of star forming complexes. The young populations are clustered along ridges and filaments where dust emission in the far-infrared (FIR) ($70 \mu\text{m} - 500 \mu\text{m}$) is bright. At $70 \mu\text{m}$ and $100 \mu\text{m}$ we report a strong dust emission increase in regions hosting young massive stars, which is less pronounced in regions populated only by less massive ($\lesssim 4 M_\odot$) PMS stars.

In addition, this thesis presents the first systematic variability study of massive young stellar objects (YSOs) in the LMC. By using a χ^2 -analysis on multi-epoch observations obtained by the VMC and my open time programme, stellar variability is identified. 173 high-reliability YSO candidates are selected based on several *Spitzer* studies, out of which 39 displayed variability. They have been classified into eruptive, fader, dipper, short-term variable and long period variable-YSO based on the appearance of their K_s -band lightcurves. The majority of YSO variables are aperiodic; for five YSOs the lightcurves indicate a possible periodicity, identified using a Lomb-Scargle periodogram analysis. The lightcurve shapes and colour shifts can be mostly associated with unsteady accretion or (grey) extinction. Overall, the observed amplitudes are moderate with only two YSOs exhibiting a $\Delta K_s > 1 \text{ mag}$. Eruptive variables tend to

have the largest amplitudes amongst all classes. Compared with similar Galactic studies the amplitudes tend to be smaller, which could be attributed to smaller extinction variations due to the larger gas-to-dust ratio of the LMC.

Acknowledgements

I would like to express my deep gratitude to Joana Oliveira and Monika Petr-Gotzens, my Ph.D. supervisors, for their guidance, encouragement, and useful critiques during this research work. Even during times when they had tightly packed schedules due to teaching and other commitments, they found time and patience to answer my questions and gave me helpful advice about my work. Their feedback and commentary on any manuscript I wrote throughout my time as PhD student was invaluable and improved greatly the quality of the final result.

I spend two years at Keele University and two years at ESO during my PhD work, and I want to thank both institutes for the great conditions offered and for giving me the opportunity to begin this journey.

I would like to offer my special thanks Stefano from the VMC team for providing the catalogues I used in this thesis. His contribution has accelerated this work considerably.

I also want to thank the scientists of the VMC team, which gave me many suggestions in all four annual VMC meetings I participated. They also provided constructive and valuable feedback for my publication, and thus also helped in improving the quality of this thesis.

My special thanks are extended to my fellow students at Keele University, which provided help from programming to comic relief. On this note, I also want to mention my fellow students at the ESO headquarters with which I shared my days during the two years I spend at the ESO headquarters.

Finally, I want to thank my mother for her support not only throughout my PhD, but also for everything that came before. On the occasions I made it back to my home-town in Germany she provided me with more food than I could possibly eat, and with emotional support in case I needed it.

The thesis is dedicated to the memory of my father who helped me to become the person I am.

Contents

Abstract	i
Acknowledgements	iii
1 Introduction	1
1.1 Star formation	1
1.1.1 Conditions for the onset of star formation	1
1.1.2 Early stellar evolution	5
1.1.2.1 Observational identification of young stars	7
1.1.2.2 Massive YSOs	9
1.2 YSO variability	13
1.3 The influence of metallicity	15
1.3.1 Heating and cooling balance	16
1.3.2 Circumstellar discs	17
1.4 The Large Magellanic Cloud	19
1.4.1 Observational studies of young stars in the LMC	20
1.5 Project goals	23
2 Observations and data	25
2.1 Properties of VISTA/VIRCAM	25
2.2 The VMC survey	27
2.3 Tile LMC_7_5	29
2.3.1 Complementary observations of LMC_7_5	32
3 PMS populations in the LMC	33
3.1 Introduction	33
3.2 Constructing differential Hess diagrams	34
3.2.1 CMD density diagrams	34
3.2.2 Control field selection	36
3.2.3 CMD residuals and significance maps	39
3.3 Identifying candidate young regions	41
3.4 Testing the identification strategy	47
3.4.1 Synthetic clusters	47
3.4.2 Literature clusters	52
3.4.3 Final choice of grid element radius	54
3.5 Results	54
3.5.1 Spatial distribution of the young populations	54
3.5.1.1 Global properties	54
3.5.1.2 Individual regions	59
3.5.2 Spatial distribution of the older UMS population	61
3.5.3 Quantitative analysis of the PMS populations	63

3.5.4	Comparison with dust emission maps	66
3.6	Summary and conclusions	69
4	Variability analysis of Young Stellar Objects	72
4.1	Introduction	72
4.2	Multi-epoch catalogue	73
4.2.1	Constructing the multi-epoch catalogue	73
4.2.2	Correcting magnitude offsets	74
4.3	Identifying variable stars using χ^2 -analysis	75
4.4	Analysis of the variable stars	83
4.4.1	General properties	83
4.4.2	Comparison to known samples	87
4.4.3	Periodicity tests	91
4.5	The massive YSO sample	96
4.5.1	<i>Spitzer</i> source selection	97
4.5.2	Matching with VMC catalogues	98
4.5.3	Removing contaminants	100
4.5.3.1	Colour criteria	100
4.5.3.2	Visual examination	102
4.6	Results and discussion	105
4.6.1	Lightcurve classification	105
4.6.1.1	Eruptive	106
4.6.1.2	Fader	107
4.6.1.3	Dipper	109
4.6.1.4	STV	110
4.6.1.5	Not classified	111
4.6.2	YSO periodicity	111
4.6.3	Properties of the variable YSOs	114
4.6.4	Long-term variability and colour analysis	119
4.6.5	Comparison to Galactic studies	120
4.7	Summary and conclusions	123
5	Conclusions, summary and prospects	126
5.1	PMS populations	126
5.2	YSO variability	128
5.3	Future prospects	130
5.4	Beyond the LMC	131
A	Observational epochs	133
	Bibliography	140

List of Figures

1.1	Typical SEDs for the different YSO classes (Schulz 2012)	9
1.2	Schematic representation of the evolution of a low mass star. From http://www-cr.scphys.kyoto-u.ac.jp/research/xray/press200011/figures/	10
1.3	Schematic representation of the early evolution of massive stars (Schulz 2012)	12
1.4	Cooling rates for different coolants (Klessen & Glover 2016). For H ₂ and its deuterated analogue HD a fully molecular gas is assumed, while the C and O abundances are taken from Sembach et al. (2000). The density is assumed to be $n = 1 \text{ cm}^{-3}$ and the values are weighted by the fractional abundance of the coolants relative to H ₂	17
1.5	Three colour LMC mosaic from the SAGE data. The red channel shows the distribution of warm dust, while the blue channel primarily tracks the stellar content. Image taken from Meixner et al. (2006).	22
2.1	Schematic view of the VISTA telescope (Sutherland et al. 2015).	25
2.2	The detector plane of VIRCAM. From http://www.eso.org/sci/facilities/paranal/instruments/vircam/inst.html	27
2.3	Tiling of the VMC area overplotted onto the HI distribution of the Magellanic system (Cioni et al. 2011). The colors of the rectangles indicate when the observations for the corresponding tile started. Blue: start in P85 (1 Nov 2009–31 March 2010); Green: start in P86 (01 April 2009–30 Sep 2010); Red: start after 1 Oct 2010	28
2.4	Digitized Sky Survey (DSS) image showing the location of the LMC_7.5 field within the wider LMC environment. North is up and east is to the left.	30
3.1	VISTA RGB composite with Y ($1.02 \mu\text{m}$) in blue, J ($1.25 \mu\text{m}$) in green, and K_s ($2.15 \mu\text{m}$) in red showing the north-eastern corner of the pilot field. Green crosses are placed at the centres of the grid elements ($90''$ radius in this instance). The small yellow circle highlights an example grid element, while the large white circle shows the area searched to identify suitable control field regions (see text).	36

- 3.2 **Top:** CMDs of two example grid elements. Boxes indicate the UMS and PMS regions used in the control field selection, as well as the RC region used to determine the mean extinction (see Sec. 3.2.2 for details). The slope of the RC selection box is defined by the reddening vector. **Bottom:** Corresponding Hess CMDs. Thin solid lines are PARSEC isochrones (Bressan et al. 2012) for $\log(t/\text{yr}) \in [9.5, 9.6, 9.7, 9.8]$ and $Z = 0.0033$ (left panel), and $\log(t/\text{yr}) \in [6.0, 6.1, 6.2, 6.3, 6.4, 6.5, 6.6, 6.7, 6.8]$ and $Z = 0.008$ (right panel). The assumed metallicities are typical for the age ranges (Rubele et al. 2012; Tatton et al. 2013). The isochrones are shifted by a distance modulus of 18.49 mag (de Grijs, Wicker & Bono 2014), and an extinction correction derived from the RC analysis (see text) is applied. The dotted line marks the typical 50% completeness level. 38
- 3.3 Cumulative colour distribution of RC stars for the grid element under investigation (black line), and for the corresponding control field before and after the reddening correction (blue and red lines, respectively). RC stars are defined by the RC selection box in Fig. 3.2. The intrinsic RC colour adopted is $(Y - K_s)_0 = 0.84$ mag (Tatton et al. 2013). 40
- 3.4 **Top left:** Residual map generated for a grid element showing no significant density excesses, leading to a featureless residual map; such a grid element is thus dominated by the old LMC field population. **Top right:** Residual map for a grid element that includes the OB association LH 63. Significant density excesses can be seen across the CMD, which is due to the presence of massive OB and PMS stars. **Bottom:** Significance map for the same LH 63 region with 25 CMD boxes overlaid; these are used to classify candidate regions based on observed density excesses (see Sec. 3.3). 42
- 3.5 Same significance map in the background as shown in Fig. 3.4 (bottom). Blue and red symbols display VMC sources that are successfully matched to the LH 63 UMS (left) and PMS (right) catalogues from Gouliermis et al. (2011). Thick black lines highlight the boxes relevant for the UMS and PMS classifications, respectively (see also Fig. 3.6). 44

- 3.6 **From left to right:** Significance maps for grid elements classified as UMS-only, PMS-only, UMS+PMS, and “old”. The CMD boxes relevant for each classification are highlighted. Boxes that are flagged in the particular significance map are numbered. PARSEC isochrones (Bressan et al. 2012) are shown in all panels. Red isochrones represent ages from $\log(t/\text{yr}) = 9.6$ to 9.8, with a metallicity of $Z = 0.0033$ (Tatton et al. 2013); they show the typical location of the old LMC field population. Black isochrones represent young populations from $\log(t/\text{yr}) = 6.0$ to 6.8 ($Z = 0.008$; Rubele et al. 2012). The two black isochrones in the rightmost panel represent populations of $\log(t/\text{yr}) = 8.5$ and 8.6 ($Z = 0.008$). All isochrones are reddened according to the mean extinction for that particular grid element (Sect. 3.2.2). In the second panel the theoretical positions for stars of three different masses are shown (colour-coded circles) for the youngest and oldest black isochrones. 46
- 3.7 **Top:** Significance map for a PMS-only classified grid element (left) is compared to a synthetic stellar population of $250 M_{\odot}$ and 1 Myr (right). **Bottom:** Similar to the top, but showing a UMS+PMS classified grid element (left) and a synthetic stellar population of $1000 M_{\odot}$ and 5 Myr (right). Flagged boxes are numbered in each map. 49
- 3.8 **Top panel:** Detection percentages for $500 M_{\odot}$ clusters of different ages for grid-element radii from $90''$ to $40''$. A general increase in detection rates with decreasing radius is noticeable. A decrease in detection rates with increasing cluster age is evident as well. **Bottom panel:** Detection percentages for clusters of four different masses across the age range from 1 Myr to 1 Gyr for the $40''$ radius. A decrease in sensitivity for older ages and lower masses is apparent. Clusters more massive than $500 M_{\odot}$ show high detection rates for young ages. 51
- 3.9 **Top left:** Three-colour composite image with VMC Y (blue) and K_s bands (green), and *Spitzer* IRAC $8.0 \mu\text{m}$ (red). The rectangle shows the region covered by our analysis. Small crosses mark the centres of grid elements for the $40''$ grid that are classified as PMS-only (yellow) or UMS+PMS (cyan). Several prominent regions are highlighted and labelled (spatial sizes according to Bica et al. 2008) and discussed further in Sec. 3.5. **Top right:** Inverted grey-scale map of $\text{H}\alpha$ emission (Smith et al. 2005). **Bottom:** PMS density contours for elements classified as PMS-only or UMS+PMS derived from the residual maps of the grid elements. The outermost contour represents $\Delta n_{\text{PMS}} = 2.4 \text{ stars arcmin}^{-2}$ (see Sec. 3.5.3 for details); every subsequent contour represents an increase in density by $3 \times \Delta n_{\text{PMS}}$ 55

3.10	Top: Normalised distance distribution for all possible grid pairs for the 208 PMS-only and UMS+PMS classified elements (green line), and for a same-size sample of randomly distributed unclassified elements (black line). Bottom: Same as the top panel, but separating the two classifications.	57
3.11	Three-colour composite image (top left) of the analysed area with H α emission in blue, K_s ($2.15\ \mu\text{m}$) in green, and <i>Spitzer</i> IRAC $8\ \mu\text{m}$ in red. Regions and contours are the same as in Fig. 3.9. Other panels show enlarged views of selected star-forming complexes: N 44 (top right), N 148 (bottom left), and N 51 (bottom right).	60
3.12	Left: Three-colour composite image with VMC Y (blue) and K_s bands (green), and <i>Spitzer</i> IRAC $8.0\ \mu\text{m}$ (see also Fig. 3.9). Green and white crosses mark the locations of elements classified as UMS and “old”, respectively. The UMS+PMS and PMS-only classified elements are included as blue circles to facilitate comparison. Right: Same as the left panel, but using an inverted grey-scale image of the H α emission.	62
3.13	Normalised distance distribution for all possible grid element pairs classified as UMS+PMS (blue) and UMS-only (green) (see also Fig 3.10).	63
3.14	Cumulative number distribution for the 31 PMS structures (0.2 dex bins). The vertical dashed line indicates the sensitivity limit, while the dash-dotted line represents a power law with a slope of -0.86 . The error bars represent the Poissonian uncertainties.	66
3.15	Left panel: Three-colour composite image with <i>Spitzer</i> MIPS $70\ \mu\text{m}$ in blue, <i>Herschel</i> PACS $160\ \mu\text{m}$ in green, and <i>Herschel</i> SPIRE $350\ \mu\text{m}$ in red; the density contours are the same as those in Fig. 3.9. Middle panels: Dust emission distribution for image pixels in areas covered by the UMS+PMS and PMS-only classified elements, and by the same number of randomly selected unclassified elements. A Gaussian fit is plotted and the mean of the fit is indicated. Right panels: Mean dust emission vs. young stars number density for the PMS and UMS+PMS classified elements. The error bars show the typical standard deviations within the dust emission bins.	67
3.16	Ratios of the mean dust emission observed for classified elements and the field average. The widths of the bars mimic the filter bandwidths.	69
4.1	Spatial distribution of all sources from detector 4 and pawprint Epoch 4-J6 with counterpart (left panel), and without counterpart (right panel) in the deep catalogue.	74
4.2	Fluxbased mean magnitudes versus mean photometric errors for the J -band (left panels) and the K_s -band (right panels) for Pawprint 1 to 6 (top to bottom row) over all epochs. The vertical lines in the bottom panels indicate the bright magnitude cutoff (Sec. 4.2.1).	76

4.3	Comparison between the mean photometric errors and the observed standard deviation of the K_s -magnitudes. Every plotted source was detected at least 10 times to reduce the number of outliers caused by small number statistics. The green line shows the 1:1 relation.	78
4.4	Same as Fig. 4.3, but for the J -band.	78
4.5	χ^2 -distributions for K_s -band photometric data for Pawprint 1 to 6 (top to bottom row): left panels for the faint sample ($K_s \geq 15.5$ mag), right panels for the bright sample. The dashed lines indicate the 3σ thresholds.	80
4.6	As Fig. 4.5, but for J -band photometry.	81
4.7	Left panel: Spatial distribution of the 3817 variable star candidates (black points). The labelled blue ellipses show star forming complexes (see Fig. 3.9). Right panel: Distribution of the 3062 unflagged high reliability variables in a $Y - K_s$ CMD. In the background is a Hess diagram of the total stellar population from the deep catalogue. The labelled boxes identify populations discussed in detail in the main text.	83
4.8	Left panel: Same as Fig. 4.7 (right panel) but for flagged variables with low reliability. Right panel: K_s distribution of all variables (grey) and of the flagged variables (red).	86
4.9	Left panel: J vs. ΔJ scatter-plot for the 3062 unflagged high reliability variables. Right panel: Same as on the left, but for the K_s -band.	86
4.10	Left panel: Spatial distribution of the 3240 OGLE variables with counterparts in the deep catalogue. The full extent of Tile LMC_7.5 is shown in the background. Right panel: Distribution of the 2289 OGLE variables which are located in areas covered by at least two pawprints, and which fulfil our requirement for the χ^2 -analysis in at least one filter. The datapoints are colour-coded based on their type.	88
4.11	Left panel: Distribution of the magnitudes for the 2289 OGLE variables, colour-coded based on the variability type. The K_s values are taken from the deep catalogue. Right panel: Distribution of amplitudes in the I -band ($0.8 \mu\text{m}$) as given in the OGLE-III catalogue.	88
4.12	Left panel: Distribution of the I -band ($0.8 \mu\text{m}$) amplitude for the sample of LPVs (red), and for the LPVs identified as variable by our analysis (black). Right panel: As on the left but for the J -band amplitude.	89
4.13	Top panel: J vs. ΔJ scatter-plot for the Cepheids and RR Lyrae stars combined: identified as variable (blue), not identified as variable (red) in the J -band. Bottom panel: Same as on top, but for the K_s -band.	91
4.14	Various properties of the 87 OGLE stars found to be variable in the K_s -band. Top left: Distribution of the periods according to the OGLE-III catalogue. Top right: Distribution of the amplitudes in K_s . Bottom: Period vs. K_s amplitude (left) and Period vs. K_s magnitude (right).	92

- 4.15 **Top left:** Periodogram example for a source with a successfully recovered OGLE period, using the 500 period list. The vertical green line shows the OGLE period (~ 3.7 days). Three horizontal lines indicate the FAP levels of 10 % (dotted), 5 % (dashed), and 1 % (solid). **Bottom left:** Corresponding folded lightcurve for the calculated period, with the sinusoidal model overplotted. **Right panels:** As for the left panels, but for a star where the OGLE period of ~ 0.9 days was not successfully recovered. Note the low amplitude of the variations. 94
- 4.16 **Top left panel:** Period-steps vs. OGLE-period. Stars below the horizontal line (period-steps = 25) are considered successful period detections. The solid circles are colour-coded based on the K_s amplitude. **Top right panel:** Distribution of the FAPs for the OGLE sample, and for the stars with recovered periods. **Bottom panels:** Same as Fig. 4.14 (bottom panels), but with the recovered periods highlighted. 95
- 4.17 **Left panel:** Location of the deep catalogue YSO counterparts in the $Y - K_s$ CMD shown as solid circles. In the background is the total stellar population displayed for comparison. **Right panel:** Distribution of the spatial separation between matched pairs for all YSO counterparts (grey), and for the subsample where the counterparts are comparatively blue ($Y - K_s < 1.2$ mag). 99
- 4.18 **Left panel:** As Fig. 4.17 (left), but only for counterparts with a separation $< 0.75''$. **Right panel:** As on the left, but for counterparts with a separation $> 0.75''$ 100
- 4.19 $K_s - [3.6]$ vs. $Y - K_s$ CCD showing the YSOs from Spezzi et al. (2015) (blue) and massive YSOs (black). The background is the overall stellar population. The $3.6 \mu\text{m}$ photometry is taken from the SAGE catalogue (Meixner et al. 2006), all other filters are from the VMC deep catalogue. Solid lines show the colour cuts, and the arrow represents the reddening vector for $A_V = 10$ mag (Nishiyama et al. 2009). 102
- 4.20 CMD with the total stellar population and showing the YSO sources which fulfilled the colour criteria (see text). The type of data-point is coded based on the study which identified the YSO (C12: Carlson et al. 2012; GC09: Gruendl & Chu 2009; S09: Seale et al. 2009). 103
- 4.21 **Left panel:** VISTA RGB composite with Y ($1.02 \mu\text{m}$) in blue, J ($1.25 \mu\text{m}$) in green, and K_s ($2.15 \mu\text{m}$) in blue showing a *Spitzer*-identified YSO that is likely a background galaxy. **Right panel:** As on the left, but for source resolved into a group of stars. The radius of the circle corresponds to 1 pc at LMC distance. 103
- 4.22 As Fig. 4.20, but for background galaxies and star groups. 104

4.23	Examples for lightcurves of stars identified as eruptives (green circles). The black circles show the lightcurve of a nearby non-variable star (separation $< 3'$) with similar K_s -band magnitude for comparison. Since the photometric errors are very similar we have omitted plotting the error-bars for the companion star. In all lightcurves we use epoch magnitudes obtained from the individual pawprints.	106
4.24	As Fig.4.23 but for stars classified as faders. More details in the main text.	108
4.25	As Fig.4.23 but for stars classified as dippers. The lightcurve in the bottom right panel is from the same object as in the top right panel, just for the J -band.	109
4.26	K_s lightcurves of two YSOs classified as STVs (left panels). The right panels show a zoom into the high cadence observations at the end of the observation window.	110
4.27	Lightcurves of the variable YSOs that are unclassified. The right panels show the K_s lightcurve (top) and J lightcurve (bottom) of the same star.	112
4.28	Zoomed in K_s lightcurves of two YSOs classified as STVs, with the LombScargle model of the calculated period overplotted (left panels). The right panels show the corresponding folded lightcurves.	113
4.29	Left panels: K_s lightcurves of possible LPV-YSOs with their models overplotted. Right panels: Corresponding folded lightcurves.	114
4.30	Left panel: CMD with the YSO sample (circles), and the variable YSOs (squares). Right panel: As on the left, but as a CCD.	115
4.31	Left panel: Distribution of the K_s -amplitudes (ΔK_s) for the variable YSOs. Right panel: K_s vs. ΔK_s plot for the variable YSOs (solid circles). Objects classified as eruptives are highlighted in red. The histogram shows the median- ΔK_s for all detected variables in magnitude bins of 0.5 mag width.	116
4.32	Spatial distribution of the 40 high-amplitude variables ($\Delta K_s > 1$ mag; crosses). The labelled blue ellipses show star forming complexes, the black contours indicate areas with significant PMS populations (see Fig. 3.9). There is a tendency for the high-amplitude variables to be associated with known star forming regions.	118
4.33	Amplitudes for the J and K_s -band, using the magnitude averages for the time-periods as specified in the axis-labels. The circles are colour-coded based on the lightcurve classification of the corresponding YSO.	119

List of Tables

1.1	Sample of observed regions in the LMC with detected PMS candidates.	21
2.1	Filters available with VISTA.	26
3.1	Most likely classifications for mass and age ranges based on synthetic cluster tests.	52
3.2	Number of classified clusters from the sample of 31 clusters from the literature as a function of grid element radius.	53
3.3	Number of PMS candidates in the whole LMC 7.5 tile and individual prominent regions. The errors are calculated assuming grid elements are statistically independent.	64
4.1	χ^2 -thresholds for the different pawprints, filters, and magnitude ranges (Bright sample: $J < 15.3$ mag and $K_s < 15.5$ mag; Faint sample: $J \geq 15.3$ mag and $K_s \geq 15.5$ mag).	82
4.2	Number of stars (N_{tot}), number of variable star candidates (N_{var}), and the corresponding fraction for the CMD-regions labeled in Fig. 4.7 (right panel). Note, that N_{tot} is the number of stars that fulfill the minimum detections requirement ($\text{Detections}_{K_s} \geq 10$, $\text{Detections}_J \geq 6$).	84
4.3	Number of variables, mean amplitudes, the standard deviations, and the median amplitudes for all classes. The sum is 41 instead of 39 because one star was classified as eruptive and dipper, and another as eruptive and LPV-YSO.	117
4.4	Numbers of YSO variables of a given classification in Contreras Peña et al. (2017b) and Teixeira et al. (2018), abbreviated as CP17 and T18, respectively.	121
A.1	Pawprints of K_s observations and associated photometric data.	133
A.1	Pawprints of K_s observations continued.	134
A.1	Pawprints of K_s observations continued.	135
A.1	Pawprints of K_s observations continued.	136
A.2	Pawprints of J observations and associated photometric data.	137
A.2	Pawprints of J observations continued.	138
A.2	Pawprints of J observations continued.	139

1 Introduction

The large majority of our knowledge about star formation is derived from Galactic star-forming regions with near-solar metallicity. Extensive and resolved studies of these regions have provided an understanding of the physical processes involved (for a comprehensive overview see Shu, Adams & Lizano 1987). However, these studies all probe environments that are typical for our Galaxy, hence limiting our view to a small range of environmental conditions.

As the nearest gas-rich galaxy, the Large Magellanic Cloud (LMC) represents an excellent target for resolved star formation studies in environments different from our own Galaxy. Furthermore, its proximity offers the opportunity of bridging the gap between processes on large galactic-wide scales and on the small scales of individual young stellar objects (YSOs). This project samples and characterises young stellar populations in the LMC across an area of $\sim 1.2 \text{ kpc}^2$ (Chap. 3), focusing on scales of clusters, associations, and complexes. On the level of individual stars, this thesis also examines the photometric variability of massive YSOs (Chap. 4).

1.1 Star formation

1.1.1 Conditions for the onset of star formation

It has long been established that molecular clouds are the sites of star formation (Zuckerman & Palmer 1974). The largest are known as Giant Molecular Clouds (GMCs) and can span over several tens of parsecs (Ward-Thompson & Whitworth 2015). GMCs are highly inhomogeneous objects composed of clumps ($M \sim 50 - 500 M_{\odot}$, $R \sim 0.3 - 3 \text{ pc}$, $n_{\text{H}_2} \sim 10^3 - 10^4 \text{ cm}^{-3}$; Bergin & Tafalla 2007), which in itself can include dense subregions that are known as cloud cores ($M \sim 0.5 - 100 M_{\odot}$, $R \sim 0.03 - 0.2 \text{ pc}$, $n_{\text{H}_2} \sim 10^4 - 10^5 \text{ cm}^{-3}$; Bergin & Tafalla 2007). To form stars, gravity must overcome the support mechanisms of a cloud (Shu, Adams & Lizano 1987). We follow Ward-

Thompson & Whitworth (2015) and start deriving the necessary condition by treating the cloud as an ensemble of particles with mass m_i , position \mathbf{r}_i , and velocity \mathbf{v}_i . The moment of inertia \mathcal{I} of the cloud is given by

$$\mathcal{I} = \sum_i m_i \mathbf{r}_i \cdot \mathbf{r}_i. \quad (1.1)$$

The time derivative $\dot{\mathcal{I}}$ is then

$$\dot{\mathcal{I}} = 2 \sum_i m_i \mathbf{v}_i \cdot \mathbf{r}_i. \quad (1.2)$$

Taking the second time derivative gives

$$\begin{aligned} \ddot{\mathcal{I}} &= 2 \sum_i m_i \dot{\mathbf{v}}_i \cdot \mathbf{r}_i + 2 \sum_i m_i \mathbf{v}_i \cdot \mathbf{v}_i \\ &= 2 \sum_i \mathbf{F}_i \cdot \mathbf{r}_i + 4\mathcal{K}, \end{aligned} \quad (1.3)$$

where $\mathbf{F}_i = m_i \dot{\mathbf{v}}_i$ is the force acting on the i -th particle, and $\mathcal{K} = 1/2 \sum_i m_i v_i^2$ is the total kinetic energy due to random thermal motion and bulk motion like rotation and turbulence. Assuming an isolated cloud, \mathbf{F}_i is the sum of all forces acting on particle i due to all other cloud particles. This leads to

$$\begin{aligned} \ddot{\mathcal{I}} &= 2 \sum_i \sum_{j \neq i} \mathbf{F}_{ij} \cdot \mathbf{r}_i + 4\mathcal{K} \\ &= \sum_i \sum_{j \neq i} (\mathbf{F}_{ij} \cdot \mathbf{r}_i + \mathbf{F}_{ji} \cdot \mathbf{r}_j) + 4\mathcal{K} \\ &= \sum_i \sum_{j \neq i} \mathbf{F}_{ij} \cdot (\mathbf{r}_i - \mathbf{r}_j) + 4\mathcal{K}. \end{aligned} \quad (1.4)$$

If \mathbf{F}_{ij} is the force due to gravity between two particles, then $\mathbf{F}_{ij} \cdot (\mathbf{r}_i - \mathbf{r}_j)$ is the gravitational potential energy between them. Hence, the first term on the right-hand side of Eq. 1.4 equals $2\Omega_G$, where Ω_G is the self-gravitational potential energy of the cloud (the factor 2 arises because the summation counts every particle-pair twice).

Finally, this gives

$$\frac{1}{2} \ddot{\mathcal{I}} = \Omega_G + 2\mathcal{K}. \quad (1.5)$$

This relation describing the balance of energies is known as the Virial theorem. For a cloud in equilibrium \mathcal{I} does not change, consequently $\ddot{\mathcal{I}}$ is also zero. Thus the equilibrium condition is

$$0 = \Omega_G + 2\mathcal{K}. \quad (1.6)$$

For the simplest case any bulk motions are ignored and only gravity and thermal pressure are considered. Equation 1.6 becomes

$$0 = \Omega_G + 2U, \quad (1.7)$$

where U is the thermal energy described as

$$U = \frac{3}{2}NkT = \frac{3M}{2\mu m_H}kT, \quad (1.8)$$

with μ and m_H being the mean molecular mass and the hydrogen atomic mass, respectively. The gravitational potential energy of a spherical cloud depends on the density profile, but can be approximated by

$$\Omega_G \approx \frac{GM^2}{R}. \quad (1.9)$$

Substituting Eq. 1.8 and Eq. 1.9 into Eq. 1.7 and expressing the radius R in terms of density and mass leads to

$$M_J \approx \left(3\frac{kT}{G\mu m_H}\right)^{3/2} \left(\frac{3}{4\pi\rho}\right)^{1/2}. \quad (1.10)$$

If the cloud mass is larger than the critical M_J , it undergoes gravitational collapse. M_J is known as the Jeans mass and is derived from the Jeans instability criterion (Jeans 1902). Applying typical temperatures and densities of GMCs (15 K, $n = 10^2 \text{ cm}^{-3}$, e.g. Stahler & Palla 2005) results in $M_J \approx 100 M_\odot$, which is several orders of magnitudes less massive than the GMCs themselves. Considering thermal pressure alone, GMCs would be in a state of collapse. However, systematically inward directed velocities are not observed (Stahler & Palla 2005) and the star formation rate would significantly exceed the observed value in this scenario (Zuckerman & Palmer 1974). Solomon et al.

(1987) found that the velocity dispersion σ in molecular clouds follows a relation with size and mass, such that

$$\frac{GM}{R} \propto \sigma^2. \quad (1.11)$$

Moreover, since the kinetic energy \mathcal{K} matched $|\Omega_G|$ over a wide range of cloud sizes (Myers & Goodman 1988), turbulent motions seem to be able to balance out the gravitational pull. Turbulence is however expected to decay quickly without an additional source of energy (Goldreich & Kwan 1974). Therefore, another support mechanism is needed to prevent a quick onset of gravitational collapse.

Observational evidence for magnetic fields in the Interstellar medium (ISM) has been found several decades ago using polarisation observations (Axon & Ellis 1976). The energy density of a magnetic field exerts a pressure of

$$P_{\mathcal{M}} = \frac{B^2}{8\pi}, \quad (1.12)$$

where B is the magnetic field strength. The total magnetic energy stored in a volume V is therefore

$$\mathcal{M} = \frac{1}{8\pi} \int_V B^2 dV. \quad (1.13)$$

To account for this additional energy term, the Virial theorem is accordingly modified to include the effect of magnetic fields. The equilibrium condition is then

$$0 = \Omega_G + \mathcal{M} + 2\mathcal{K}. \quad (1.14)$$

Charged particles are bound to the magnetic field lines, causing the field and the gas to move together like a magnetized fluid. This flux-freezing effectively leads to a conservation of the magnetic field flux permeating the cloud, which provides long-term support against collapse.

This raises the question of how a magnetically subcritical cloud could loose support against gravity in order to condense into cloud cores and subsequently into stars. A possible mechanism to overcome support is ambipolar diffusion. A magnetic field only directly affects charged particles, which gyrate around the field lines. Neutral particles are free to move across the lines, however the charged and neutral gas components are coupled through collisions. The strength of this coupling depends on the

ionisation fraction: the smaller the fraction the larger the possible drift between the two components. The magnetic flux through a cloud can thus be slowly decreased, weakening its support. The timescale for ambipolar diffusion is

$$\tau_{\text{AD}} = 7.3 \times 10^{13} \frac{n_i}{n_{\text{H}}} \text{yr}, \quad (1.15)$$

where n_i/n_{H} is the ionisation fraction. Clearly, ambipolar diffusion is a very slow process. Given the lifetimes of GMCs (4–25 Myr, e.g. Dobbs & Pringle 2013), a very small ionisation fraction is necessary for ambipolar diffusion to have an impact. Such small fractions are believed to exist in molecular clouds (e.g. Schulz 2012). For a comprehensive discussion on molecular clouds and the global conditions for star formation we refer to Dobbs et al. (2014).

1.1.2 Early stellar evolution

In the early stages of collapse the cloud is approximately isothermal as long as the energy released by the gravitational contraction can be radiated away efficiently enough. In this case the thermal pressure only increases proportional to the density ρ , and can therefore never match the gravitational pressure which grows proportional to $\rho^{4/3}$. As a result the collapse proceeds on a free fall timescale (Hayashi 1966):

$$t_{\text{ff}} \sim \sqrt{\frac{3\pi}{32G\rho}}. \quad (1.16)$$

The Jeans mass M_{J} , which represents the smallest mass that can collapse under given thermodynamical conditions, decreases with density ($\propto \rho^{-1/2}$; Eq.1.10). During the global contraction, stable parts of the cloud can therefore become gravitationally unstable on their own. As a consequence they start to collapse independently. This local collapse causes the original cloud to fragment.

The isothermal free-fall phase continues as long as the density is below $\sim 10^{-13} \text{g cm}^{-3}$ (e.g. Schulz 2012). Once this value is exceeded in the central regions of the cloud, the material becomes opaque to its own radiation. The released gravitational energy can no longer escape efficiently and the gas heats up. As a consequence,

the thermal pressure increases rapidly, slowing down the collapse. A first hydrostatic core is created, surrounded by a thick circumstellar envelope (Larson 1973). Typical sizes for the first core are in the range of 1–10 AU, with masses roughly between 10^{-3} – $10^{-2} M_{\odot}$ (Bhandare et al. 2018). Hence, it contains only a tiny fraction of the initial cloud core mass. The hydrostatic core contracts adiabatically while it steadily heats up. Once central temperatures reach ~ 2000 K the H_2 molecules start to dissociate. Since this is an endothermic process it removes the energy that would otherwise increase the gas temperature. A second collapse takes place as the thermal pressure cannot counter the increasing gravitational load. Once all H_2 molecules have been dissociated in the central regions, a second hydrostatic core forms. This object is usually referred to as a protostar, which is still deeply embedded in its envelope.

The protostar continues to accrete material from the envelope and enters the main accretion phase during which it builds up most of its final mass. The accreted material falls onto the boundary between protostar and envelope with a free-fall velocity:

$$v_{ff} = \sqrt{\frac{2GM_*}{R_*}}, \quad (1.17)$$

where M_* and R_* are the mass and radius of the protostar, respectively. The excess kinetic energy is dissipated at the shock front. Assuming that all kinetic energy is transformed into photons, the accretion luminosity can be expressed as

$$L_{\text{acc}} = \frac{GM_*\dot{M}}{R_*} \quad (1.18)$$

where \dot{M} is the mass accretion rate.

As a cloud core contracts and a protostar is formed in the center, even modest initial rotational velocities will play a key role in the deep interior. Due to angular momentum conservation, the angular rotational speed of an infalling particle is $\Omega_r = \Omega_0(r_0/r)^2$, where Ω_0 and r_0 are the initial values for angular rotation and distance from the rotational axis. Consequently, the centrifugal force increases with r^{-3} , faster than the r^{-2} rise due to gravity. The centrifugal support will therefore prevent a direct infall onto the protostar perpendicular to the rotational axis. However, it has no

effect parallel to the rotational axis. This leads to the formation of disc-like structures, in which friction aids angular momentum transfer outwards making further accretion onto the protostar possible (Hartmann 1998). The full picture of the young protostellar system consists of a protostar in the center with an infalling envelope that feeds an accreting circumstellar disc.

The embedded protostar increases its mass quickly via disc accretion; the accretion rate is assumed to be highly variable with values between 10^{-4} and $10^{-7} M_{\odot} \text{ yr}^{-1}$ (e.g. Schulz 2012). Several mechanisms are thought to be the cause of accretion bursts: fragmentation due to gravitational instabilities (Vorobyov & Basu 2010), a change in viscosity due to thermal instabilities (see Audard et al. 2014 and references therein), or external triggers like a close encounter in dense stellar clusters (Pfalzner 2008). The envelope mass is thought to drop below $\sim 5\%$ of the initial cloud core mass within 0.5 Myr (Vorobyov & Basu 2010), at which point the burst activity diminishes because the mass transfer from the envelope to the disc drops to low levels: the accretion rate onto the star decreases to $\lesssim 10^{-7} M_{\odot} \text{ yr}^{-1}$. Once the envelope has been accreted and only a circumstellar disc is left, the star is usually referred to as a pre-main sequence (PMS) star *if* hydrogen burning in its core has not yet started. A PMS star still contracts and radiates away gravitational potential energy. The evolution is then governed by the Kelvin-Helmholtz timescale:

$$t_{KH} = \frac{GM_*^2}{R_*L_*}. \quad (1.19)$$

With the onset of hydrogen burning the star is stabilised by the energy released in the nuclear reactions and settles onto the main-sequence. The minimum mass required for hydrogen burning is $\sim 0.075 M_{\odot}$ (Cañas et al. 2018).

1.1.2.1 Observational identification of young stars

During the protostellar stage a direct view on the emerging protostar at visual and near-IR (NIR) wavelengths is prevented by the thick envelope. The radiation released due to contraction and accretion (Eq. 1.18) is absorbed by the surrounding dust and re-

radiated at longer wavelengths. Even when the envelope has disappeared, leaving only the circumstellar disc, an infrared (IR) excess due to dust emission is observed (e.g. Lynden-Bell & Pringle 1974). Consequently, YSOs¹ are often identified by their redder colours compared to main-sequence stars of similar luminosity, occupying different regions in colour–colour and colour–magnitude diagrams (see Sec. 3.2 and 4.5.3.1). Since IR wavelengths are less affected by dust extinction, YSOs are in general best studied in the IR regime.

Lada (1987) defined the spectral index,

$$\alpha = \frac{d \log (\lambda F_{\lambda})}{d \log \lambda}, \quad (1.20)$$

measured for fluxes F_{λ} between $2 \mu\text{m}$ and $20 \mu\text{m}$ to categorise YSOs into three classes. The classification scheme was as follows:

- Class I: $\alpha \geq 0.3$
- Class II: $-1.6 \leq \alpha < -0.3$
- Class III: $\alpha < -1.6$

Class I corresponds to the protostellar stage with an infalling envelope feeding an accretion disc. Class II corresponds to a later stage in which the envelope has dissipated, leaving a circumstellar disc from which the star continues to accrete material. Finally, a Class III star has a remnant or no disc left, but it has not yet reached the main sequence. Class 0 was introduced subsequently to describe objects too deeply embedded to be detected in the near-IR (Andre, Ward-Thompson & Barsony 1993). The progress from Class 0 to Class III is therefore understood as an evolutionary sequence where the star gradually dissipates the surrounding material. PMS stars are either Class II (prominent circumstellar disc) or Class III (circumstellar material essentially dissipated). Figure 1.1 shows the typical spectral energy distributions (SEDs) associated with the four classes.

¹The umbrella term “YSO” covers both the protostellar and the PMS phase.

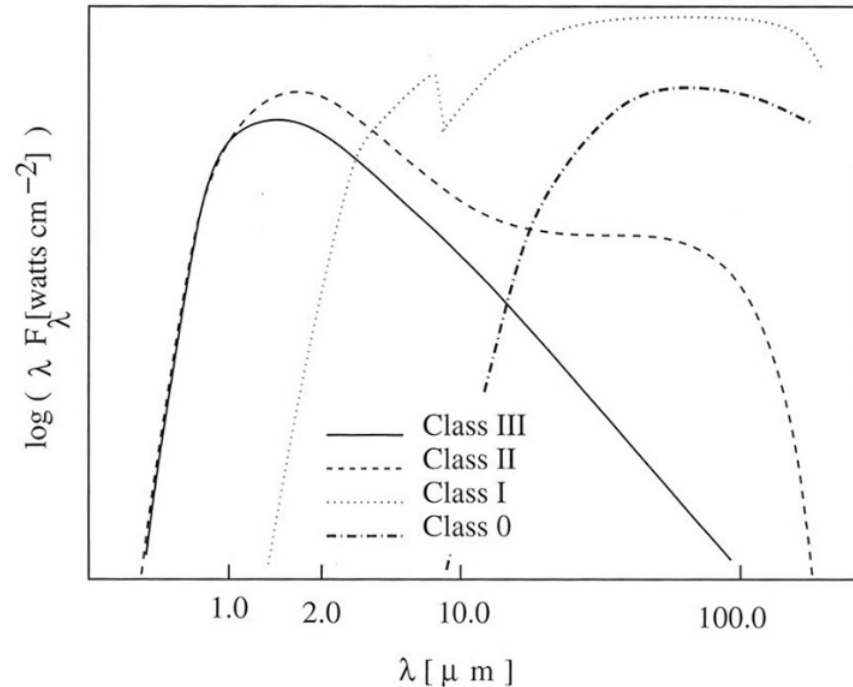


Figure 1.1: Typical SEDs for the different YSO classes (Schulz 2012)

$H\alpha$ excess emission, powered by ongoing disc accretion (e.g. Edwards et al. 1994), is another well established youth indicator. In fact, the original identification of young low-mass stars was based on objects showing $H\alpha$ emission lines (Joy 1945). Due to their similarity to T Tau they were named T Tauri stars. They are either Class II (classical T Tauri star) or Class III (weak line T Tauri star) objects with masses up to $\sim 2 M_{\odot}$. Their intermediate mass ($\sim 2 - 8 M_{\odot}$) counterparts, the Herbig Ae/Be stars, were also identified by their bright emission lines (Herbig 1960). Figure 1.2 shows the evolution of a typical T Tauri star, including typical timescales.

1.1.2.2 Massive YSOs

The evolution described in Sec. 1.1.2 and the classes in Sec. 1.1.2.1 are not applicable to massive YSOs, i.e. their formation is not an exact scale-up of the intermediate/low

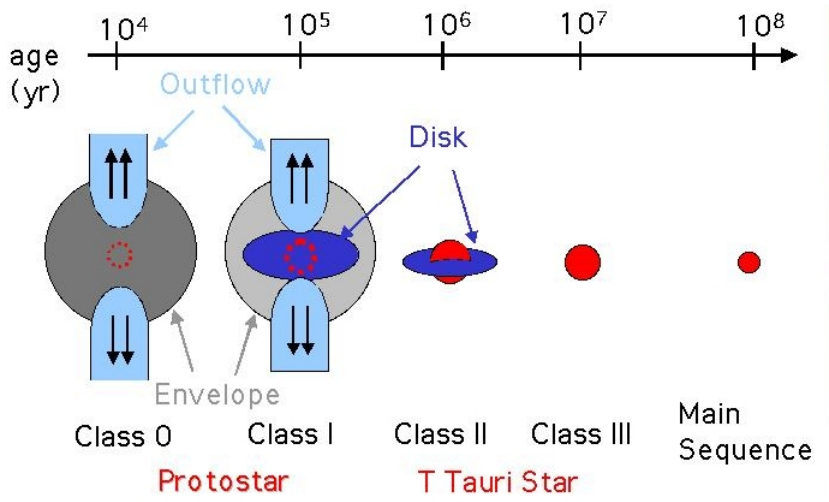


Figure 1.2: Schematic representation of the evolution of a low mass star. From <http://www-cr.scpphys.kyoto-u.ac.jp/research/xray/press200011/figures/>

mass young stellar evolution. Massive stars are usually defined as stars with masses $\gtrsim 8 M_{\odot}$. Using $R_* = 3.9 R_{\odot}$ and $L_* = 2600 L_{\odot}$ in Eq. 1.19, which are typical values for an $8 M_{\odot}$ star (e.g. Pecaut & Mamajek 2013), gives $t_{KH} \approx 3 \times 10^5$ yr. Since this is approximately the time needed for the envelope to dissipate (e.g. Schulz 2012; Vorobyov & Basu 2010), stars with $\gtrsim 8 M_{\odot}$ have already started hydrogen burning before they dissipate their envelopes and become optically visible, essentially bypassing the PMS phase. Hence, massive YSOs do not have Class II or Class III analogue stages.

In order to form a massive star by direct gravitational collapse it is necessary to suppress the further fragmentation of a cloud core (Sec. 1.1.2), otherwise a cluster of comparatively low mass stars will be formed. Simulations by Myers et al. (2013) explored the effect of magnetic fields and radiative feedback on the fragmentation. They found that both mechanisms combined are very effective at preventing fragmentation. Magnetic fields tend to stabilise regions of the cloud core that would be Jeans unstable, but which are magnetically subcritical. Also they remove angular momentum via magnetic braking, enhancing the mass flux towards the center. The increased accretion rate leads to a higher accretion luminosity, heating the gas and thereby increasing the

Jeans mass. Another mechanism is the turbulent core model (McKee & Tan 2003), where the support against further fragmentation comes from supersonic turbulence. Cluster formation simulations using turbulent cores (Krumholz, Klein & McKee 2012) generated systems that indeed reproduced the observed initial mass function (IMF) up into the massive stars regime.

Another scenario for massive star formation is the competitive accretion model (Bonnell & Bate 2006). In this scenario YSOs located near the centre of young stellar systems are able to accrete at higher rates, since they benefit from the gravitational attraction of all YSOs as gas is funnelled into the inner regions. Objects not located near the centre do not accrete significantly such that their masses are set by the fragmentation process, while these centrally located develop into high mass stars. However, stars with masses $\sim 100 M_\odot$ have been found in environments of comparatively low density (e.g. Wright et al. 2014), indicating that massive stars are able to form also by other mechanisms (see also Krumholz, McKee & Klein 2005).

Another challenge compared to low mass stars is set by the strongly super-linear relationship between mass and luminosity ($L \propto M^{3.5}$, Salaris & Cassisi 2006). While this is a relationship for main-sequence stars, the short contraction time of massive YSOs turns them into main-sequence stars while accreting. Hence, their radiation pressure is a significant barrier to further accretion, effectively capping the maximum mass. For accretion to occur the gravitational force has to be stronger than the radiative force, i.e.

$$\frac{GM_*}{r^2} > \frac{\kappa L_*}{4\pi r^2 c}, \quad (1.21)$$

or correspondingly

$$\frac{L_*}{M_*} < \frac{4\pi Gc}{\kappa}, \quad (1.22)$$

where κ is the dust opacity. Transformed into more convenient units, equality of both forces occurs at

$$\left(\frac{L_*}{M_*}\right) = 1300 \left(\frac{L_\odot}{M_\odot}\right) \kappa_1^{-1}, \quad (1.23)$$

with $\kappa_1 = \kappa / (10 \text{ cm}^2 \text{ g}^{-1})$ (Krumholz 2015). Stars with $M_* \gtrsim 20M_\odot$ exhibit $L_*/M_* \gtrsim 1300(L_\odot/M_\odot)$, hence stars should not be able to accrete beyond this point. However,

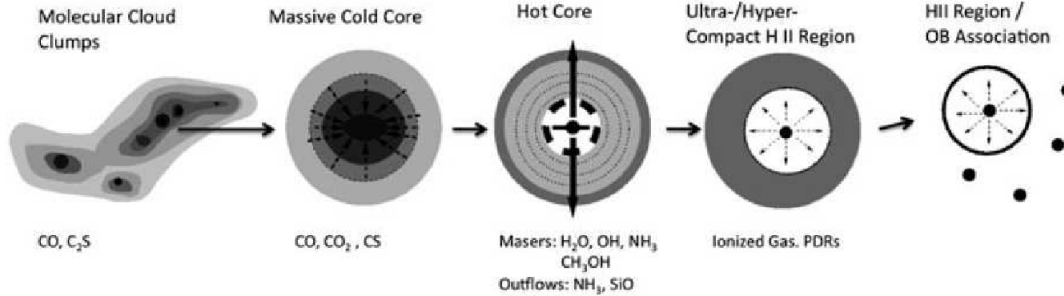


Figure 1.3: Schematic representation of the early evolution of massive stars (Schulz 2012)

this estimate is only valid for spherically symmetric accretion, which is unrealistic. Angular momentum conservation forces the material into an accretion disc (see Sec. 1.1.2) which concentrates the ram pressure into the equatorial plane, enabling accretion up to higher masses. Kuiper et al. (2010) showed that disc accretion can form stars with masses in excess of $> 100 M_{\odot}$, essentially covering the entire observed high-mass range.

From an observational perspective the earliest phase of high-mass star formation are IR dark clouds (IRDCs) with H₂ column densities of $10^{23} - 10^{24} \text{ cm}^{-2}$ (e.g. Zinnecker & Yorke 2007), which contain massive and compact cold cores. IRDCs are more dense and massive than the clouds that only produce low-mass stars. While optically thick and with negligible emissions in the NIR, they usually show prominent emissions in the sub-mm regime (e.g. Parsons, Thompson & Chrysostomou 2009) due to their low temperatures. The next stage are hot molecular cores (100 – 200 K, Ward-Thompson & Whitworth 2015) consisting of warm gas and dust heated by newly formed massive protostars. The release of ices and volatile grain material creates a rich chemistry with prominent SiO, OH, and water emission (Schulz 2012). Particularly methanol maser emission is exclusively associated with high mass star formation (e.g. Oliveira et al. 2006). Once the evolving star is hot enough it emits copious amounts of energetic photons which create growing pockets of ionised gas. Depending on their size they are known as hypercompact, ultracompact, or compact H II regions (e.g. Yorke 1986; Hoare

& Franco 2007). Finally, when the gas is ionized globally, often by multiple ionising sources, a classical H II region develops. It further expands and disrupts the molecular cloud, revealing the newly formed stellar population. Figure 1.3 shows schematically the evolution sequence for massive stars.

1.2 YSO variability

Variability was early recognized as one of the defining characteristics of stars in the process of formation (Joy 1945; Herbig 1952). In one of the first NIR monitoring programs of young stars (Skrutskie et al. 1996), all 15 observed PMS stars exhibited variability greater than the uncertainties of the photometry. Subsequent large programs showed that 50–60% of all young stars are significantly variable (e.g. Carpenter, Hillenbrand & Skrutskie 2001; Morales-Calderón et al. 2011), making variability an excellent tracer of stellar youth (e.g. Briceño et al. 2005; Lucas et al. 2017). The large range of variability time-scales (days to years), amplitudes (one tenth to over two magnitudes), and light curve shapes (periodic and sinusoidal, periodic non-sinusoidal, irregular) suggests a variety of physical mechanisms leading to variability.

- **Starspots:** This phenomena signposts regions which are either hotter or cooler than the average photospheric temperature. Cool starspots arise similarly to sunspots in magnetively active regions (Bouvier & Bertout 1989), whereas hot starspots are thought to be regions where material accreted along magnetic field lines impacts the star (Hartmann, Hewett & Calvet 1994). The photospheric variability is induced by rotational modulation of the fractional spot coverage towards the observer. Starspots have been known to exist in T Tauri stars and were used to calculate rotational periods (Bouvier et al. 1993). For a fractional cold spot area coverage of $\sim 30\%$ with $T_* - T_{spot} \approx 2000$ K peak-to-peak amplitudes in the near-IR of ~ 0.4 mag are predicted (Carpenter, Hillenbrand & Skrutskie 2001). Hot spots are able to produce larger amplitudes of > 1 mag,

since the temperature difference to the photosphere can be significantly higher (Wolk, Rice & Aspin 2013).

- **Extinction:** Variability due to extinction is caused by inhomogeneities in the material along the line of sight. They can be located in the circumstellar environment or in the ambient cloud. The variable star is then expected to exhibit colour changes according to a reddening law if the grain size distribution is comparable to the interstellar grain size distribution (see Mathis 1990 for a comprehensive overview). The amplitudes of the variations can in principle be arbitrarily high and depend on the increase in dust column density towards the star. An example for this type of variables are UXors (Natta & Whitney 2000), named after the prototype UX Ori. UXor variability is mainly observed in Herbig Ae/Be and T Tauri stars (Eiroa et al. 2002), but massive YSO variability has been identified that is probably linked to temporal changes in extinction (Teixeira et al. 2018).
- **Accretion:** We have discussed in Sec. 1.1.2 that mass accretion rates can be highly unsteady. It is estimated that $\sim 25\%$ of the total accreted mass during the protostellar stage does so during accretion bursts (Offner & McKee 2011), where the mass accretion changes sporadically by several orders of magnitudes. Photometric variability can then result due to changes in the accretion luminosity (Eq. 1.18), or changes in the accretion disc structure that alter the amount of reprocessed stellar radiation (Carpenter, Hillenbrand & Skrutskie 2001). The variability is usually irregular and can produce large amplitudes ($\Delta K_s > 2.5$ mag in extreme cases; Contreras Peña et al. 2017b). Two general classes of outbursting young variables are identified: FUors, named after the prototype FU Orionis (Herbig 1977), and EXors, named after EX Lupi (Herbig 2007). FUors have long duration outbursts (tens of years) with large amplitudes of several , while EXors exhibit much shorter outbursts (weeks to months).

All these mechanisms can interplay and create complicated lightcurves which renders their interpretation difficult. Galactic studies like the Young Stellar Object Variability (YSOVAR) program found clear correlations between *global* variability characteristics and the age of a young stellar population (Rebull et al. 2014). Long variability timescales (weeks or longer) and large amplitudes of $\Delta K_s > 1$ mag are observed amongst stars in earlier evolutionary stages (Class I protostars; Contreras Peña et al. 2014), and are likely associated with highly unsteady accretion from a circumstellar disc. Moreover, YSOs at these stages appear to dominate the high-amplitude variables population at NIR wavelengths (Lucas et al. 2017). YSO lightcurves display great diversity in shape, based on which they were classified in Contreras Peña et al. (2017b), Teixeira et al. (2018), and in this work (see Sec. 4.6.1). More evolved YSOs show on average smaller variability amplitudes (usually $\Delta K_s < 0.5$ mag) and shorter periods ($P \lesssim 15$ d), caused by obscuration events due to structures in the inner circumstellar disc (for Class II objects), or photospheric phenomena like cool and/or hot spots (in both Class II and Class III). Colour variations also seem to be smaller for more evolved Class III stars (Rice et al. 2015), indicating physical mechanisms that have little influence on the colour (like starspots).

1.3 The influence of metallicity

Only a minor fraction of the mass in the universe is made up of metals ($\sim 2\%$ for solar metallicity), however their influence cannot be overstated. The presence of the numerous molecular and atomic species provide many ways in which radiation can interact with matter. This is of particular importance in star forming regions, since many physical processes involve the interaction of the ISM with radiation fields. A different metallicity could therefore have a profound effect on the star formation process.

1.3.1 Heating and cooling balance

In order to develop cloud cores and subsequently stars, a molecular cloud must be able to dissipate the heat produced during the contraction. Hence, cooling agents are needed which are capable to efficiently radiate away the thermal energy content, otherwise cloud collapse is prevented. Molecular hydrogen, the most abundant molecule, has widely spaced energy levels between the different rotational states due to its low mass. Furthermore, dipole transitions are strongly forbidden for homonuclear molecules like H_2 . As a result, the excitation temperature for the lowest rotationally excited state is around 500 K (Gry et al. 2002). Consequently, H_2 is an inefficient cooling agent for $T < 500$ K. Molecular clouds have temperatures well below this value ($\sim 10 - 40$ K, Ward-Thompson & Whitworth 2015), thus other species than H_2 must be involved in the cooling process.

Metallic cooling agents provide many transitions at significantly lower temperatures. Their comparatively large mass leads to tighter spaced energy levels which can provide efficient cooling down to the cold temperatures prevalent in molecular clouds. Figure 1.4 shows the cooling rates of a few basic molecules and atoms for a density of $n = 1 \text{ cm}^{-3}$. Despite being an inefficient coolant for $T \lesssim 500$ K, H_2 is the dominant coolant agent down to roughly 100 K due to its abundance. However, at lower temperatures all efficient agents are metals or metallic molecules. Fine-structure line emission of carbon and oxygen, and rotational transitions of molecules like CO are the most efficient cooling mechanisms. In the early stages of star formation where densities are low, CO is the dominant coolant for molecular clouds. With increasing density other molecules like O_2 and H_2O become more important (Tielens 2010). Recently, Oliveira et al., in prep. have showed that the cooling balance is distinct in Magellanic YSOs compared to Galactic samples. Finally, the gas-to-dust ratio is higher at lower metallicities (e.g. Rémy-Ruyer et al. 2014). This affects the thermal radiation of dust grains, another important cooling process.

Simulations for metallicities of $0.3 Z_\odot$ and densities $n = 10^4 \text{ cm}^{-3}$ (typical for prestellar cores), have shown an increase in temperature by a factor of roughly 1.5

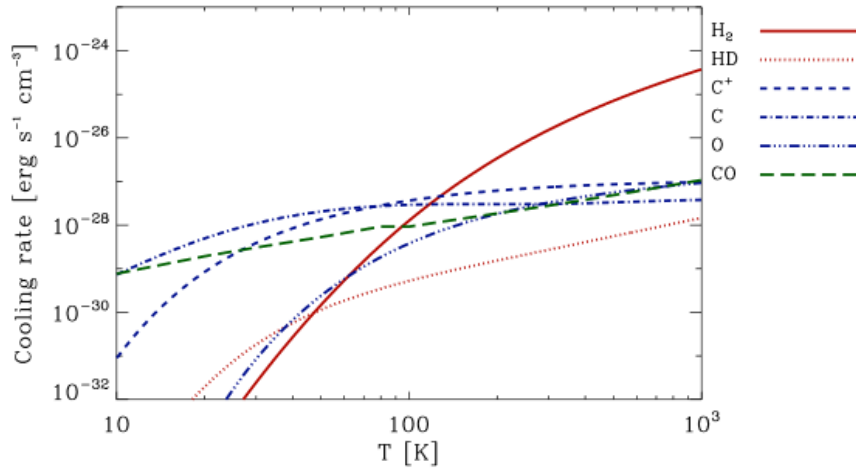


Figure 1.4: Cooling rates for different coolants (Klessen & Glover 2016). For H_2 and its deuterated analogue HD a fully molecular gas is assumed, while the C and O abundances are taken from Sembach et al. (2000). The density is assumed to be $n = 1 \text{ cm}^{-3}$ and the values are weighted by the fractional abundance of the coolants relative to H_2 .

(Glover & Clark 2012). This corresponds to an increase in the Jeans mass of a factor ~ 2 (Eq. 1.10). Since a reduced metallicity seems to affect the cooling efficiency, it is reasonable to expect also some influence on the initial stages of star formation and the fragmentation process. Observational studies are inconclusive as some show indications that metal-poor environments lead to a shallower IMF slope (Marks et al. 2012; Martín-Navarro et al. 2015), while others do not find any significant difference (Yasui et al. 2016).

1.3.2 Circumstellar discs

Observational studies indicate disc lifetimes in low metallicity environments as short as 1 Myr (Yasui et al. 2010; Yasui et al. 2016), while at near solar metallicities the disc half life is close to 3 Myr (Haisch, Lada & Lada 2001). This directly affects the star as it limits the time window in which it is able to accrete material. Ercolano &

Clarke (2010) investigated the metallicity-dependence of X-ray photoevaporation rates of discs. They found that the X-ray wind rates increase with lower metallicities which consequently would reduce disc lifetimes. This is due to the fact that metals increase the X-ray opacity of the disc. Since a low metallicity implies a lower opacity, a larger column can be heated, increasing the efficiency of X-ray photoevaporation.

Another process that affects the disc lifetime is viscous accretion, which transfers angular momentum outwards and allows the material to spiral inwards (Hollenbach, Yorke & Johnstone 2000). For low metallicities the viscosity is predicted to be lower (Durisen et al. 2007), leading to an increase of the viscous time and consequently to an *increase* of the disc-lifetime. Indeed, the measured mass accretion rates for $\gtrsim 10$ Myr old PMS populations in the metal-poor LMC could indicate longer disc lifetimes (Spezzi et al. 2012).

In addition, several studies of star forming regions in both Magellanic Clouds have also reported a consistently higher mass accretion rate compared to similar Galactic samples of PMS stars (De Marchi et al. 2011; De Marchi, Beccari & Panagia 2013a; Spezzi et al. 2012). Higher accretion rates were also found for massive YSOs (Ward et al. 2017). It is assumed that higher metallicity limits the accretion in both rate and duration due to higher radiation pressure (Biazzo et al. 2019). As the mass accretion rates scale with circumstellar disc mass (e.g. Manara et al. 2016), this implies higher disc masses for the Magellanic Cloud PMS stars.

The influence of metallicity on the discs could have implications for young stellar variability. More massive discs are prone to gravitational instabilities (Evans et al. 2015) that can cause strong changes in the inward mass accretion, likely leading to larger variability amplitudes among young LMC stars than in Galactic samples. If the disc lifetimes are indeed shortened as some aforementioned studies indicate, more short-period variables with smaller amplitudes are expected compared to Galactic samples of similar age. For stars whose variability is caused by obscuration events from a dusty disc two mechanisms operate in opposite directions. As the gas-to-dust ratio is larger, the disc opacity gets smaller which would decrease the variability amplitudes. However, with more massive discs the disc inhomogeneities causing the variability might be more

pronounced, counteracting the lower opacity.

1.4 The Large Magellanic Cloud

Dwarf galaxies in our local universe offer the best opportunity to study star formation, young stellar populations, and the ISM at low metallicities. The Magellanic Clouds (MCs) are nearby, interacting, gas-rich galaxies with metallicities lower than typically encountered in the Milky Way (e.g. Stanimirović, Staveley-Smith & Jones 2004; Besla et al. 2012). With moderate distances of 50 ± 2 kpc for the LMC (de Grijs, Wicker & Bono 2014) and 61.9 ± 0.6 kpc for the Small Magellanic Cloud (SMC; de Grijs & Bono 2015), they provide a great opportunity to study resolved star formation down to the scales of individual young stellar objects under different environmental conditions than those found in the Galaxy. The LMC has an apparent size on the sky of approximately $5.4^\circ \times 4.6^\circ$ (Cook et al. 2014) and is seen almost face-on (van der Marel & Cioni 2001). Its depth is 4.0 ± 1.4 kpc and 3.44 ± 1.16 kpc in the bar region and the disc, respectively (Subramanian & Subramanian 2009), leading to relatively small distance modulus variations among its stellar members. The mean metallicity of the LMC is $Z \approx 0.5Z_\odot$ (e.g. Russell & Dopita 1992), which places it close to the mean metallicity of the interstellar medium during the time of peak star formation in the Universe (Pei, Fall & Hauser 1999). A linear decrease of the metallicity away from the center out to ~ 8 kpc is reported (Cioni 2009).

It is relatively easy, compared to the Milky Way, to study star formation in the LMC on a galaxy-wide scale. Observations suffer less from confusion and extinction effects, which often plague Galactic studies as the star forming regions of the Milky Way are concentrated in the disc-plane. The LMC is home to 30 Doradus, the brightest H II region of the Local Group, which comprises multiple generations of young stars and includes hundreds of very massive O-type stars (e.g. Evans et al. 2011). A CO survey of the LMC (Fukui et al. 2001) revealed 168 GMCs with sizes in the range of 28 – 120 pc and a total mass of $\sim 4.2 \times 10^7 M_\odot$. Further evidence of the high star

forming activity in the LMC are 494 young stellar systems (OB-associations and open clusters), identified in an area of $6.5^\circ \times 6.5^\circ$ centred around the LMC bar (Gouliermis et al. 2003).

After the initial burst of star formation in the LMC over 10 Gyr ago, a relatively quiescent period followed that lasted till 5–6 Gyr in the past (Harris & Zaritsky 2009). There are clear indications that the star formation rate (SFR) has two pronounced peaks around 5 Gyr and 2 Gyr ago (Rubele et al. 2012), which may be connected with tidal interactions between the LMC and the SMC (Harris & Zaritsky 2009). The total stellar mass of the LMC is estimated to be $\sim 2.7 \times 10^9 M_\odot$ (van der Marel 2006).

1.4.1 Observational studies of young stars in the LMC

The first studies of young stellar populations within the MCs were published over half a century ago (Westerlund 1961; Bok 1966). Lucke & Hodge (1970) created a catalogue of 122 OB associations in the LMC, based on observations at optical wavelengths down to $m_V \approx 16$ mag, which corresponds at the LMC distance to an $\sim 11 M_\odot$ main-sequence star of age 10 Myr (Bressan et al. 2012). The advent of sensitive CCD detector arrays improved the detection limit so that more detailed studies of the stellar content of associations became possible (e.g. Massey, Parker & Garmany 1989; Massey et al. 1989).

A huge leap in sensitivity and resolution was provided by the *Hubble Space Telescope* (HST). Optical imaging studies of young clusters and OB associations in both galaxies have found evidence of extensive PMS populations well below the solar mass regime (e.g. Gilmozzi et al. 1994; Panagia et al. 2000; Gouliermis, Brandner & Henning 2006; Gouliermis et al. 2006; Gouliermis et al. 2007; Gouliermis et al. 2011). Analysis of the PMS populations in the 30 Doradus region, revealed by the Hubble Tarantula Treasury Project (HTTP; Sabbi et al. 2013), allowed Cignoni et al. (2015) to reconstruct the star formation history of the complex. They identified three major star forming events 20 Myr, 7 Myr and 1–3 Myr ago. Overall, the observed initial mass function (IMF) in the LMC is consistent with that of the Galaxy (e.g. Da Rio, Goulier-

Table 1.1: Sample of observed regions in the LMC with detected PMS candidates.

Cluster/Association	ra	dec	age (Myr)	Reference
LH 9	04h 56m 39s	-66°29'00"	3–10	Vallenari, Chiosi & Sordo (2010)
LH 10	04h 56m 52s	-66°24'25"	2–4	Vallenari, Chiosi & Sordo (2010)
LH 13	04h 57m 44s	-66°27'42"	2–5	Vallenari, Chiosi & Sordo (2010)
NGC 1850 B	05h 08m 46s	-68°45'39"	4.3 ± 0.9	Gilmozzi et al. (1994)
LH 52	05h 25m 38s	-66°17'03"	2–5	Gouliermis, Brandner & Henning (2005)
LH 60	05h 27m 24s	-67°27'00"	3–5	Gouliermis et al. (2011)
LH 63	05h 28m 00s	-67°25'12"	3–5	Gouliermis et al. (2011)
LH 72	05h 32m 12s	-66°27'00"	3–5	Gouliermis et al. (2011)
SN 1987 A cluster	05h 35m 28s	-69°16'11"	10–14	Panagia et al. (2000)
LH 95	05h 37m 04s	-66°22'01"	2.8–4.4	Da Rio, Gouliermis & Gennaro (2010)
NGC 2060	05h 37m 47s	-69°10'22"	4–6	Sabbi et al. (2016)
LH 99	05h 37m 48s	-69°10'00"	~ 10	Sabbi et al. (2013)
Hodge 301	05h 38m 17s	-69°04'00"	20–25	Grebel & Chu (2000)
R 136	05h 38m 42s	-69°06'03"	1–4	Sabbi et al. (2016)

mis & Henning 2009; Liu et al. 2009a; Liu et al. 2009b). Spezzi et al. (2012) and De Marchi, Beccari & Panagia (2013b) used narrow-band photometry with an H α -filter to identify PMS objects actively undergoing mass accretion. Both studies found that PMS stars in the MCs have higher mass accretion rates than stars of similar mass in the Galaxy, which might be an effect of metallicity (see Sec. 1.3.2). These HST studies targeted individual associations and/or star-forming complexes, uncovering the young stellar populations down to masses as low as $\sim 0.3 M_{\odot}$. Table 1.1 provides an overview of some LMC regions with active star formation for which PMS populations have been detected.

In contrast, wide-field photometric surveys give a galaxy-wide overview of the stellar populations. They allow investigating the large-scale distribution of star-forming complexes and their relationship with the underlying gas and dust distribution. Examples for large surveys covering the LMC are the Magellanic Cloud Photometric Survey (Zaritsky et al. 2002; Zaritsky et al. 2004) which performed optical imaging, and the 2 Micron All Sky Survey (2 MASS; Skrutskie et al. 2006) which provided near-IR images. The VISTA survey of the Magellanic Clouds (VMC; Cioni et al. 2011), a near-IR survey which surpasses the depth of 2 MASS by ~ 4 mag, is described in detail in Chap. 2.

With a wavelength coverage from $3.6 - 500 \mu\text{m}$, the *Spitzer* Space Telescope

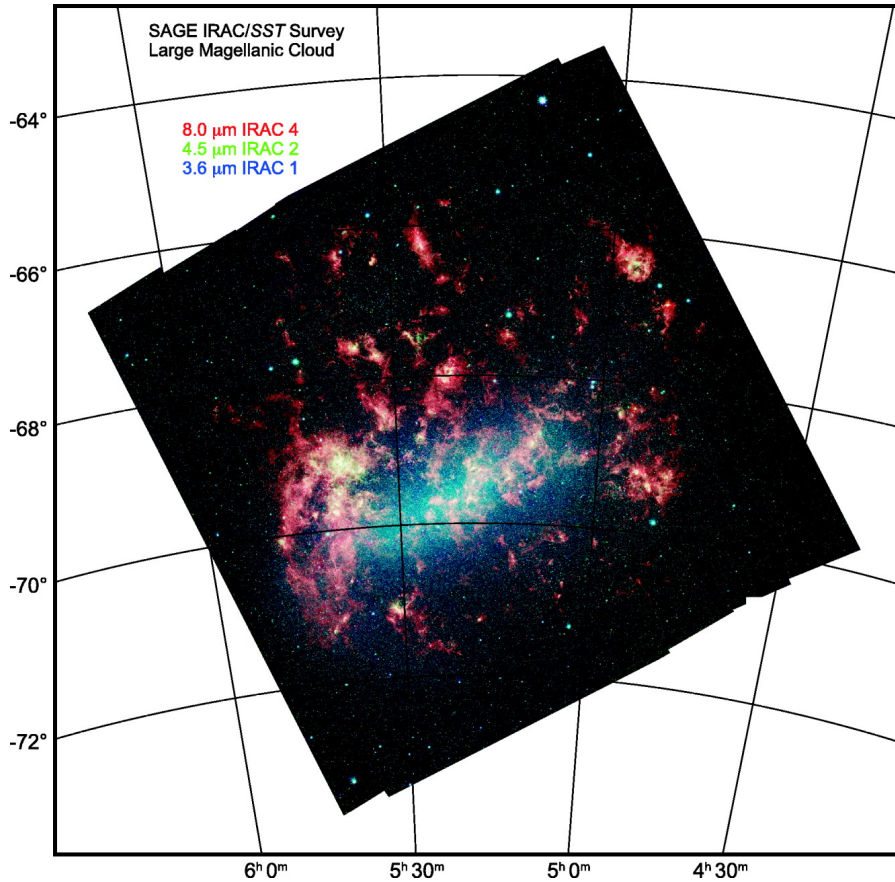


Figure 1.5: Three colour LMC mosaic from the SAGE data. The red channel shows the distribution of warm dust, while the blue channel primarily tracks the stellar content. Image taken from Meixner et al. (2006).

(Werner et al. 2004) and the *Herschel* Space Observatory (Pilbratt et al. 2010) opened the possibility to observe stars at the early stages of their evolution across wide areas. Both have been used in large MC surveys, allowing the identification and analysis of YSO populations across both the LMC and SMC. The SAGE survey (Surveying the Agents of a Galaxy's Evolution; Meixner et al. 2006) conducted with *Spitzer* has provided a panchromatic view in 3.6, 4.5, 5.8, 8.0 (IRAC, Fazio et al. 2004), 24, 70, and 160 μm (MIPS, Rieke et al. 2004) for the whole LMC. As a result, over 2000 previously unknown candidates for intermediate/high mass YSOs have been identified (Whitney

et al. 2008; Gruendl & Chu 2009; Carlson et al. 2012), based on their location in colour–magnitude (CMD) and colour–colour diagrams (CCD). Carlson et al. (2012) also fitted YSO models to the observed SEDs to acquire a high reliability sample, while Whitney et al. (2008) used YSO models on a subset of their photometrically determined selection to derive their physical properties. Spectroscopic analysis for some of these YSO candidates led to further characterization based on the dominant features in the spectra (Seale et al. 2009; Oliveira et al. 2009; Jones et al. 2017), which are thought to reflect an evolutionary sequence. The spectra of the most embedded YSOs are dominated by ices adsorbed on the dust grain surfaces and silicate features in absorption, while more evolved YSOs show PAH emission only.

The HERITAGE survey (HERschel Inventory of The Agents of Galaxy Evolution; Meixner et al. 2013) mapped the LMC and the SMC at 100, 160, 250, 350, and 500 μm . These wavelengths trace dust and the most deeply embedded Class 0 YSOs. Using the HERITAGE catalogues of point sources 3518 YSO candidates were found, out of which 2493 had a high likelihood of being genuine YSOs (Seale et al. 2014). Based on HERITAGE data an integrated dust mass of $(7.3 \pm 1.7) \times 10^5 M_{\odot}$ for the LMC was derived (Gordon et al. 2014). By comparing the dust emission with CO, H α , and HI 21 cm observations a gas-to-dust ratio of $380_{-130}^{+250} \pm 3$ was found (Roman-Duval et al. 2014), which would imply a total gas content of $\sim 3 \times 10^8 M_{\odot}$.

1.5 Project goals

This PhD project aims to answer the following questions:

- **How is the intermediate/low mass young stellar content of the LMC distributed on large scales, and what are its characteristics?**

Whilst massive OB-stars dominate the energy output and act as signposts of recent or ongoing star formation due to their short lifetimes, they are far outnumbered by their lower mass siblings. So far, low/intermediate mass PMS populations have been studied in some targeted OB-associations (see Tab. 1.1),

but very little is known about the distributed population on large scales. This project uses VMC data (Sec. 2.2) to sample and characterise these stars in an area of $\sim 1.2 \text{ kpc}^2$ known to be active in star formation (Sec 2.3). My approach is based on a statistical analysis of the stellar distribution in CMDs in order to distinguish PMS populations from the field (Chap. 3). The overall properties of these populations (e.g. age, mass) are broadly constrained by using synthetic clusters of appropriate metallicity (see Fig. 3.7). Finally, the large scale distribution of the identified young populations are also compared to the large scale distribution of gas and dust (Sec. 3.5.4).

- **Is young stellar variability affected by metallicity?**

NIR-variability is a common property in Galactic samples of young stars (Carpenter, Hillenbrand & Skrutskie 2001) to the extent that YSOs might actually dominate the NIR-variability populations at high amplitudes (Contreras Peña et al. 2017b). The investigation of young variables presented in this thesis aims at gauging the influence of environmental conditions on the variability patterns in an LMC sample of young stars. A comparison with Galactic variability studies can reveal possible differences in the global variability characteristics. Several ways of how a low metallicity environment could affect young stellar variability are presented in the last paragraph of Sec. 1.3.2. For this investigation I use the multi-epoch data of the VMC, combined with additional epochs from our own open time programme (Sec. 2.3.1). The selected sample of LMC YSOs is composed of high reliability candidates from different *Spitzer* studies (Sec. 4.5). Their lightcurves are analysed and classified based on their shape and examined for possible periodicity (Sec. 4.6.1). Lastly, I discuss the possible origins of the variability (Sec. 4.6.4), and finish with a comparison with Galactic samples.

2 Observations and data

This project uses NIR photometric data obtained from observations with the Visible and Infrared Survey Telescope for Astronomy (VISTA). In this chapter I will first describe the instrument and some of its properties, followed by a description of the observations and the data.

2.1 Properties of VISTA/VIRCAM

VISTA is a wide-field survey telescope located at ESO's Cerro Paranal Observatory in northern Chile at an elevation of 2518 m. It uses a Ritchey-Cretien design with a 4.1 m primary mirror and a 1.24 m secondary mirror, which are separated by 2.725 m (Sutherland et al. 2015). The system's focal length is 12.07 m. The compact telescope structure is shown schematically in Fig. 2.1.

The VISTA InfraRed CAMera (VIRCAM) is mounted at the Cassegrain focus. VIRCAM contains, amongst other devices, an eight slot filter-wheel and 16

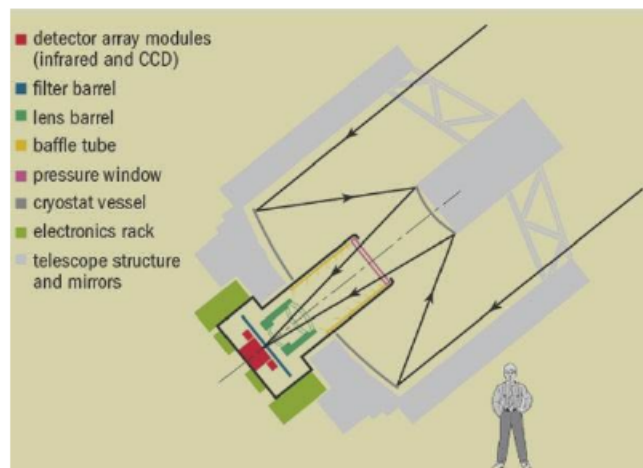


Figure 2.1: Schematic view of the VISTA telescope (Sutherland et al. 2015).

Table 2.1: Filters available with VISTA.

Filter	λ_{mean} [μm]	FWHM [μm]
<i>Z</i>	0.88	0.12
<i>Y</i>	1.02	0.10
<i>J</i>	1.25	0.18
<i>H</i>	1.65	0.30
<i>K_s</i>	2.15	0.30
NB980	0.98	0.01
NB990	0.99	0.01
NB118	1.18	0.01

NIR Raytheon detectors sensitive in the wavelength range $0.84\ \mu\text{m} - 2.3\ \mu\text{m}$ (Emerson, McPherson & Sutherland 2006). Seven slots are used for scientific filters, while one slot is reserved for a dark filter. The installed set of scientific filters comprises five broad-band and three narrow-band filters (Table 2.1), with NB980 and NB990 sharing one slot.

The physical size of the detectors is $40.96\ \text{mm} \times 40.96\ \text{mm}$, containing 2048×2048 pixels with a pixel size of $20\ \mu\text{m}^1$. At the focal plane the mean pixel size is $0.339''$ on the sky (Dalton et al. 2006). Hence, each detector covers $11.6' \times 11.6'$ resulting in a total field-of-view (FOV) of $\sim 0.6\ \text{deg}^2$ for all detectors. However, they are arranged in a 4×4 grid with considerable spacing between them (Fig. 2.2). Thus, a single exposure produces a non-contiguous image of the sky known as a pawprint. To create a contiguous image with a reasonably uniform coverage, six pawprints with a fixed offset-pattern between them are combined. The fully sampled area of the sky, i.e. with filled gaps, is called a tile and covers an area of $\sim 1.5\ \text{deg}^2$. Accounting also for areas at the tile-edges which are only covered by one single pawprint exposure, the tile FOV is $\sim 1.77\ \text{deg}^2$.

¹http://www.eso.org/sci/facilities/paranal/instruments/vircam/doc/VIS-MAN-ESO-06000-0002_v101.pdf

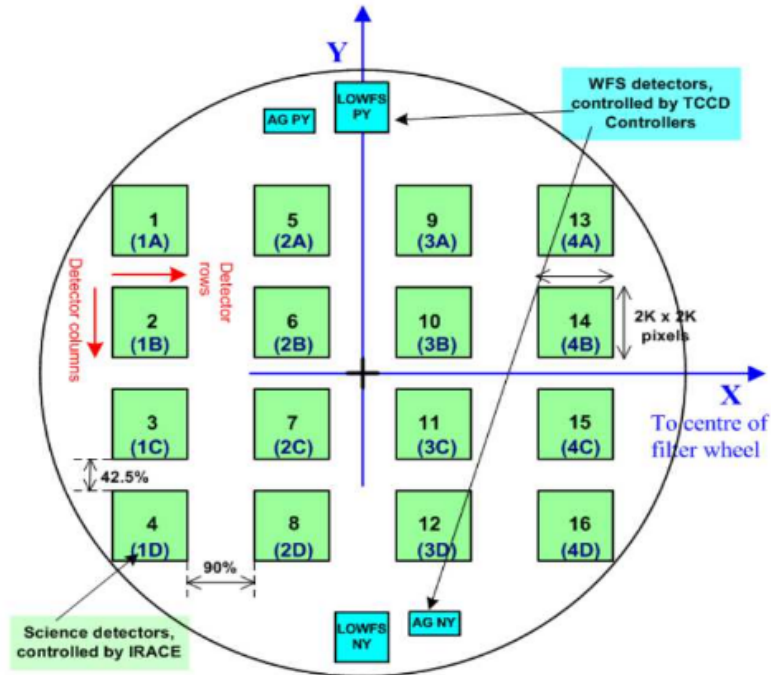


Figure 2.2: The detector plane of VIRCAM. From <http://www.eso.org/sci/facilities/paranal/instruments//vircam/inst.html>

2.2 The VMC survey

The core data for this thesis was obtained by the VISTA survey of the Magellanic Clouds (VMC; Cioni et al. 2011). The VMC is a large ESO public survey that observed an area of $\sim 170 \text{ deg}^2$ until its completion in October 2018, with a total number of 110 tiles observed. It covers the LMC (68 tiles, $\sim 105 \text{ deg}^2$), the SMC (27 tiles, $\sim 42 \text{ deg}^2$), the Magellanic Bridge (13 tiles, $\sim 21 \text{ deg}^2$), and includes also parts (2 tiles, $\sim 3 \text{ deg}^2$) of the Magellanic Stream (see Fig. 2.3). The observing strategy of the VMC involves multi-epoch imaging of tiles across the Magellanic System in the Y ($1.02 \mu\text{m}$), J ($1.25 \mu\text{m}$), and K_s ($2.15 \mu\text{m}$) bands. Every tile is observed at three epochs in Y , three epochs in J , and twelve epochs in K_s . The exposure time per epoch is 800 s in Y and J , and 750 s in K_s , leading to total exposure times of 2400 s (Y , J) and 9000 s

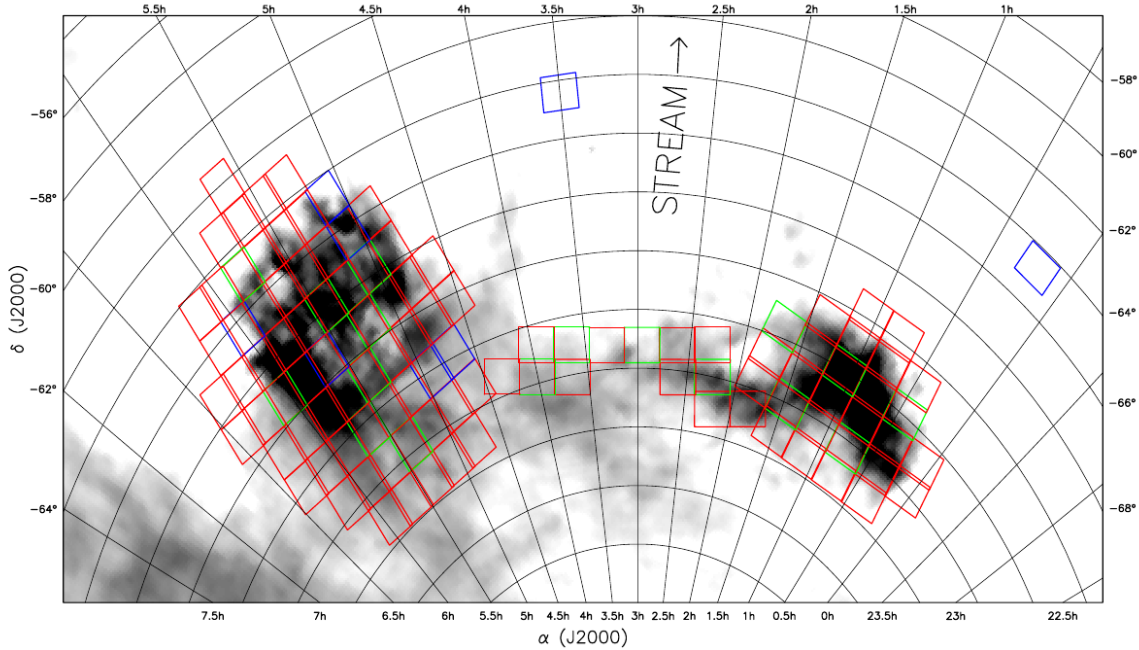


Figure 2.3: Tiling of the VMC area overplotted onto the HI distribution of the Magellanic system (Cioni et al. 2011). The colors of the rectangles indicate when the observations for the corresponding tile started. Blue: start in P85 (1 Nov 2009–31 March 2010); Green: start in P86 (01 April 2009–30 Sep 2010); Red: start after 1 Oct 2010

(K_s) in the deep stacked image of all epochs. The nominal 10σ magnitude limits are $Y \approx 21.9$ mag, $J \approx 21.4$ mag, and $K_s \approx 20.3$ mag. The corresponding limits for single epochs are 21.3 mag, 20.8 mag, and 18.9 mag, in the Y , J , and K_s band, respectively.

The primary science goals of the VMC are to resolve the star formation history of the Magellanic System and to uncover its three dimensional structure. The first objective involves a comparison of model stellar populations with the color–magnitude diagrams (CMDs) observed in the examined regions (e.g. Rubele et al. 2012; Rubele et al. 2015; Rubele et al. 2018). The 3D structure can be obtained by using the periods of RR Lyrae and Cepheid variables, which are physically linked to their absolute luminosity via Period-Luminosity, Period-Luminosity-Colour, and Period-Wesenheit relations (e.g. Moretti et al. 2014; Ripepi et al. 2017; Muraveva et al. 2018a). Other

studies using VMC data investigated background quasars (Ivanov et al. 2016), the globular cluster 47 Tucanae (Niederhofer et al. 2018), and created large-scale reddening maps (Tatton et al. 2013).

With the photometric depth, spatial resolution, and wavelength coverage in the NIR the VMC is also very useful to trace young stellar populations, as comparatively cool PMS stars and their immediate surroundings emit large fractions of their energy in the NIR range. Furthermore, NIR observations are less affected by extinction than visible light (Cardelli, Clayton & Mathis 1989). We exploit the VMC data to identify and characterise these populations (Chap. 3) for a tile rich in star forming activity (Sec. 2.3). Furthermore, we combine VMC-epochs with additional epochs from our own observing programme (Sec. 2.3.1) to investigate the variability of massive YSOs (Chap. 4) identified with *Spitzer*.

2.3 Tile LMC_7_5

We chose as target for this project the area covered by the tile LMC7_5. Its central coordinates are α (J2000) $\approx 81^{\circ}493$ and δ (J2000) $\approx -67^{\circ}895$, which is approximately $1^{\circ}7$ to the north-west of the Tarantula Nebula and to the north of the LMC bar. The coordinate range covered by this tile is approximately $80^{\circ}0 \lesssim \alpha \lesssim 83^{\circ}0$ and $-68^{\circ}6 \lesssim \delta \lesssim -67^{\circ}2$. Figure 2.4 shows the location of tile LMC7_5 within the wider environment of the LMC. This field harbours LHA 120-N 44 and LHA 120-N 51 (Henize 1956), two large star-forming complexes (e.g. Carlson et al. 2012) that are discussed in more detail in Sec. 3.5.1. They include massive OB associations like LH 60 and LH 63, in which significant populations of intermediate- and low-mass PMS stars down to $0.5 M_{\odot}$ have been identified (Gouliermis et al. 2011). Several older clusters with ages between 10 Myr and 1 Gyr are also found in this field (e.g. Glatt, Grebel & Koch 2010; Popescu, Hanson & Elmegreen 2012).

We use a photometric catalogue obtained by performing point spread function (PSF) photometry on stacked PSF-homogenized images (Rubele et al. 2012; Rubele

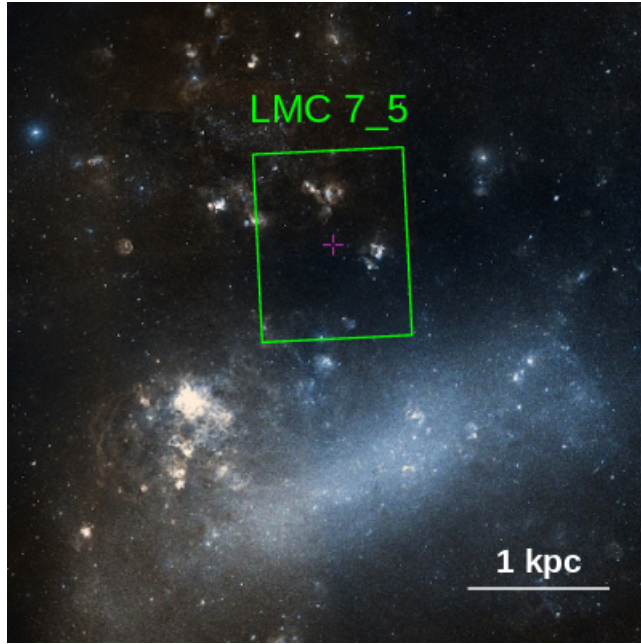


Figure 2.4: Digitized Sky Survey (DSS) image showing the location of the LMC_7.5 field within the wider LMC environment. North is up and east is to the left.

et al. 2015), which we refer to as the deep catalogue hereafter. Homogenisation is applied to obtain a uniform PSF model since seeing variations can affect the PSF shape as a function of position and time. First, homogenised pawprints are created by converting every pawprint into an image with a constant reference PSF (RPSF) model. The RPSF is generated with a half-flux radius (HFR) equal to the largest HFR of all detectors for a given pawprint. The homogenized pawprints of a given epoch are then combined into a PSF-homogenised tile image, degraded to the worst pawprint of this epoch. Finally, these tile-images are then combined (i.e. stacked).

Previous studies have shown that PSF photometry recovers more sources in crowded regions than aperture photometry (e.g. Tatton et al. 2013). PSF photometry results in deeper and more complete catalogues especially in areas with active or very recent star formation. We tested this by comparing the PSF photometry data with aperture photometry data, reduced and calibrated with the VISTA Data Flow System

(VDFS) pipeline (Irwin et al. 2004; González-Fernández et al. 2018) and retrieved from the VISTA Science Archive (VSA²; Cross et al. 2012) for six circular regions with a radius of 2'. Three regions contain young OB associations (LH 54, LH 60, and LH 63), while the other three showed no sign of recent star formation activity or stellar overdensities. The PSF photometry detects ~ 1.4 times more sources in regions without active star formation, and ~ 1.6 times more sources in the regions containing the three young associations. In addition, the deep catalogue provides estimates of the local completeness for every filter based on artificial star tests (Rubele et al. 2012). These estimates are used to correct for differences in the completeness between stellar populations from different regions (Sec. 3.2.3). For the deep catalogue a completeness of 50% is typically reached at $Y \approx 21.4$ mag, $J \approx 21.3$ mag, and $K_s \approx 20.6$ mag. The 5σ magnitude limits are $Y \approx 22.3$ mag, $J \approx 21.9$ mag, and $K_s \approx 20.9$ mag (for the nominal aperture photometry magnitude limits, see Sec. 2.2). Using the mean reddening in LMC 7.5 ($E(Y - K_s) \approx 0.18$ mag; Tatton et al., in prep.), the PSF 5σ limits correspond to PMS masses of $\sim 0.7 M_\odot$ and $\sim 1.3 M_\odot$ for ages of 1 Myr and 10 Myr, respectively.

For the variability analysis of massive YSOs (Chap. 4) we use stacked pawprint PSF-photometry of Tile LMC_7.5, which span roughly four years of VMC-observations (first observation in 2011 and last epoch was taken in 2015; see Table A.1 and Table A.2). The raw pawprint images were reduced and calibrated with the VDFS pipeline v1.3 (Irwin et al. 2004; González-Fernández et al. 2018) and the PSF photometry performed on homogenised pawprint images. The exposure times per stacked pawprint are 400 s and 375 s for the J and K_s band, respectively. Based on the fraction of pawprints in which a source is detected, the 50% completeness limits are $J \approx 20.5$ mag and $K_s \approx 18.4$ mag. An individual stacked pawprint constitutes the smallest unit of an epoch (Table A.1 and Table A.2).

²<http://horus.roe.ac.uk/vsa/>

2.3.1 Complementary observations of LMC_7_5

The VMC observing strategy was devised to enable studies of known variable objects. To extend the time baseline of the VMC and to add higher cadence observations we complement the VMC epochs by data obtained for our open time programme 0100.C-0248 (PI: V. Zivkov). The goal is to improve the sensitivity to both the long-term and short-term variability. Furthermore, the program was designed to obtain contemporaneous observations in the J and K_s band at each epoch in order to study the colour behaviour of young variables.

The observations were executed with VISTA/VIRCAM between 18 Jan 2018 and 05 Feb 2018. They added 11 contemporaneous epochs of tile LMC_7_5 in the J and K_s band using the exact same pointing and dither pattern as used in the VMC observations. Combined with the VMC-data these data-sets provide 15 and 24 epochs in J and K_s respectively, covering a baseline of ~ 6 years. The raw pawprint images were reduced and calibrated with the VDFS pipeline v1.5, and analogous to the VMC data we work with stacked pawprint PSF-photometry. For our observations the exposure times per stacked pawprint are 90s for the J band, and 480s for the K_s band. The increase in exposure time for K_s , compared to the VMC, was motivated by the results of studies which showed that variability in this filter is common amongst young stars in the Milky Way (e.g. Contreras Peña et al. 2014; Lucas et al. 2017). Hence, we maximised the depth in K_s . It also allows us to better probe high-extinction regions, where young stars tend to be located. The 50% completeness limits, determined in the same way as for the VMC data, are $J \approx 19.3$ mag and $K_s \approx 19.1$ mag. Further details can be found in Table A.1 and Table A.2.

3 PMS populations in the LMC

The work presented in this Chapter has already been published in Zivkov et al. (2018). Minor adjustments have been made and the appendix of the paper was integrated into the main text. The results of the study are unaffected by the changes.

3.1 Introduction

The data obtained by the SAGE and the HERITAGE surveys have initiated numerous large-scale star formation studies (see Sec. 1.4.1). They identified and characterised the deeply embedded YSOs, and provided a comprehensive overview of the high-mass young stellar content and their spatial distribution. However, they lack the depth and resolution for studying the intermediate- and low-mass young stellar population.

The VMC survey (Cioni et al. 2011) provides a significant improvement in depth and resolution (Sec. 2.2). Its data are being used, amongst other works, to characterise the stellar content of the MCs. Piatti et al. (2014) analysed the CMDs of known clusters in the LMC, while Piatti et al. (2016) used stellar over-densities to detect new stellar clusters in the SMC with ages between $\log(t/\text{yr}) \sim 7.5 - 9.0$. Sun et al. (2017a), Sun et al. (2017b), and Sun et al. (2018) used upper main-sequence (UMS) stars to trace large-scale structures in major star formation complexes in the LMC and SMC. They found that the size and mass distributions follow a power law, which supports hierarchical star formation governed by turbulence. Less massive PMS stars, due to their extended PMS phase (Baraffe et al. 2015), provide valuable information about the recent star formation history (see Gouliermis et al. 2012 for an overview). Identifying the PMS populations, including star formation sites only composed of intermediate- and low-mass stars, can thus reveal the full galaxy-wide extent of recent star formation.

We present an automated method that uses the capabilities of the VMC to detect intermediate- and low-mass ($1 M_{\odot} \lesssim M_{*} \lesssim 4 M_{\odot}$) PMS populations. The method is based on a colour–magnitude Hess diagram (Hess CMD) analysis, which includes

corrections for reddening and completeness, in order to distinguish young populations from the field. This chapter describes the development of this method as well as its application to a $\sim 1.5 \text{ deg}^2$ region in the LMC (Sec. 2.3). The chosen pilot field contains well-studied OB associations with known PMS populations that are used to calibrate and fine-tune the method. The chapter is organized as follows: Section 3.2 describes how we deal with the contamination from old field stars, while Sec. 3.3 explains in detail the strategy we devised to identify and categorise young populations. In Sec. 3.4 we present tests using synthetic and literature clusters to evaluate the sensitivity of the method for the cluster age and mass. We show in Sec. 3.5 first results based on the application of our method to the LMC pilot field and discuss the properties of the identified young low-mass populations. Finally, we present a summary and our main conclusions in Sec. 3.6.

3.2 Constructing differential Hess diagrams

To identify young stellar populations in the pilot field, we use the star positions in the CMD, which are indicative of their masses and ages. CMD-based methods are widely used to analyse clusters of all ages (e.g. Da Rio, Gouliermis & Henning 2009; Rubele et al. 2011; Girardi et al. 2013; Niederhofer et al. 2017). In general, observations towards clusters or associations are contaminated by the dispersed field population; it is thus necessary to apply a robust decontamination procedure. In this paper we work with $K_s/(Y - K_s)$ CMDs, since the longer wavelength baseline makes different populations easier to distinguish.

3.2.1 CMD density diagrams

We start by spatially dividing the pilot field into a grid (see Fig. 3.1). Every grid element is circular, and the distance between the centres of two neighbouring elements is one grid element radius. The resulting overlap ensures that every location is covered

by the grid. It also reduces the chance that a young cluster or association is split up between two or more neighbouring grid elements. The grid radius is a very important parameter, and it is the subject of extensive testing in this study (see Sec. 3.4). We defined grids with radii of $r = \{90'', 75'', 60'', 50'', 40''\}$. Individual $K_s/(Y - K_s)$ CMDs are constructed for each grid element. The CMDs are then smoothed using a Gaussian kernel, resulting in a 2D density map of the stellar distribution in colour–magnitude space. The widths of the kernels define the colour–magnitude resolution of our density maps; they must be small enough to highlight the distribution of different stellar populations in the CMD, but large enough to be robust against small number statistics. We apply an adaptive kernel width that depends on the number of stars in a grid element ($N_{*,\text{ge}}$) and on the photometric errors defined as follows:

$$\sigma_{K_s} = 0.2 \text{ mag} \times \sqrt{\frac{\langle N_* \rangle}{N_{*,\text{ge}}}} \quad (3.1)$$

$$\sigma_{Y-K_s} = 0.5 \times \sigma_{K_s}, \quad (3.2)$$

where $\langle N_* \rangle$ is the median number of stars in the coarsest grid. If the mean photometric error within the kernel $\Delta K_s > \sigma_{K_s}$, we adopt $\sigma_{K_s} = \Delta K_s$. The width values are typically in the ranges $0.1 \text{ mag} < \sigma_{Y-K_s} < 0.2 \text{ mag}$ and $0.2 \text{ mag} < \sigma_{K_s} < 0.4 \text{ mag}$. Kernel width maxima of $\sigma_{Y-K_s} = 0.2 \text{ mag}$ and $\sigma_{K_s} = 0.4 \text{ mag}$ are set to prevent smoothing over too large CMD regions. The smoothing procedure results in a Hess CMD for every grid element. Figure 3.2 shows representative CMDs (top) and Hess CMDs (bottom) for two grid elements containing mostly old field stars (left) and a star-forming region (right), as shown by the overplotted PARSEC¹ isochrones (Bressan et al. 2012).

¹PAдова and TRIeste Stellar Evolution Code
<http://stev.oapd.inaf.it/cgi-bin/cmd.2.7>

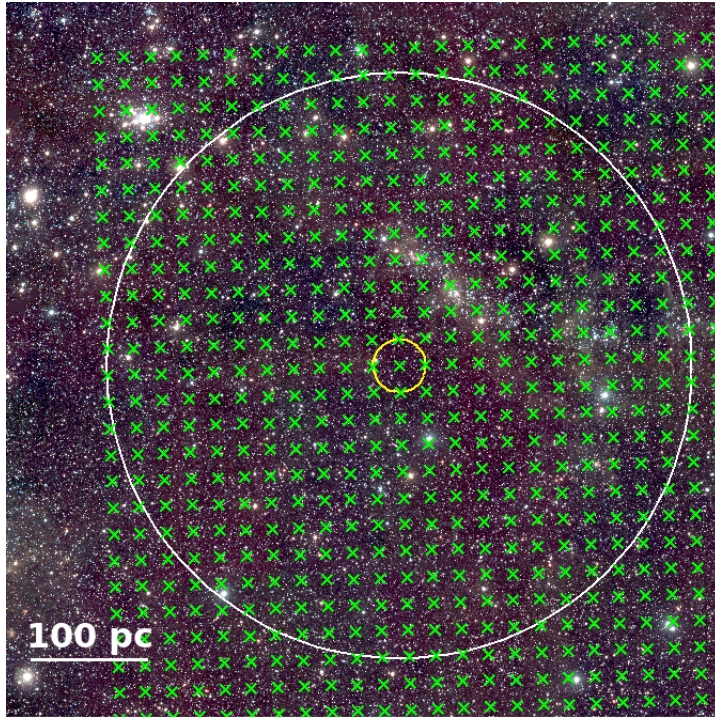


Figure 3.1: VISTA RGB composite with Y ($1.02 \mu\text{m}$) in blue, J ($1.25 \mu\text{m}$) in green, and K_s ($2.15 \mu\text{m}$) in red showing the north-eastern corner of the pilot field. Green crosses are placed at the centres of the grid elements ($90''$ radius in this instance). The small yellow circle highlights an example grid element, while the large white circle shows the area searched to identify suitable control field regions (see text).

3.2.2 Control field selection

To decontaminate each grid element from field stars, we use offset control fields that closely resemble the local field population. The total size of the pilot field precludes the use of a single control field for the whole tile, since the typical field population changes over such large spatial scales. Hence it is necessary to define control fields individually for every grid element. The approach is as follows: we count stars within the UMS and PMS regions of the CMD (shown in Fig. 3.2) for all grid elements within a distance of $1000''$ from the grid element being analysed. The UMS and PMS regions are defined primarily using PARSEC isochrones. Furthermore, the red limit for the PMS region

excludes background galaxies (Kerber et al. 2009), while the blue edge excludes most old field stars. The boundary at bright magnitudes is generous enough to allow for effects like PMS variability and IR excesses, and the lower boundary is imposed by the sensitivity of the survey. The CMD of a typical LMC field population is expected to have significantly fewer stars within the UMS and PMS regions than that of an area dominated by young stars. Star counts can thus identify grid elements that are control field candidates. An example control field search area is depicted in Fig. 3.1. The number of grid elements within this area varies, depending on the size of the elements; the coarsest grid (90'' radius) contains around 360 grid elements. We create histograms of the star counts for both the UMS and PMS regions and approximate these with Gaussian distributions.

In addition, the mean extinction towards every grid element within the control field search area is determined by using the mean observed colour of red clump (RC) stars. These are evolved stars with well-constrained luminosities, and thus the RC is often used for distance and reddening measurements (e.g. Paczyński & Stanek 1998; Tatton et al. 2013). Although population effects change the absolute magnitude of RC stars (Girardi & Salaris 2001), any variations on \ll kpc scales are generally dominated by distance differences and reddening. The selection box for the RC is also indicated in Fig. 3.2. Its slope of 0.434 is calculated based on the relative extinctions for VISTA filters, $A_Y/A_V \approx 0.390$ and $A_{K_s}/A_V \approx 0.118$ (Catelan et al. 2011). The $Y - K_s$ colour limits were chosen to keep the contamination by non-RC objects low, while still covering typical LMC reddening values (Rubele et al. 2012; Tatton et al. 2013). Assuming an intrinsic RC colour of $(Y - K_s)_0 = 0.84$ mag (Tatton et al. 2013), we probe extinction values up to $A_V \approx 4.26$ mag. The magnitude limits are such as to be insensitive to the small distance variations due to the depth of the LMC along the line of sight. We create a histogram of all mean extinction values within the control field search area, and fit it with a Gaussian distribution. Across the pilot field, the mean extinction is $A_V \approx 0.7$ mag, consistent with another determination using the RC method ($A_V \approx 0.66$ mag; Tatton et al. in prep.).

A grid element is considered a reliable control field candidate if its UMS and

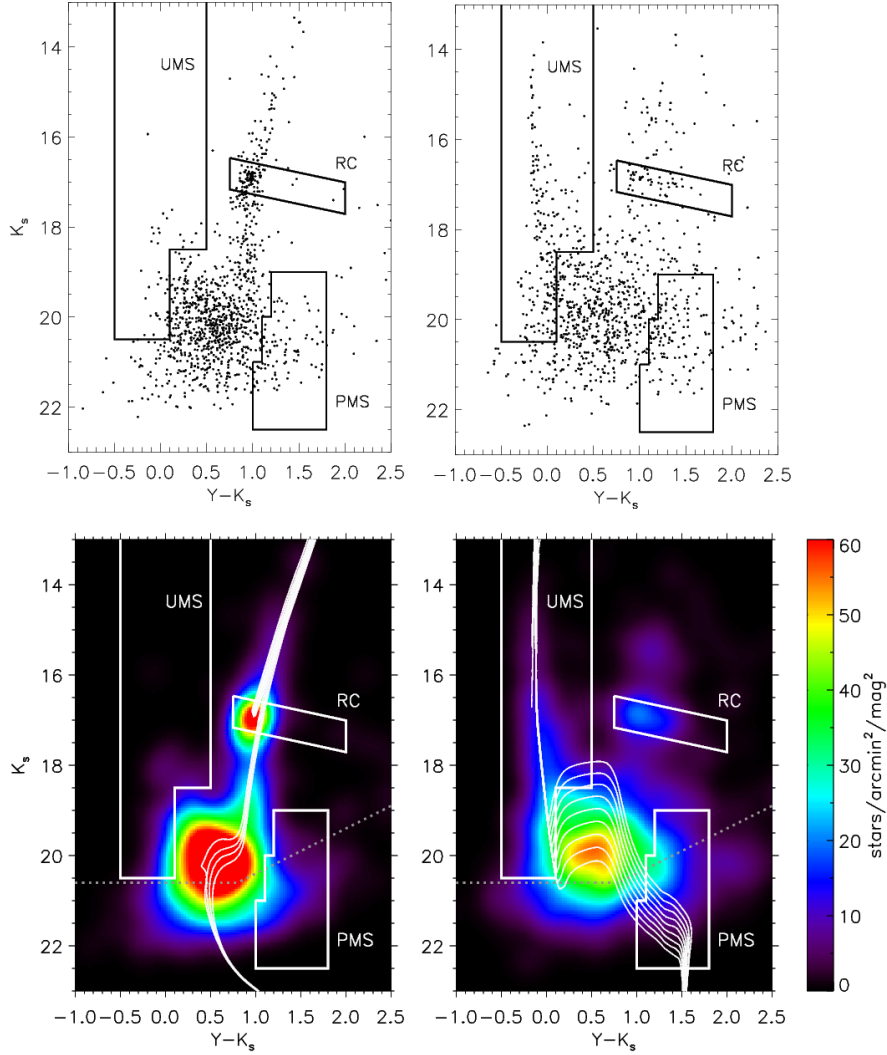


Figure 3.2: **Top:** CMDs of two example grid elements. Boxes indicate the UMS and PMS regions used in the control field selection, as well as the RC region used to determine the mean extinction (see Sec. 3.2.2 for details). The slope of the RC selection box is defined by the reddening vector. **Bottom:** Corresponding Hess CMDs. Thin solid lines are PARSEC isochrones (Bressan et al. 2012) for $\log(t/\text{yr}) \in [9.5, 9.6, 9.7, 9.8]$ and $Z = 0.0033$ (left panel), and $\log(t/\text{yr}) \in [6.0, 6.1, 6.2, 6.3, 6.4, 6.5, 6.6, 6.7, 6.8]$ and $Z = 0.008$ (right panel). The assumed metallicities are typical for the age ranges (Rubele et al. 2012; Tatton et al. 2013). The isochrones are shifted by a distance modulus of 18.49 mag (de Grijs, Wicker & Bono 2014), and an extinction correction derived from the RC analysis (see text) is applied. The dotted line marks the typical 50% completeness level.

PMS counts, and mean extinction are within 1σ from the mean value of the respective Gaussian distributions. Usually, over 100 suitable control field candidates are found within any given $1000''$ search area (61 is the minimum). The algorithm automatically selects the N nearest control field candidates and combines them into a master control field. The chosen value for N depends on the grid radius: $N = 10, 14, 20, 28,$ and 40 for the $90'', 75'', 60'', 50'',$ and $40''$ grids, respectively. These values provide a good balance between computing time and well-sampled control field populations.

3.2.3 CMD residuals and significance maps

In order to compare the stellar content of a grid element to that of the respective master control field, it is necessary to correct for differences in the reddening, since reddened main-sequence stars can occupy the same region in the CMD as PMS stars. Using the mean extinction values determined in Sect. 3.2.2 is not appropriate since it would not account for differential reddening. Instead, the magnitudes of the stars in the control fields are individually corrected. We start by determining the cumulative colour distribution of stars in the RC box (as defined in Sec. 3.2.2) for each grid element and the corresponding master control field (Fig. 3.3). For every control field star a random number is generated. This number is taken as a percentile in the cumulative distributions of the RC stars; each star is in turn dereddened by the corresponding $E(Y - K_s)$ in the colour distribution of the control field, and subsequently reddened by the corresponding $E(Y - K_s)$ in the colour distribution of the grid element. By shifting all stars from the control field along the reddening vector so that both RC colour distributions closely match each other (Fig. 3.3), any reddening differences between the grid element and its control field are minimised.

Figure 3.3 shows how this correction is performed. The blue line represents the cumulative colour distribution of RC stars in the control field. Since the control field combines several grid elements, it contains many RC stars. This creates a very smooth distribution. The steep slope indicates a compact RC with little differential reddening. The black line shows the cumulative distribution for the grid element being studied.

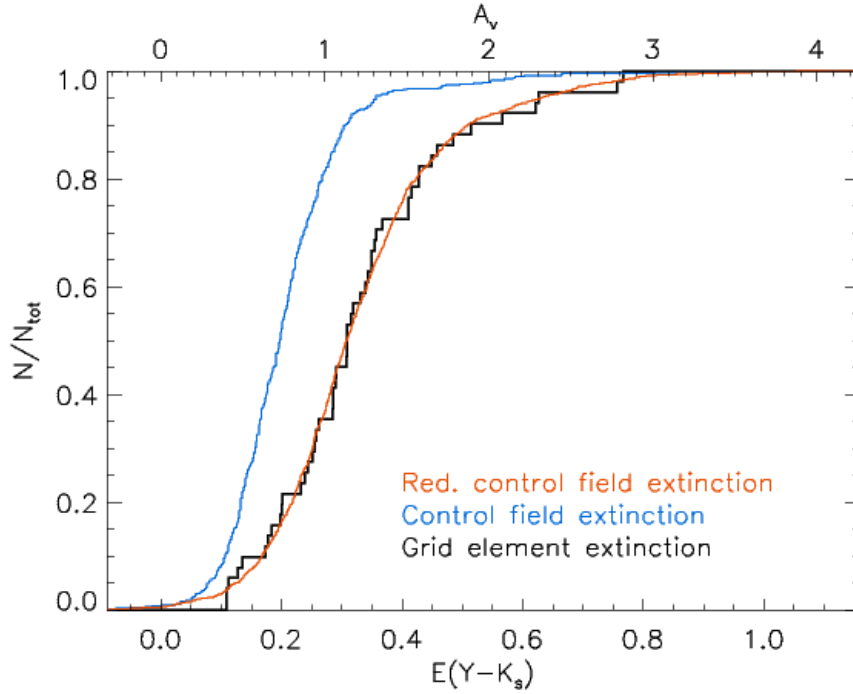


Figure 3.3: Cumulative colour distribution of RC stars for the grid element under investigation (black line), and for the corresponding control field before and after the reddening correction (blue and red lines, respectively). RC stars are defined by the RC selection box in Fig. 3.2. The intrinsic RC colour adopted is $(Y - K_s)_0 = 0.84$ mag (Tatton et al. 2013).

Its slope is shallower because the RC is more spread out. Especially the top $\sim 25\%$ of the most strongly reddened stars suggests substantial differential reddening. After the reddening correction is applied to the control field population, its RC distribution (red line) closely follows the grid element RC distribution. Differential reddening is accounted for, which would not have been possible by simply adopting a fixed reddening value for the control field stars.

Since the reddening procedure shifts control field stars to fainter magnitudes and redder colours, its completeness values need to be adjusted. Even if the areas considered display similar extinction levels, there can be differences in the completeness due to crowding. We compare the original deep catalogue completeness of each control field

star to the average completeness of stars located in the vicinity of its shifted CMD position (in the grid element being studied). Control field stars are assigned a weight equal to the ratio of the original and shifted completenesses. Weights smaller than unity lead to lower densities in the Hess diagram, simulating the fact that fewer stars would have been detected.

A Hess CMD is generated for the reddened master control field in a similar way as for the corresponding grid element (Sec. 3.2.1), but using a convolution of completeness weights and Gaussian kernel in the smoothing process. Finally, the Hess CMD of the reddened control field is subtracted from that of the grid element analysed. The result is a differential Hess CMD (henceforth residual map) in which differences between specific stellar populations and the local field population stand out as density excesses (examples in the top panels of Fig. 3.4).

We use Poisson statistics to obtain the significance of any density excesses in the residual maps. If n_{ge} and n_{cf} are the density values at a specific location in the Hess diagram for the grid element and the control field, respectively, then the density excess is simply $n_{ge} - n_{cf}$; the individual statistical uncertainties are $\sqrt{n_{ge}}$ and $\sqrt{n_{cf}}$, which gives a total uncertainty of $\sqrt{n_{ge} + n_{cf}}$ for the residual. The statistical significance in the residual is thus

$$\sigma_{\text{residual}} = \frac{n_{ge} - n_{cf}}{\sqrt{n_{ge} + n_{cf}}}. \quad (3.3)$$

This significance is computed for every point in the residual map, creating an associated significance map. Figure 3.4 (bottom panel) shows an example significance map. We apply the algorithm to the five grids with different radii; for every element in each grid a residual map and a significance map are obtained.

3.3 Identifying candidate young regions

We developed a procedure that analyses the residual and significance maps, flagging and categorising candidate regions. This was extensively tested by comparing the significance maps from grid elements containing the well-studied associations LH 60

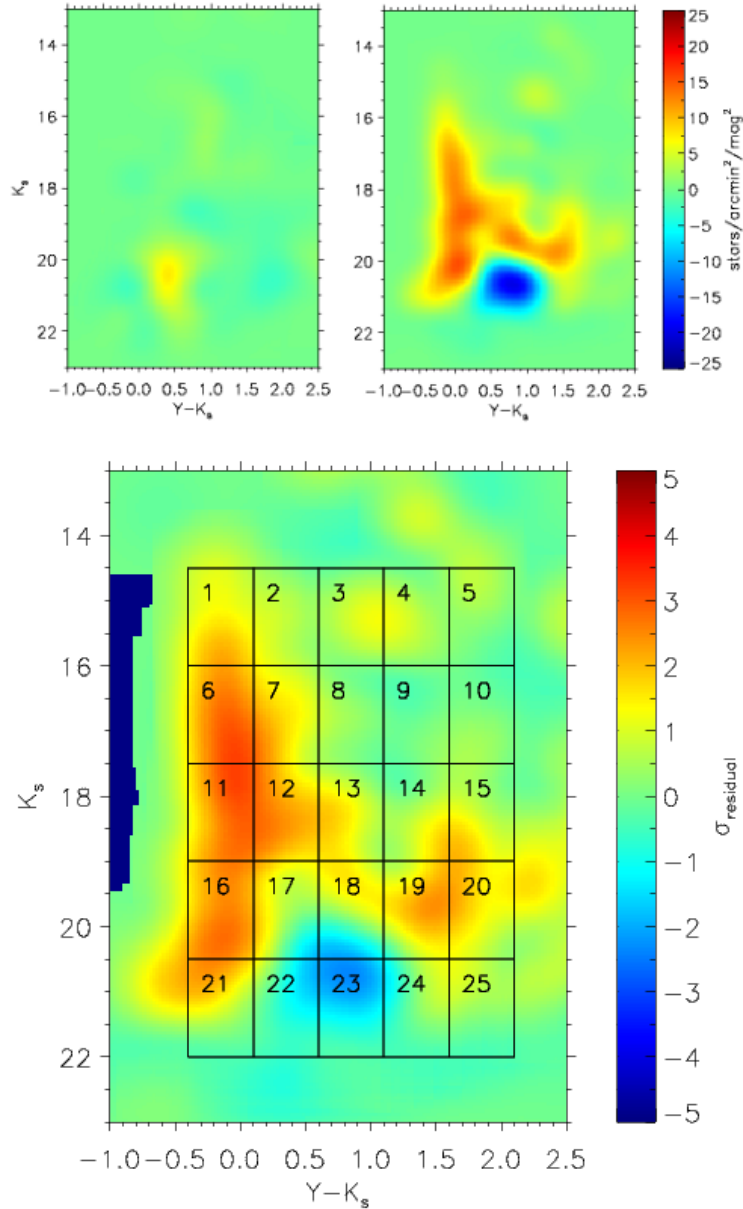


Figure 3.4: **Top left:** Residual map generated for a grid element showing no significant density excesses, leading to a featureless residual map; such a grid element is thus dominated by the old LMC field population. **Top right:** Residual map for a grid element that includes the OB association LH 63. Significant density excesses can be seen across the CMD, which is due to the presence of massive OB and PMS stars. **Bottom:** Significance map for the same LH 63 region with 25 CMD boxes overlaid; these are used to classify candidate regions based on observed density excesses (see Sec. 3.3).

and LH 63, and a nearby control field (Gouliermis et al. 2011). Figure 3.4 (top) shows residuals for the control field (left) and a grid element that contains LH 63 (right). The bottom panel shows the significance map that results from applying Eq. 3.3 to the LH 63 residual. It displays extended areas with significances > 2 at CMD locations that are indicative of the presence of young UMS and PMS stars.

A prominent blue patch is also noticeable, suggesting a field over-subtraction, where one would expect faint main-sequence stars. This feature is likely caused by small-scale variations in the completeness that are due to crowding, which are not accurately accounted for in our method. The dark blue areas at the edge of the map are artefacts caused by the absence of stars at these CMD positions for the grid element and the corresponding control field.

We divide the colour–magnitude space into 25 boxes (Fig. 3.4 bottom panel), which are analysed separately. A box is flagged when the average statistical significance is higher than a predefined threshold. The threshold value is chosen to balance sensitivity to less populous associations and robustness against statistical fluctuations. To find an appropriate threshold, we analyse the distribution of the average significances in all CMD boxes across the whole tile. This distribution is approximated by a Gaussian, and the width σ describes the typical statistical fluctuation. We use either 2.5σ or 3σ as the flagging threshold (details to follow).

Depending on their properties (i.e. age and total mass), stellar populations create density excesses above the local field population in different areas of the significance maps. We analysed the residuals and significance maps for example regions with known young populations. Gouliermis et al. (2011) constructed catalogues of candidate PMS and UMS stars for LH 60 and LH 63 (age 3 – 5 Myr), based on a statistical analysis of HST photometry in the $F555W$ and $F814W$ filters. After correcting for a systematic difference of $0.42''$ in RA, we cross-correlated the HST catalogues with the deep catalogue using a conservative $0.3''$ matching radius. We further compared the magnitudes of the matched pairs in the VISTA Y filter and in the HST $F814W$ filter. The transmission curves of these filters are similar enough for these magnitudes to be comparable. For the matched pairs ($F814W - Y$) is on average 0.43 mag, with a

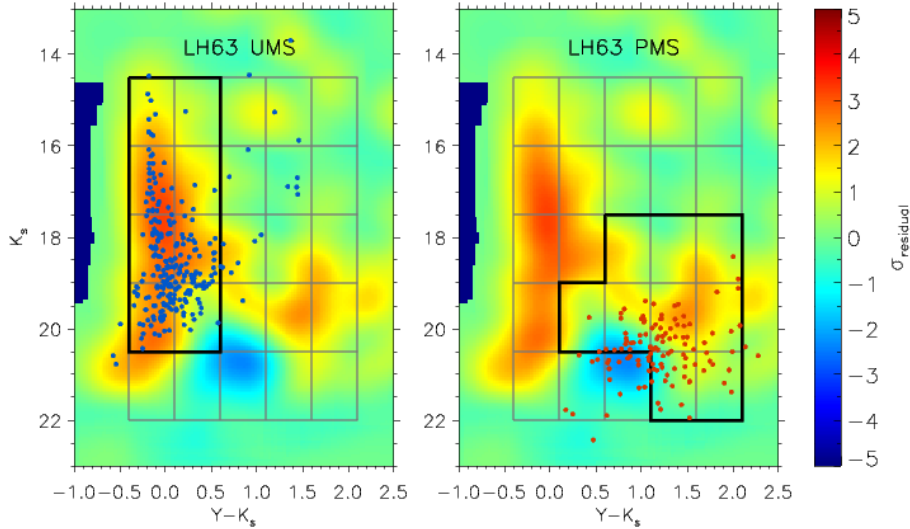


Figure 3.5: Same significance map in the background as shown in Fig. 3.4 (bottom). Blue and red symbols display VMC sources that are successfully matched to the LH63 UMS (left) and PMS (right) catalogues from Gouliermis et al. (2011). Thick black lines highlight the boxes relevant for the UMS and PMS classifications, respectively (see also Fig. 3.6).

dispersion of 0.86 mag. To select a clean sample, pairs with $(F814W - Y) \geq 2$ mag were excluded.

In LH60 we found 112 and 174 VMC counterparts to the HST PMS and the UMS sources, respectively. For LH63 the corresponding numbers are 125 and 269². Figure 3.5 shows the VMC counterparts for the LH63 UMS and PMS catalogues, with the significance map shown in the background. A clear gap is visible between the two populations, since the HST catalogue excludes areas in the optical CMD that are heavily contaminated by field stars. Clearly, the UMS matches coincide very well with areas of statistically significant density excesses; the highlighted CMD boxes (Fig. 3.5 left) cover the majority of UMS matches and the corresponding density excesses. Overall, 237 out of 269 UMS matches are located within these eight boxes; some matches are

²Based on a catalogue matching with shifted coordinates, we estimate that $\sim 3\%$ of the UMS matches and $\sim 10\%$ of the PMS matches are spurious.

located near the red giant branch and are likely contaminants in the UMS catalogue (Gouliermis et al. 2011).

The situation is more complicated for the PMS matches. Some matches fall on the strong negative density excess described previously; we did not use this part of the CMD to identify PMS populations precisely to avoid severe contamination by main-sequence stars. The large scatter in the CMD distribution of the PMS matches can be due to photometric errors and/or young stellar variability (e.g. T Tauri stars or FU Orionis variables; Contreras Peña et al. 2014; Rice et al. 2015). In addition, the PMS population could have either an age spread, or it could consist of multiple populations with different ages, similar to what has been seen in Orion (Beccari et al. 2017). Nevertheless, the regions with the most significant density excesses suggest a PMS distribution that is brighter than the distribution of HST-matched stars. Two effects likely contribute to this. Firstly, small-scale completeness variations can be significant in crowded regions like LH 63 (see Sec. 3.2.3). This can lead to over-subtraction during the control field decontamination process, which eliminates a potential density excess due to faint PMS stars. Secondly, the HST PMS catalogue included mostly relatively faint PMS stars ($F814W \geq 21.2$ mag). The density excess seen in our maps includes brighter PMS candidates excluded from HST optical catalogues. Using the location of the PMS matches and the location of the typical density excesses seen in the residual maps of known young associations, we selected the CMD boxes highlighted in the right panel of Fig. 3.5 as PMS indicators. Ninety-six out of 125 PMS matches are within this area, and overall, around 85% of the HST–VMC counterparts are located within the outlined UMS and PMS boxes.

Using these contiguous regions in the CMD that are indicative of the presence of specific populations, we classify each grid element based on which boxes are flagged in its significance map. Four classifications are adopted:

1. **UMS-only:** At least two adjacent boxes are flagged in the UMS CMD region. Figure 3.6 (left) shows a typical example of this classification. It covers a broad age range from ~ 10 to ~ 300 Myr. Based on artificial cluster tests (see

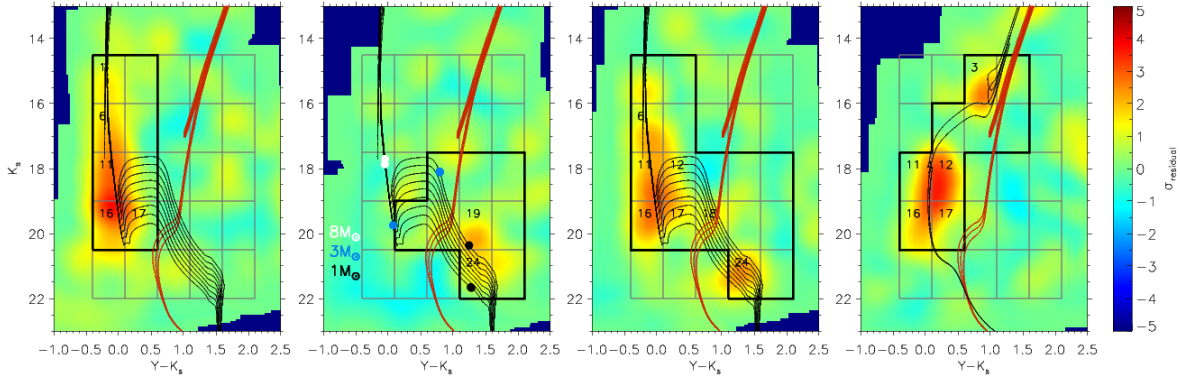


Figure 3.6: **From left to right:** Significance maps for grid elements classified as UMS-only, PMS-only, UMS+PMS, and “old”. The CMD boxes relevant for each classification are highlighted. Boxes that are flagged in the particular significance map are numbered. PARSEC isochrones (Bressan et al. 2012) are shown in all panels. Red isochrones represent ages from $\log(t/\text{yr}) = 9.6$ to 9.8 , with a metallicity of $Z = 0.0033$ (Tatton et al. 2013); they show the typical location of the old LMC field population. Black isochrones represent young populations from $\log(t/\text{yr}) = 6.0$ to 6.8 ($Z = 0.008$; Rubele et al. 2012). The two black isochrones in the rightmost panel represent populations of $\log(t/\text{yr}) = 8.5$ and 8.6 ($Z = 0.008$). All isochrones are reddened according to the mean extinction for that particular grid element (Sect. 3.2.2). In the second panel the theoretical positions for stars of three different masses are shown (colour-coded circles) for the youngest and oldest black isochrones.

Sec. 3.4.1), a minimum cluster mass of $\sim 500 M_{\odot}$ is needed to reliably flag two UMS boxes. For populations younger than 10 Myr, the PMS population is also detectable, changing its classification to UMS+PMS (see below). Beyond ~ 300 Myr, sufficiently massive clusters ($> 1000 M_{\odot}$) create a significant red giant excess, which will trigger the classification “old”.

2. **PMS-only:** At least two adjacent boxes are flagged in the PMS CMD region (second panel in Fig. 3.6). This classification traces young (< 10 Myr), low-mass clusters and associations up to around $\sim 500 M_{\odot}$. While the PMS phase for stars with masses $\lesssim 0.5 M_{\odot}$ can last up to 100 Myr (e.g. Tout, Livio & Bonnell 1999), PMS populations older than ~ 10 Myr are too faint to be detected in the VMC survey. Young clusters and associations with masses above

$500 M_{\odot}$ also flag boxes typical of UMS populations, changing the classification to UMS+PMS.

3. **UMS+PMS:** A grid element is classified as UMS+PMS if a total of at least three boxes in both the typical PMS and UMS CMD regions are flagged. Adjacency is not strictly enforced, since a minimum of three flagged boxes always leads to reasonable combinations. The same age range as in the PMS classification is probed (< 10 Myr), but the clusters and associations are more massive, since enough massive stars need to be present to flag UMS boxes. Examples for this classification are shown in Fig. 3.6 (third panel) and Fig. 3.4.
4. **Old:** This classification requires a minimum of three flagged boxes in the red giant branch and the fainter parts of the UMS CMD region. The flagging threshold for the red giant branch boxes is 2.5σ (compared to 3σ for the other boxes). We found in tests with synthetic and real clusters that this threshold reduction improves our ability to classify old clusters, without a noticeable increase in the number of false positives. Grid elements with clusters older than ~ 300 Myr and more massive than $\sim 1000 M_{\odot}$ fall into this classification (Fig. 3.6, right).

3.4 Testing the identification strategy

3.4.1 Synthetic clusters

To assess the sensitivity of this procedure to young populations of different masses and ages, we ran tests using synthetic clusters. To generate the synthetic clusters, we used the Popstar Evolutionary Synthesis Code (Mollá, García-Vargas & Bressan 2009) and adopted a Kroupa IMF (Kroupa 2001; Kroupa 2002). There is no conclusive evidence that the IMF in the LMC is significantly different from the Galactic IMF (for $M > 1 M_{\odot}$; Gruendl & Chu 2009; Liu et al. 2009a; Liu et al. 2009b), with the possible exception of 30 Doradus (Schneider et al. 2018b). NIR photometry for the VISTA filter

set was obtained using PARSEC models (Bressan et al. 2012). Synthetic clusters were generated for the following mass and age combinations:

- $M_{\text{cl}} \in [250 M_{\odot}, 500 M_{\odot}, 1000 M_{\odot}, 2000 M_{\odot}, 3000 M_{\odot}]$
- $\log(t/\text{yr}) \in [6.0, 6.3, 6.7, 7.0, 7.5, 8.0, 8.5, 9.0]$.

The cluster masses are representative of LMC clusters within this age range (de Grijs & Anders 2006). We also adopted the canonical LMC metallicity of $Z = 0.008$. For every mass–age combination, ten clusters were created. Incompleteness was applied and photometric errors added to match the quality of the VMC data before injecting the clusters into the deep catalogue. All clusters were seeded in control-field-like grid-elements with flat significance maps. Each synthetic cluster was fully contained within a grid element, a reasonable assumption given that even the smallest elements have a physical radius of 10 pc ($1 \text{ pc} \cong 4''$ at the LMC distance). The enhanced deep catalogues for every synthetic cluster were ingested into our algorithm, and the resulting residuals and significance maps were evaluated. If a synthetic cluster was classified into one of the four classes defined in Sec. 3.3 and in agreement with the cluster input properties, it is considered to be reliably identified.

In Fig. 3.7 we show examples of significance maps generated from observed data, compared with maps generated from synthetic clusters. The top left panel shows a PMS-only classified element with a clear PMS signal and no UMS excess. This suggests the presence of a very young, low-mass population. A synthetic population of $250 M_{\odot}$ with an age of 1 Myr generates a very similar significance map. The bottom left panel contains the significance map for a UMS+PMS classified element. A synthetic stellar population of $1000 M_{\odot}$ with an age of 5 Myr creates a similar significance map. Since at 5 Myr many PMS stars fall below the sensitivity limit, the PMS signature is relatively weak.

Fig. 3.8 shows the results of our synthetic cluster tests. In the top panel the detection rates for the different grid element radii for $500 M_{\odot}$ clusters of various ages are presented. While for the $90''$ radius clusters of this mass are rarely detected, the percentages increase steadily for smaller radii. At a radius of $40''$ the detection rates

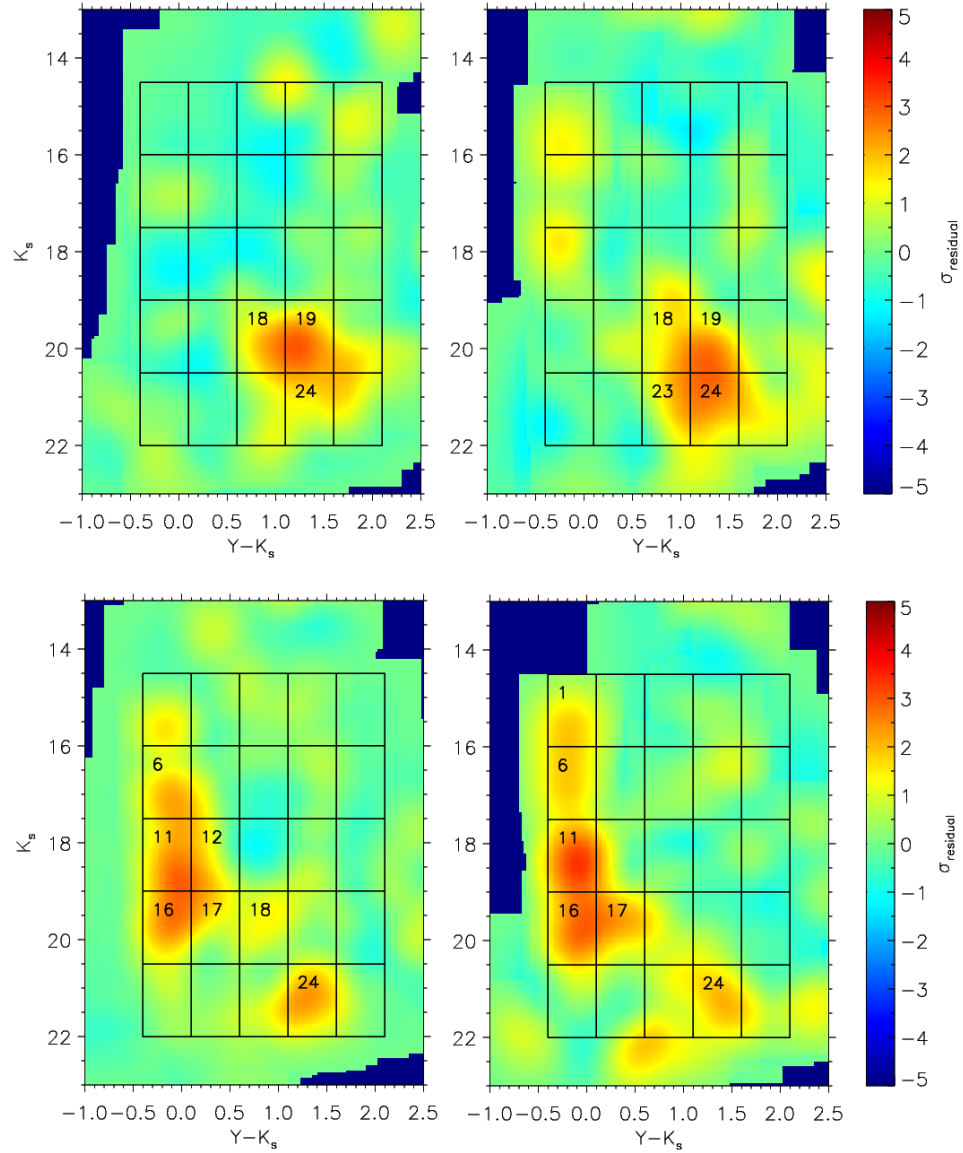


Figure 3.7: **Top:** Significance map for a PMS-only classified grid element (left) is compared to a synthetic stellar population of $250 M_{\odot}$ and 1 Myr (right). **Bottom:** Similar to the top, but showing a UMS+PMS classified grid element (left) and a synthetic stellar population of $1000 M_{\odot}$ and 5 Myr (right). Flagged boxes are numbered in each map.

are at least 60% for ages where one would expect to find PMS stars. The bottom panel shows the results obtained using the $40''$ grid for four different cluster masses in more detail. For masses $\geq 1000 M_{\odot}$, clusters are always detected, with a drop in detection rate only noticeable at 1 Gyr. For lower masses, the detection rate drops steadily with age. This is due to a decrease of flagged UMS boxes with increasing age, as more massive stars evolve away from the main sequence onto the red giant branch. At these cluster masses, this does not necessarily trigger the flagging of boxes that lead to the “old” classification. For ages $\lesssim 10$ Myr, the majority of $500 M_{\odot}$ clusters are detected. Even though the detection rate drops sharply for masses $< 500 M_{\odot}$, it remains high for very young ages.

These tests reveal three clear trends. Rather obviously, the more massive a synthetic cluster at any given age, the higher the probability of a reliable detection. Secondly, with smaller grid element radius, the probability of detection for a given synthetic cluster mass and age increases. The reason is that the same number of synthetic stars cause a higher density excess in the residuals of smaller grid elements, leading to a higher flagging probability. Thirdly, the detection rates generally decrease with age. The luminosity of intermediate- and low-mass PMS stars decreases as they approach the main sequence. Hence, an increasing fraction of PMS stars falls below the sensitivity limit of the VMC survey for progressively older ages.

Table 3.1 presents an overview of the most common classifications for synthetic clusters of different age and mass ranges. The decrease of detectable PMS stars with age causes an increase in the minimum cluster mass that is necessary to detect a PMS signature. Beyond 10 Myr, the VMC survey is not sufficiently deep to reliably detect any remaining PMS stars. Therefore, all detected clusters are classified either as UMS-only or as “old”. The tests reveal that massive ($\gtrsim 2000 M_{\odot}$) clusters within the age range 30 Myr – 1 Gyr can be mis-classified as UMS+PMS, and thus contaminate the UMS+PMS class. However, the level of contamination is 2.5% at most.

In summary, we conclude that for a given mass, a cluster or association is easier to detect and classify at a young age (preferably < 10 Myr); this is mostly due to the sensitivity and completeness limits of the VMC survey. While $\sim 28\%$ of detected

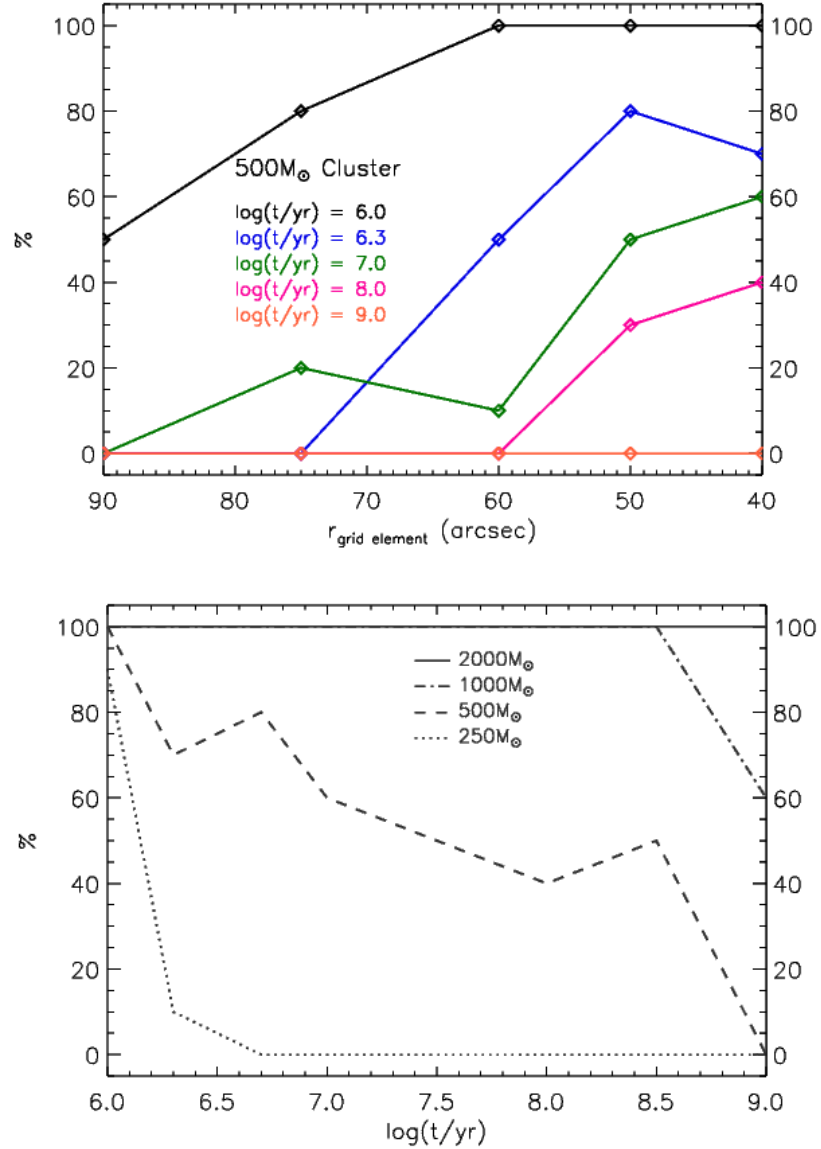


Figure 3.8: **Top panel:** Detection percentages for 500 M_⊙ clusters of different ages for grid-element radii from 90'' to 40''. A general increase in detection rates with decreasing radius is noticeable. A decrease in detection rates with increasing cluster age is evident as well. **Bottom panel:** Detection percentages for clusters of four different masses across the age range from 1 Myr to 1 Gyr for the 40'' radius. A decrease in sensitivity for older ages and lower masses is apparent. Clusters more massive than 500 M_⊙ show high detection rates for young ages.

Table 3.1: Most likely classifications for mass and age ranges based on synthetic cluster tests.

	< 2 Myr	2 – 5 Myr	5 – 10 Myr	10 – 300 Myr	> 300 Myr
< 500 M_{\odot}	PMS-only	-	-	-	-
500 – 1000 M_{\odot}	UMS+PMS	UMS+PMS	UMS-only	UMS-only	UMS-only
> 1000 M_{\odot}	UMS+PMS	UMS+PMS	UMS+PMS	UMS-only	old

clusters with age 10 Myr have a PMS signature leading to a PMS-only or UMS+PMS classification, this fraction increases to $\sim 66\%$ for 5 Myr-old populations and $\sim 98\%$ for very young ages (≤ 2 Myr). More massive clusters are obviously more likely to be identified. Another important result is that finer grids are better suited to finding low-mass clusters, despite the effects of small number statistics due to the decreasing number of stars per grid element.

3.4.2 Literature clusters

The synthetic cluster tests provided valuable results about the mass and age ranges that are effectively traced with our method. However, as these synthetic clusters were only injected into the deep catalogue rather than into the images, information on the sensitivity to different cluster radii and star count density profiles is lacking. We compiled a list of 31 clusters and associations from the literature (Gouliermis et al. 2003; Glatt, Grebel & Koch 2010; Popescu, Hanson & Elmegreen 2012). Our list is not a complete census of clusters in the pilot field, but provides a reliable sample of clusters with different ages and sizes. The selected systems span an age range from a few Myr up to around 1 Gyr, and apparent sizes from $10''$ to over $100''$ (sizes were estimated visually from the VMC images).

Table 3.2 shows how many clusters are classified as a function of grid element radius. With decreasing grid element size, the number of unclassified clusters decreases monotonically. This trend is in line with the results from the synthetic cluster tests,

Table 3.2: Number of classified clusters from the sample of 31 clusters from the literature as a function of grid element radius.

	90''	75''	60''	50''	40''
classified	20	23	23	24	25
unclassified	11	8	8	7	6

where an increasing sensitivity for the finer grids was observed. For the finest grid, 25 out of 31 literature clusters are classified with our method. For 23 of these, their classifications and inferred broad age range (see Table 3.1) are consistent with published literature ages. The two remaining clusters have literature ages of $\log(t/\text{yr}) \sim 7.8$; since an RC signature is detected, our method classifies these clusters as old, implying an age $\gtrsim 300$ Myr.

Six unclassified clusters remain, four of which flag a single CMD box. Since this does not trigger a classification, these four clusters are at the sensitivity limit of the 40'' grid. The unclassified clusters are either spatially small compared with the grid element and/or are relatively old (based on their literature ages). Two of the six unclassified clusters are the smallest in our list with radii of 10'' and 14'', $\sim 6\%$ and $\sim 12\%$ of a grid element area. This indicates that our method is mostly sensitive to clusters with $r \gtrsim 3$ pc at the LMC distance. For four of the six unclassified clusters, the literature age is in the range $7.3 \lesssim \log(t/\text{yr}) \lesssim 8.7$. The stellar populations of old clusters move towards areas in the CMD that are more heavily contaminated by the old field population, further decreasing the sensitivity. This confirms the results from the synthetic cluster tests that comparatively old systems have lower detection rates. Given that our stated goal is to identify young populations, a decrease of detection rate with cluster age is not an issue.

3.4.3 Final choice of grid element radius

Our analysis clearly advocates the use of the 40'' radius grid because of its increased sensitivity. A further decrease in radius leads to grid elements without any RC stars, impairing the ability of the method to correct for reddening differences between a grid element and its control field. On average, a 40'' grid element is populated by 265 stars, with 171 stars being the minimum. Our subsequent analysis focuses on the optimal 40'' radius grid.

3.5 Results

Applying our method to the deep catalogue from the pilot field provides the residual and significance maps, flagged boxes, and classification for every grid element. For the 40'' grid, 10,730 grid elements are unclassified, 298 are classified as UMS-only, 84 as PMS-only, 124 as UMS+PMS, and finally, 14 are classified as “old”.

3.5.1 Spatial distribution of the young populations

3.5.1.1 Global properties

Figure 3.9 shows the spatial distribution of the 208 grid elements with a significant PMS contribution (classified as UMS+PMS and PMS-only, cyan and yellow crosses, respectively). These grid elements are not distributed uniformly, but instead concentrate in areas with enhanced dust emission as traced by *Spitzer* in the IRAC 8.0 μm band (Meixner et al. 2006). Around 80% of them are found in three main regions: N 44, N 51, and N 148 (see Fig. 3.11 for a detailed view). N 44 and N 51 are well-studied large star formation complexes (e.g. Carlson et al. 2012). Almost all classified elements associated with these complexes are located within regions of about 290 arcmin² ($\sim 65, 200 \text{ pc}^2$) and 380 arcmin² ($\sim 85, 500 \text{ pc}^2$). On these spatial scales, star formation complexes contain young populations formed in multiple and/or extended star forma-

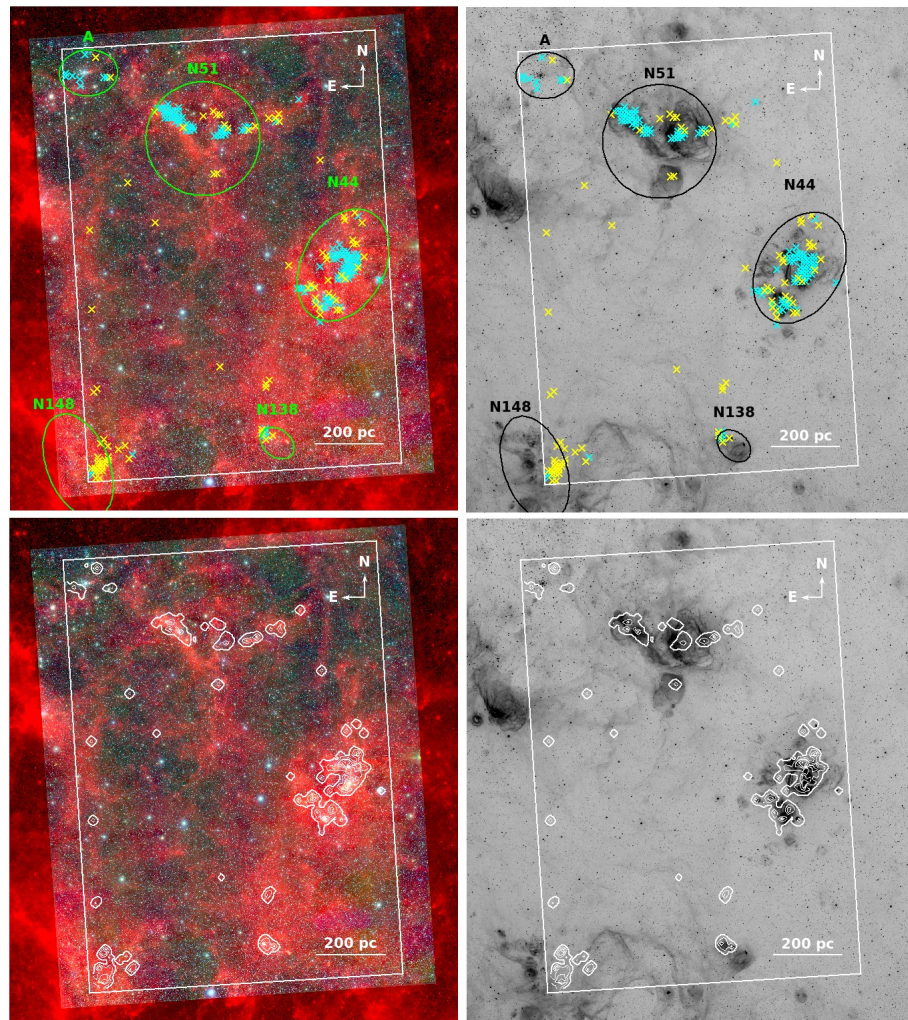


Figure 3.9: **Top left:** Three-colour composite image with VMC Y (blue) and K_s bands (green), and *Spitzer* IRAC $8.0\ \mu\text{m}$ (red). The rectangle shows the region covered by our analysis. Small crosses mark the centres of grid elements for the $40''$ grid that are classified as PMS-only (yellow) or UMS+PMS (cyan). Several prominent regions are highlighted and labelled (spatial sizes according to Bica et al. 2008) and discussed further in Sec. 3.5. **Top right:** Inverted grey-scale map of $\text{H}\alpha$ emission (Smith et al. 2005). **Bottom:** PMS density contours for elements classified as PMS-only or UMS+PMS derived from the residual maps of the grid elements. The outermost contour represents $\Delta n_{\text{PMS}} = 2.4\ \text{stars arcmin}^{-2}$ (see Sec. 3.5.3 for details); every subsequent contour represents an increase in density by $3 \times \Delta n_{\text{PMS}}$.

tion events (see Gouliermis 2018 for a detailed review). For comparison, the HTTP survey of the 30 Doradus region covers $\sim 168 \text{ arcmin}^2$ (Sabbi et al. 2013), within which Schneider et al. (2018a) found evidence for complex spatial and temporal substructure amongst the massive stars. Towards the south-eastern corner of the field lies another concentration of classified elements associated with N 148, which is also prominent in CO (Wong et al. 2011) and dust emission (Meixner et al. 2006). A fourth group is situated to the north-east (labelled Region A). While the numbers of PMS-only and UMS+PMS classified grid elements are small, this region exhibits the highest concentration of UMS-only classified elements (see Sec. 3.5.2), indicating a comparatively mature population. Another concentration of classified elements is associated with the emission nebula N 138. A more detailed discussion of these individual regions is found in Sec. 3.5.1.2.

Outside these complexes, classified grid elements are fairly scattered; Fig. 3.9 shows 12 isolated elements with signatures of a young population. An inspection of the residuals and significance maps for these isolated elements shows that they are generally consistent with the maps from elements located within star-forming complexes and from the synthetic clusters. A comprehensive analysis of the stellar populations of these isolated elements is beyond the scope of this chapter.

Overall, UMS+PMS classified grid elements are almost exclusively found in groups. PMS-only grid elements, on the other hand, are often located on the outskirts of populous UMS+PMS star groups or appear isolated. To quantify the degree of clustering, we calculated the distance between every possible pair of classified elements. Figure 3.10 (top) shows this distance distribution, together with a distribution for a same-size sample of randomly placed unclassified elements. To eliminate statistical fluctuations, we ran this simulation 100 times and used the mean and standard deviation values to construct the random distribution histogram with corresponding uncertainties. Because of the finite pilot field size, the number of possible random pairs decreases for large distances. For small distances ($< 180 \text{ pc}$), the observed distribution shows a clear excess of classified pairs as a consequence of the clustered distribution of young stars. The broad peak between 450 pc and 700 pc is due to the distances between

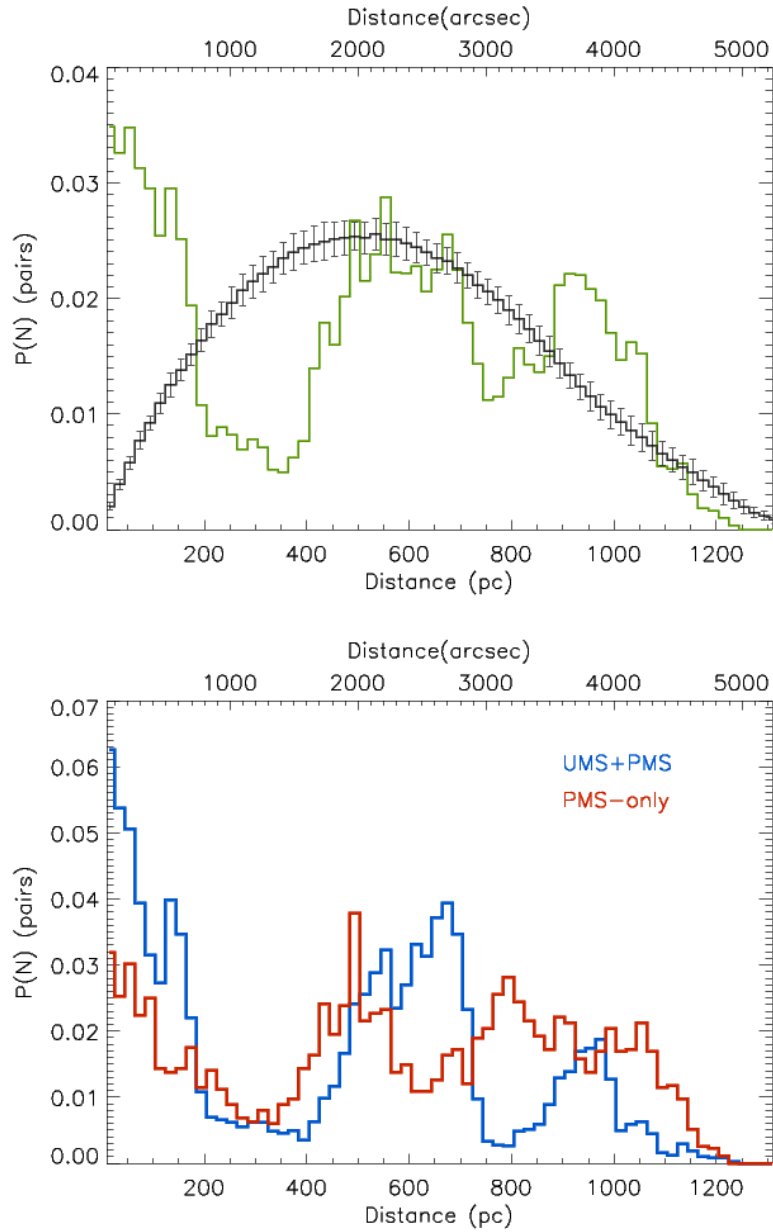


Figure 3.10: **Top:** Normalised distance distribution for all possible grid pairs for the 208 PMS-only and UMS+PMS classified elements (green line), and for a same-size sample of randomly distributed unclassified elements (black line). **Bottom:** Same as the top panel, but separating the two classifications.

N51 and N44, and between N51 and Region A. The peak between 900 pc and 1050 pc is caused by the distances between N44 and N 148, N44 and Region A, and N51 and N 148.

Figure 3.10 (bottom) displays the distance distribution for the PMS-only and UMS+PMS subsamples separately. They are distinct and not simply scaled-down from the overall distribution. As a result of the very strong clustering of the UMS+PMS classified elements, the corresponding distribution shows very prominent peaks. The very narrow peak between ~ 130 pc and ~ 170 pc is due to the distances between associations within N44 and N51. The broad peak for distances $\lesssim 200$ pc suggests a similar distribution of UMS structure sizes, as seen in other star formation complexes in the LMC (Sun et al. 2017b; Sun et al. 2017a) and in the SMC (Sun et al. 2018).

In contrast, the PMS-only distribution shows smaller variations, in agreement with a more extended spatial distribution. It is a common observation in young clusters that high-mass stars are more centrally located than intermediate- and low-mass stars (e.g. Zinnecker et al. 1993; Gennaro et al. 2011; Pang et al. 2013). The underlying physical process is assumed to be dynamical mass segregation (e.g. Bonnell & Davies 1998; Allison et al. 2009). Such effects are relevant within individual clusters, which are usually smaller than one element in our grid. However, since segregation timescales are of the order of several crossing times (e.g. de Grijs et al. 2002), dynamical mass segregation is too slow to explain the observed spatial distribution on the scales of the complexes N 44 and N 51.

In agreement with our results, the HTTP survey found that for the 30 Doradus region, the UMS stars also mostly concentrate in a few main population centres (Sabbi et al. 2016), while the PMS stellar distribution displays a larger spatial dispersion (Cignoni et al. 2015). Based on the distribution of PMS stars and the location of ionised filaments in 30 Doradus, Sabbi et al. (2016) find evidence of constructive feedback from massive stars igniting the birth of new generations of stars. In N 44, Chen et al. (2009) also reported evidence of triggered star formation. Triggering by massive stars could operate on larger spatial scales than mass segregation; it is thus a viable scenario for the different spatial distribution between PMS-only and UMS+PMS elements, since

it could lead to the formation of less massive clusters or associations in the outskirts. This is observed in the Carina Nebula, where the currently ongoing star formation seems to produce only stars up to $\sim 10 M_{\odot}$ (Gaczkowski et al. 2013).

Alternatively, the evaporation of bound clusters due to gas expulsion could also result in the observed spatial distribution of classified elements. After a quick gas removal phase ($\lesssim 1$ Myr), clusters are predicted to expand to half-mass radii $\gtrsim 10$ pc (for masses $\sim 5000 M_{\odot}$) within 10 Myr (Pfalzner et al. 2014). Crucially, they develop an extended stellar halo of ejected stars that can extend beyond 100 pc (Moeckel & Bate 2010). In the comparatively low stellar density environment of such halos, there will naturally be fewer UMS stars, thus increasing the likelihood of PMS-only classified elements in the cluster outskirts.

3.5.1.2 Individual regions

Several regions, associated with a large number of classified elements, are identified in Fig. 3.9. As described before, in N 51 and N 44, the UMS+PMS-classified elements are strongly clustered, whilst the PMS-only elements are often located in the outskirts of these regions. In both complexes significant dust and $H\alpha$ emission is also observed. In N 44, $H\alpha$ emission and the UMS+PMS-classified elements are spatially coincident, as would be expected since the ionising radiation from the UMS stars is the origin of the $H\alpha$ emission. Two large substructures can be seen: the larger substructure near the centre corresponds to the associations LH 47 and LH 48, and the smaller substructure towards the south includes LH 49. To the east of N 51, a similarly strong overlap between $H\alpha$ emission and classified elements is seen. To the west, the intense $H\alpha$ emission traces a bubble-like shape, but the overlap with classified elements is patchy. Two OB associations, LH 51 and LH 54, are associated with this bubble (e.g. Book et al. 2009). A detailed view of these complexes is shown in Fig. 3.11 (top and bottom right panel).

In addition to these complexes, the two most prominent concentrations of classified elements are located in the western part of N 148 and in Region A. N 148 is

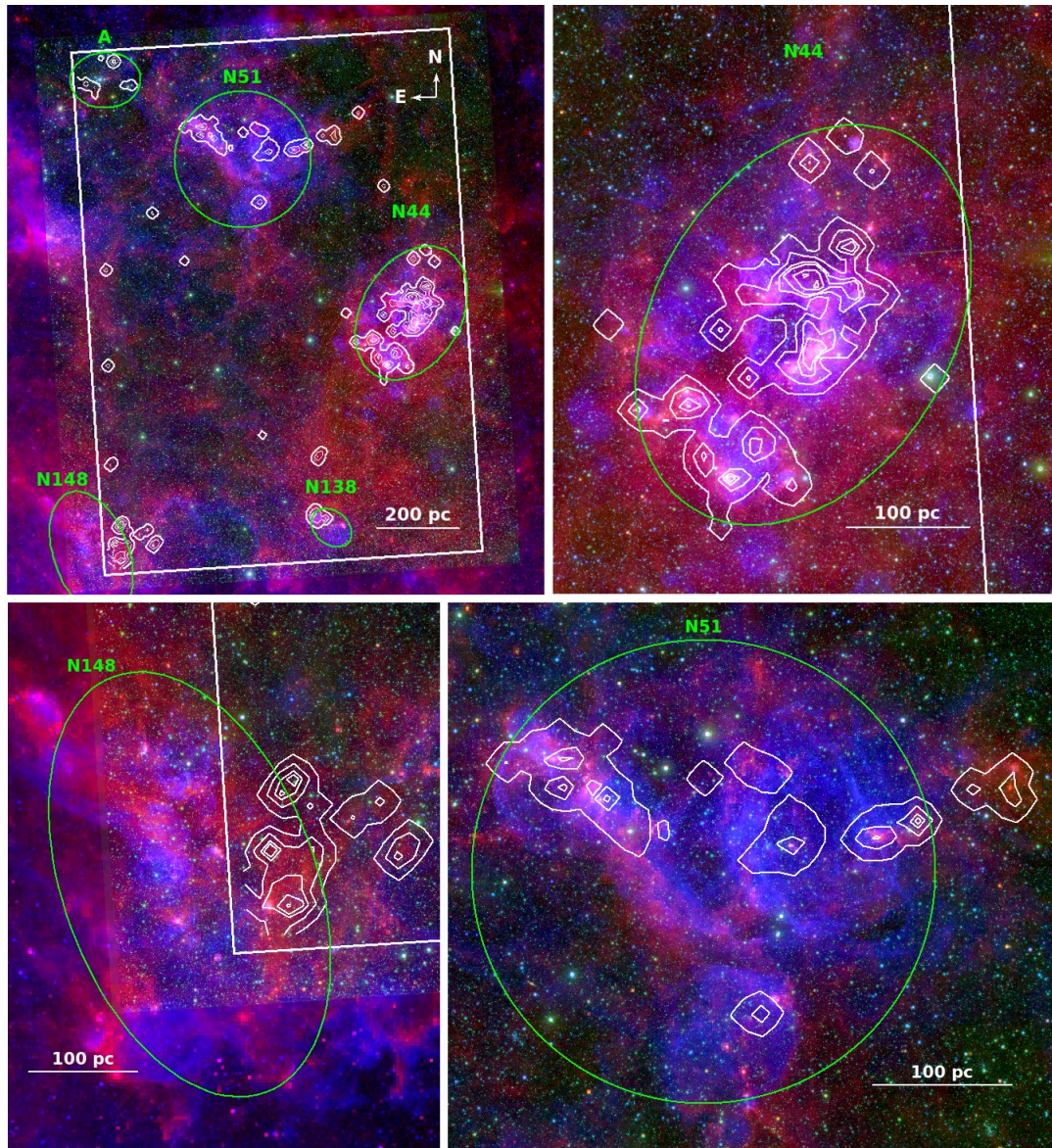


Figure 3.11: Three-colour composite image (top left) of the analysed area with $H\alpha$ emission in blue, K_s ($2.15\ \mu\text{m}$) in green, and *Spitzer* IRAC $8\ \mu\text{m}$ in red. Regions and contours are the same as in Fig. 3.9. Other panels show enlarged views of selected star-forming complexes: N 44 (top right), N 148 (bottom left), and N 51 (bottom right).

an intense and vigorous star-forming region (e.g. Ambrocio-Cruz et al. 2016) and is only partially covered by our analysis. Most grid elements are classified as PMS-only without a significant UMS population; this suggests the existence of a distributed population of intermediate- and low-mass PMS stars associated with N 148, identified here for the first time. Based on comparisons of the significance maps with synthetic clusters, some of the PMS-only grid elements seem very young (~ 1 Myr). The presence of significant dust and CO emission combined with the lack of extended H α emission provides further evidence of a young population devoid of UMS stars. Figure 3.11 shows a zoom into N 148 (bottom left panel).

The classified elements in Region A combine relatively weak PMS signatures with strong UMS signatures, suggesting an older age. The most prominent cluster in this area, NGC 2004, indeed has an age of ~ 20 Myr (Niederhofer et al. 2015), resulting in a PMS population that is too faint to be reliably detected with the VMC data. Region A also lies in an area with no significant dust or H α emission. This all hints at a comparatively old age of the dominant populations in the region, probably a result of the energetic feedback from massive stars that have significantly eroded the interstellar medium.

Another grouping of classified elements is found to the north-east of the emission nebula N 138. More specifically, the PMS-only and UMS+PMS-classified regions are spatially coincident with the H II regions N 138A and N 138C. In N 138A Indebetouw, Johnson & Conti (2004) found an ultracompact H II source, indicative of very young massive stars.

Our method for classifying young populations not only identifies all major star-forming complexes in tile LMC 7.5, but also exposes their full extents and distribution for the first time.

3.5.2 Spatial distribution of the older UMS population

In Sec. 3.5.1 we analysed the spatial distribution of elements showing a PMS signature. We found especially pronounced clustering for UMS+PMS-classified grid elements,

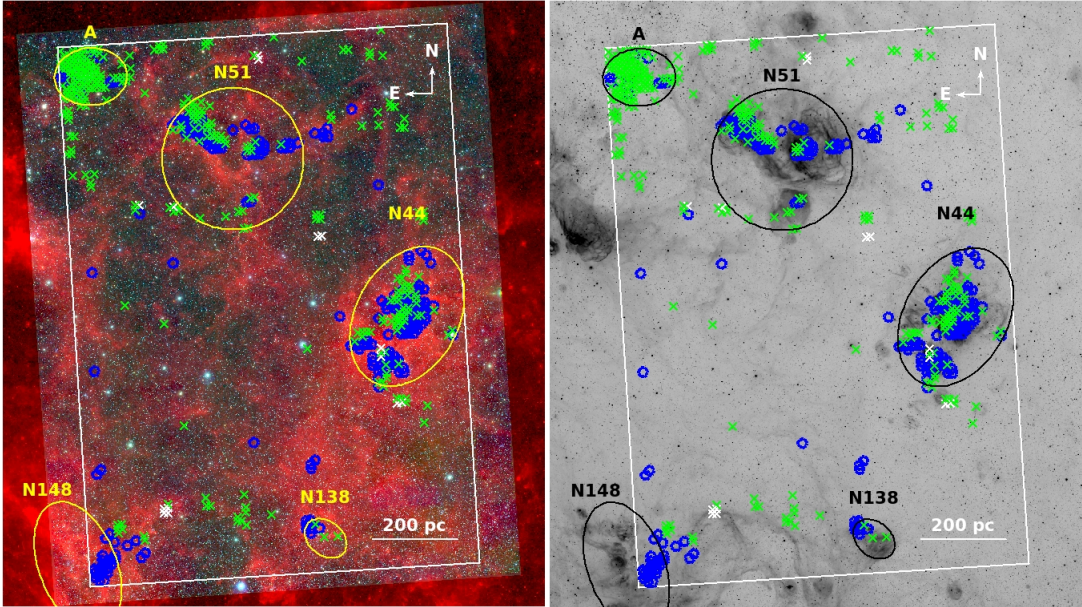


Figure 3.12: **Left:** Three-colour composite image with VMC Y (blue) and K_s bands (green), and *Spitzer* IRAC $8.0\ \mu\text{m}$ (see also Fig. 3.9). Green and white crosses mark the locations of elements classified as UMS and “old”, respectively. The UMS+PMS and PMS-only classified elements are included as blue circles to facilitate comparison. **Right:** Same as the left panel, but using an inverted grey-scale image of the $H\alpha$ emission.

which represent young and relatively massive populations. Here we investigate the spatial distribution of the 298 grid elements classified as UMS-only. They contain comparatively old populations (10 – 300 Myr; see Sec. 3.3).

Figure 3.12 shows the location of the grid elements classified as UMS-only and “old”. Their spatial distribution is more scattered across the pilot field than the UMS+PMS elements. Consequently, more UMS-only elements are either isolated or located in small groups outside the known complexes. The concentration of UMS-only elements in region A is noticeable and is further confirmation of the comparatively older age of this population. The 14 grid elements classified as “old” are scattered across the field and are neither co-spatial with young grid elements, nor with any significant dust or $H\alpha$ emission. Twelve of them seem associated with known LMC clusters (Bica

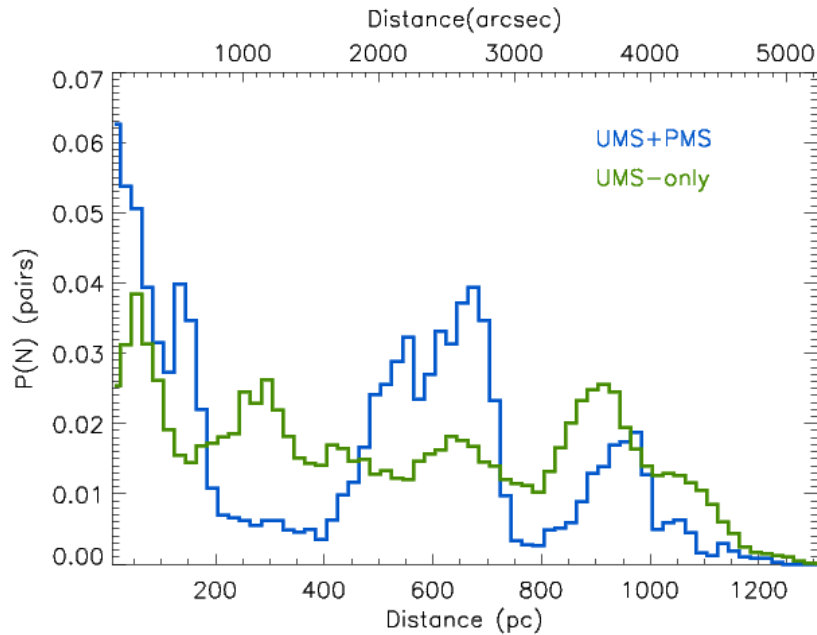


Figure 3.13: Normalised distance distribution for all possible grid element pairs classified as UMS+PMS (blue) and UMS-only (green) (see also Fig 3.10).

et al. 2008).

Fig. 3.13 is equivalent to Fig. 3.10 (bottom), but shows the distance distributions for all possible pairs of UMS+PMS and UMS-only classified elements. Some clustering is present for UMS-only elements, but it is much less pronounced than that for the UMS+PMS classified elements; UMS-only elements show a comparatively smooth distribution. This is in agreement with the temporal evolution of young stellar structures, which are observed to disperse on timescales of ~ 100 Myr (e.g. Sun et al. 2017a).

3.5.3 Quantitative analysis of the PMS populations

Using the residual maps, we calculate the number density of PMS candidates as well as the overall number of PMS candidates in the classified elements. Taking the mean density excess of the flagged boxes relevant for PMS populations (see Fig. 3.6) and

Table 3.3: Number of PMS candidates in the whole LMC 7.5 tile and individual prominent regions. The errors are calculated assuming grid elements are statistically independent.

	N_{PMS}
LMC 7.5	2256 ± 54
N 44	1000 ± 38
N 51	379 ± 22
N 148	238 ± 20
A	112 ± 13
N 138	74 ± 9

multiplying it by the area covered by these boxes in the CMD, we derive the PMS number density. We obtain a mean PMS number density $n_{\text{PMS}} = 12.7 \text{ stars arcmin}^{-2}$ over all elements classified as PMS-only or UMS+PMS. The uncertainty, estimated by analysing the density fluctuations in the residuals of non-classified elements, is $\Delta n_{\text{PMS}} = 2.4 \text{ stars arcmin}^{-2}$. Multiplying the PMS density by the solid angle of the grid element ($\sim 1.4 \text{ arcmin}^2$), we derive the number of PMS candidates (N_{PMS}). On average, there are $N_{\text{PMS}} = 17.7 \pm 3.4$ per classified element.

In Fig. 3.9 we plot the PMS density contours. The highest density is found within N 44 ($40 \text{ stars arcmin}^{-2} \cong 0.18 \text{ stars pc}^{-2}$). Large complexes contain multiple high-density peaks, displaying a hierarchical structure similar to that found for UMS stars (Sun et al. 2017a; Sun et al. 2017b). Integrating over all classified elements and accounting for the overlap between neighbouring grid elements, we determine a total number of PMS candidates of 2256 ± 54 . This result is a lower limit because the incompleteness in the VMC data at magnitudes typical of PMS stars is significant.

Table 3.3 lists the number of PMS candidates for the whole pilot field as well as for the five regions described in the previous sections. Overall, $\sim 80\%$ of all PMS candidates identified are located in one of these regions, with N 44 being the most populous.

For comparison, Meingast et al. (2016) estimated the entire young stellar pop-

ulation of the Orion A molecular cloud to have between 2300 and 3000 stars. Using a Kroupa IMF, this gives 300 to 390 stars with masses $1 M_{\odot} \leq M_* \leq 4 M_{\odot}$, which is the PMS mass range our method is sensitive to (see Fig. 3.6). The area covered by the Orion survey (18.3 deg^2) corresponds to 4.5 arcmin^2 or 3.2 grid elements at the LMC distance. In the Carina Nebula complex, 8781 young stars were identified based on their NIR colour excess (Zeidler et al. 2016). Applying a Kroupa IMF to the same mass range gives ~ 1150 stars that could potentially be identified as PMS with our method. This is comparable with our PMS count for the N 44 complex. We note, however, that this estimate includes only sources with an NIR colour excess. At the LMC distance, the area observed in Zeidler et al. (2016) corresponds to 51.5 arcmin^2 or around 37 grid elements, which is approximately the area covered by the large group of classified elements in the centre of N 44. Incompleteness and crowding would obviously reduce the number of PMS sources we would be able to detect.

To obtain a more detailed view of the morphology of the PMS populations, we define PMS structures as regions enclosed by the lowest density contour in Fig. 3.9. We detect 31 structures in total, the most populous of which is located in N 44 and contains ~ 670 PMS candidates. Figure 3.14 shows the cumulative N_{PMS} distribution for the PMS structures.

For $N_{\text{PMS}} > 20$ the distribution can be approximated by a power law with a slope $\alpha(N_{\text{PMS}}) = -0.86 \pm 0.12$. Studies of cluster mass distributions have shown that high-mass clusters are less numerous than low-mass ones (e.g. Zhang & Fall 1999; Hunter et al. 2003; de Grijs & Goodwin 2008), with a slope $\alpha(M) \sim -1$. In a histogram using equal $\log M$ intervals, $\alpha(M) = -1$ is equivalent to a mass distribution function $n(M)dm \propto M^{-\beta}dm$ with $\beta = -2$, which is the slope expected for a scale-free hierarchical star formation scenario governed by turbulence (e.g. Fleck 1996; Elmegreen 2008). Converting N_{PMS} obtained from our method into structure masses would yield very uncertain estimates because of the significant age dependence of the sensitivity limit of our VMC-based method (see Sec. 3.4.1). For predominantly “old” PMS populations, $\alpha(M) > \alpha(N_{\text{PMS}})$ is expected, since a large fraction of PMS structures will have low PMS counts; for predominantly young PMS populations, we could expect

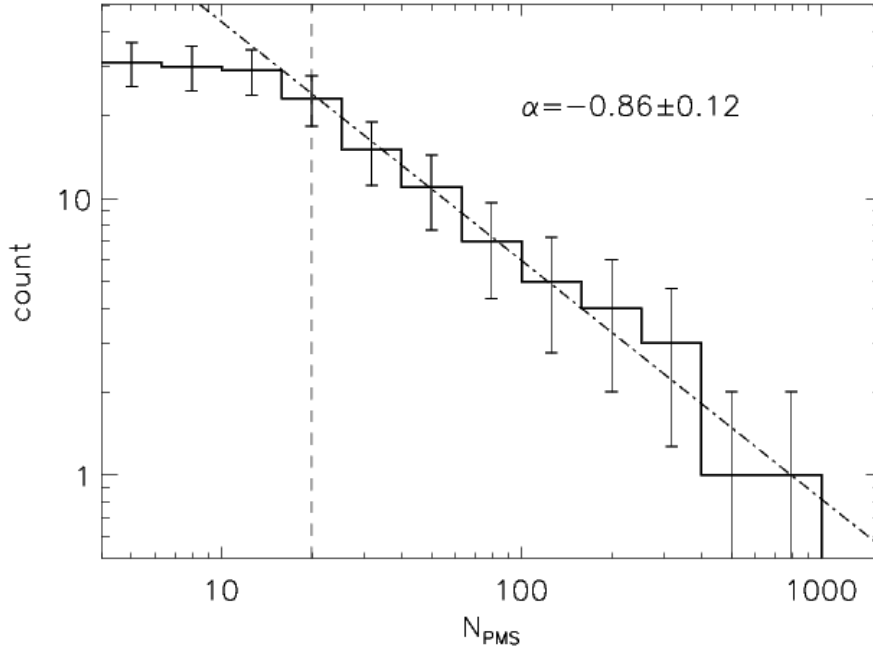


Figure 3.14: Cumulative number distribution for the 31 PMS structures (0.2 dex bins). The vertical dashed line indicates the sensitivity limit, while the dash-dotted line represents a power law with a slope of -0.86 . The error bars represent the Poissonian uncertainties.

$\alpha(M) < \alpha(N_{\text{PMS}})$. A more thorough discussion of the mass distribution should take the ages of the populations into account.

3.5.4 Comparison with dust emission maps

Since dust emission should be proportional to the product of dust mass and input stellar radiation (because of the energy balance between absorption and emission), one would expect a strong correlation between the number of young stars and dust emission. Bright far-infrared (FIR) emission is usually associated with high star formation rates (see Casey, Narayanan & Cooray 2014 for a comprehensive overview); it originates from the radiation of the young stars that is processed by dust from the remnants of their

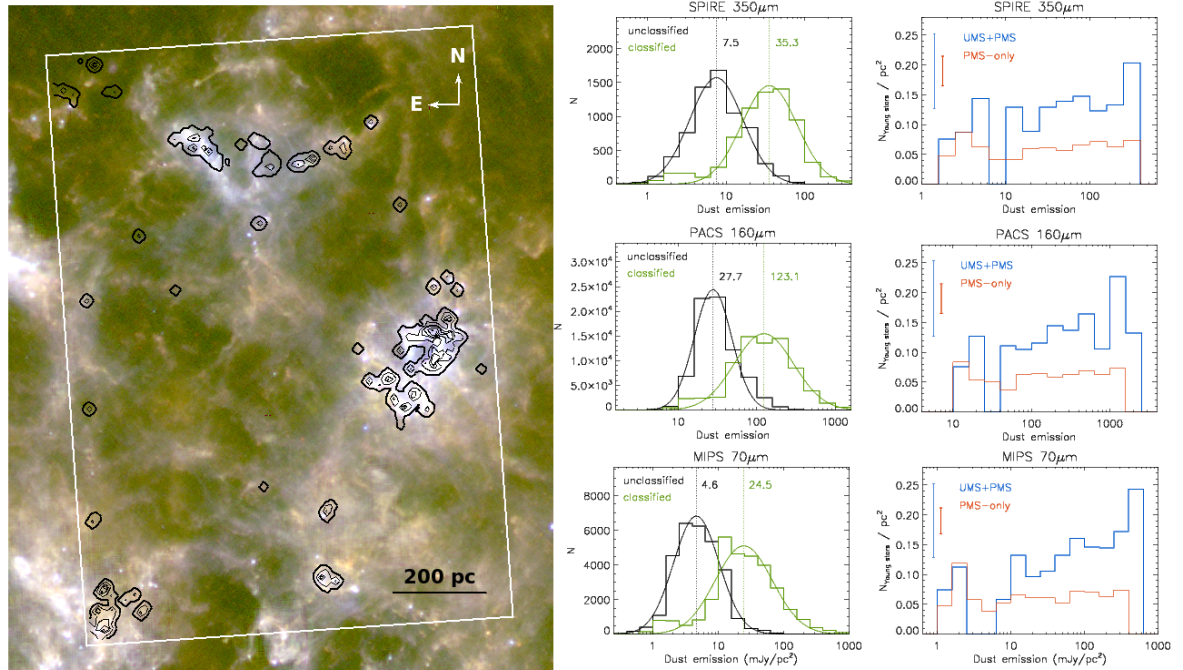


Figure 3.15: **Left panel:** Three-colour composite image with *Spitzer* MIPS 70 μm in blue, *Herschel* PACS 160 μm in green, and *Herschel* SPIRE 350 μm in red; the density contours are the same as those in Fig. 3.9. **Middle panels:** Dust emission distribution for image pixels in areas covered by the UMS+PMS and PMS-only classified elements, and by the same number of randomly selected unclassified elements. A Gaussian fit is plotted and the mean of the fit is indicated. **Right panels:** Mean dust emission vs. young stars number density for the PMS and UMS+PMS classified elements. The error bars show the typical standard deviations within the dust emission bins.

natal molecular clouds and re-emitted at longer wavelengths. Skibba et al. (2012) have reported that some regions with bright dust emission in the MCs coincide with known star-forming regions. Moreover, in M33 only young structures (< 100 Myr) were found to correlate with FIR surface brightness (Javadi et al. 2017). Given that the presence of PMS stars is an indicator of recent star formation, we examined the relation with FIR emission in regions covered by the UMS+PMS and PMS-only classified elements.

We made use of data from the SAGE and HERITAGE surveys in six FIR bands ranging from 70 to 500 μm (Meixner et al. 2006; Meixner et al. 2013). Figure 3.15 (left)

shows the PMS density contours overplotted onto an RGB image (70, 160 and 350 μm) of the pilot field. PMS-only and UMS+PMS-classified elements are located along ridges and filamentary structures with bright dust emission. The only significant exceptions are Region A and some isolated PMS-only elements. As mentioned previously, the weak dust emission for Region A is in agreement with the inferred comparatively old age of the stellar populations.

The concentration of elements with PMS populations in regions with bright dust emission is explicitly shown in the middle histograms of Fig. 3.15. The dust emission distributions for grid elements associated with PMS populations and a randomly selected sample of unclassified elements are clearly distinct; in particular, the strongest observed emission is always associated with young stellar populations.

Figure 3.15 (right) shows the dust emission versus the average number density of young stars for the same three FIR bands, separating PMS-only and UMS+PMS-classified grid elements. We computed UMS densities for the UMS+PMS elements similarly to the PMS densities (Sec. 3.5.3) to obtain the total density of young stars. We calculated the mean FIR emission for every classified element and grouped them in 0.2 dex bins; for every bin, the average number density of young stars was determined. For the UMS+PMS elements, we observe a relatively weak but consistent trend towards higher stellar number densities with increasing dust emission for all wavelengths. Hony et al. (2015) found a positive correlation between the number density of young stars (UMS and PMS stars identified using HST photometry; Gouliermis et al. 2006) and dust surface density in the prominent star-forming complex NGC 346 in the SMC. Their analysis, on scales comparable to the size of our grid elements, is in agreement with the trend in Figure 3.15 (right). For PMS-only elements, however, we do not observe an increase in stellar density with dust emission; less clustered low- and intermediate-mass PMS populations are likely more affected by the limitations of the VMC data.

Depending on the wavelength, the emission associated with the UMS+PMS and PMS-only classified elements is between four and eight times brighter than the field average (Fig. 3.16); the strongest enhancement is found for the shorter wavelengths. Furthermore, the ratios for the PMS-only sample (red) are essentially independent of

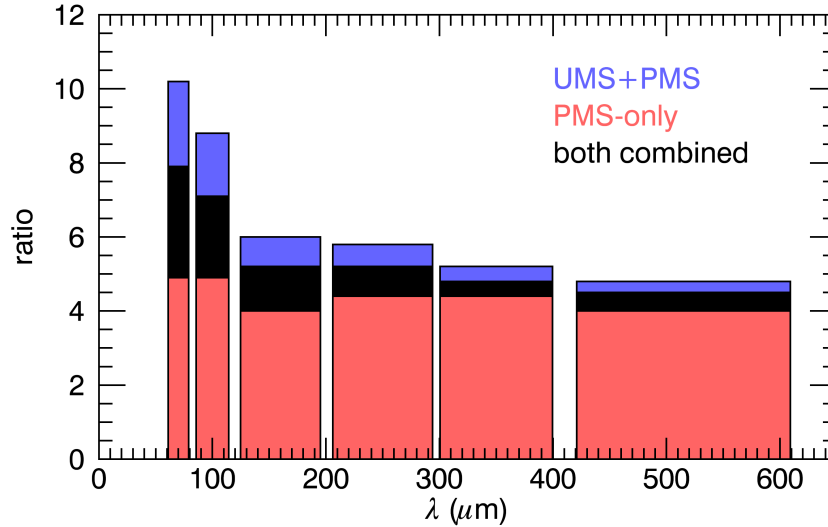


Figure 3.16: Ratios of the mean dust emission observed for classified elements and the field average. The widths of the bars mimic the filter bandwidths.

the wavelength, while the ratio for the UMS+PMS sample (blue) increases significantly towards shorter wavelengths. This is evidence that the dust is heated primarily by the young massive UMS stars, while the PMS populations contribute very little. This is consistent with studies that found that warm dust follows the distribution of massive stars in the LMC (Bernard et al. 2008), as well as in Galactic star-forming complexes (Preibisch et al. 2012; Roccatagliata et al. 2013). As a comparison, for the UMS-only classified elements (not shown), the dust emission is between 1.3 and 1.8 times higher than the pilot field average. The analysis in this section confirms the important role that young UMS stars play in heating the dust.

3.6 Summary and conclusions

We presented a method for identifying PMS populations ($\geq 1 M_{\odot}$) using data from the VMC survey. The method applies a Hess diagram analysis in the $K_s/(Y - K_s)$

space, including corrections for reddening and completeness, to distinguish young stellar populations from the underlying field; this analysis is performed independently on individual fixed-size spatial grid elements. Young populations are identified as density excesses (with respect to the field population) in pre-defined regions of the differential Hess diagrams. Depending on the location of these density excesses with respect to theoretical expectations (i.e. isochrones), we classify the population within a grid element into one of the four classes: PMS-only (population of young low-mass stars), UMS+PMS (young population with well-sampled IMF across the mass range), UMS-only (predominantly older population dominated by a prominent main-sequence population), and “old” (population that displays a significant contribution from evolved stars, in particular populating the red giant branch).

We applied our method to a $\sim 1.5 \text{ deg}^2$ VMC pilot field (LMC 7.5, located to the North of the LMC bar) and summarise our findings below.

- Tests with synthetic clusters explore the sensitivity of the method in the age range 1 Myr – 1 Gyr and the mass range $250 M_{\odot} - 3000 M_{\odot}$. We find that PMS populations can be identified up to an age of ~ 10 Myr for cluster masses $> 1000 M_{\odot}$. Beyond 10 Myr, any remaining PMS populations are below the VMC sensitivity limit. The sensitivity increases towards younger ages: PMS populations with ages ≤ 2 Myr can be detected for clusters with masses down to $250 M_{\odot}$.
- We detected a total number of 2256 ± 54 PMS stars in the pilot field. The most populous region is the N 44 complex, which has 1000 ± 38 PMS stars. This estimate must be taken as a lower limit because the VMC data are incomplete and our method has a sensitivity limit.
- The spatial distribution of elements with PMS populations is clearly inhomogeneous and clustered. UMS+PMS elements are almost exclusively found in large groups, while the PMS-only elements are more dispersed and often located in the outskirts of large star-forming complexes.

- Large star-forming complexes consist of multiple high stellar density peaks, with the highest densities found in the N 44 complex. Overall, we detect 31 PMS structures whose number distribution can be approximated by a power law with a slope of -0.86 ± 0.12 . A mass distribution with this slope would be broadly consistent with a hierarchical star formation scenario governed by turbulence.
- The PMS populations are mostly located along ridges with intense dust emission in the FIR ($70 - 500 \mu\text{m}$). We observe a correlation between the dust emission and the number of young stars for the UMS+PMS elements. This is not the case for the PMS-only elements that lack UMS stars. Dust emission is around four to eight times brighter for the UMS+PMS elements than in quiescent regions; at the shortest wavelengths, the emission can be as much as ten times brighter. This is likely due to dust heating by the radiation from the young UMS stars.
- Our analysis recovers all known star formation complexes in this field, and for the first time reveals their true spatial extent.
- In the south-eastern corner of LMC 7.5, we discovered a significant intermediate- and low-mass PMS population that is likely associated with the wider N 148 star-forming complex. Comparison with synthetic cluster Hess CMDs suggests a very young age (~ 1 Myr) for this population. This population is co-spatial with significant CO emission.

Our method clearly shows the potential of the VMC survey to identify and characterise intermediate- and low-mass young stellar populations on the scale of the whole Magellanic system. We are working on applying our method to other LMC and SMC VMC tiles.

4 Variability analysis of Young Stellar Objects

The work presented in this Chapter will also be published in Zivkov et al., in prep.

4.1 Introduction

Variability patterns in young stars can be associated with different mechanisms such as rotational modulation of hot and cool star spots, obscuration events by disc structures like warps or clumps, and unsteady mass accretion (see Sec. 1.2). Metallicity appears to have an influence on accretion rate and duration of accretion episodes, as well as on disc lifetimes and possibly disc masses (Sec. 1.3.2). Hence, it is reasonable to investigate possible metallicity dependence on global variability characteristics of young stellar populations.

Vijh et al. (2009) examined the variability of LMC stars using SAGE data (Sec. 1.4.1). They found ~ 2000 variables which were mostly evolved AGB stars. Cross-correlating these variables with the list of ~ 1000 YSOs from Whitney et al. (2008) revealed that 29 variables are likely YSOs, resulting in a YSO-variability fraction of around 3%. However, with only two epochs available in the SAGE catalogues it is not possible to constrain amplitudes and periods. The SAGE-var study (Riebel et al. 2015) added 4 observational epochs to the SAGE and SAGE-SMC data, for a total of six epochs. Using the same criteria as Vijh et al. (2009), the SAGE-var data led to the identification of 2198 variables in the LMC, out of which only 12 are YSO candidates. These low numbers either indicate a very low sensitivity towards young variables or simply a low variability fraction amongst young stars.

We use the VMC data combined with observations from our open time programme (Sec. 2.3.1) to examine the variability of a sample of highly reliable YSOs. Overall, 25 epochs in the K_s -band and 14 epochs in the J -band are available to investigate the lightcurves in a wavelength regime where numerous Galactic studies have

found significant variability fractions amongst young stars (see Sec. 1.2). This chapter is organized as follows: Section 4.2 explains how the multi-epoch catalogue is constructed. We proceed in Sec. 4.3 with the identification criteria for photometric variability. The reliability of the variability identification is then examined in Sec. 4.4 by testing how well known samples of evolved variable stars are recovered. Also examined is our ability to detect periodicity. This is followed by a detailed explanation in Sec. 4.5 of the selection and decontamination process of the YSO sample. We present and discuss the results of the YSO-variability analysis in Sec. 4.6, and finish with a summary in Sec. 4.7.

4.2 Multi-epoch catalogue

4.2.1 Constructing the multi-epoch catalogue

We start with the photometric catalogue obtained by performing PSF photometry on deep tile images where individual pawprints from all VMC-epochs were homogenised (Sec. 2.3). It is the deepest catalogue available and reaches 50 % completeness limits of $J \approx 21.3$ mag and $K_s \approx 20.6$ mag. All individual pawprint catalogues are cross-matched to the deep catalogue – where every source has a source ID – using a matching radius of $0.5''$. The matched sources from the pawprint catalogues are assigned the source ID of the respective deep counterpart, which is used to identify a source throughout the epochs.

Overall, $\sim 13\%$ (J) and $\sim 6\%$ (K_s) of the sources in the pawprint catalogues do not have a deep catalogue counterpart. The comparatively high fraction of unmatched J sources is likely due to the small number of VMC-epochs in this band; as a consequence, the deep catalogue is not that much deeper than the individual pawprint catalogues in J . Independent of the filter, we found that the unmatched sources are sometimes concentrated at the detector edges. Figure 4.1 shows for a typical detector and pawprint the spatial distribution of sources with and without deep counterpart;

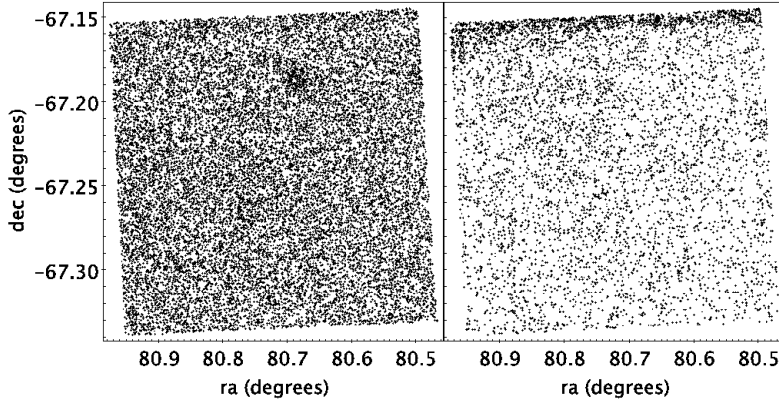


Figure 4.1: Spatial distribution of all sources from detector 4 and pawprint Epoch 4-J6 with counterpart (left panel), and without counterpart (right panel) in the deep catalogue.

the unmatched sources show a severe density enhancement along the northern detector edge. Since we only keep the matched sources, our cross-matching with the deep catalogue also removes spurious detections in the individual pawprint catalogues.

For the variability analysis, we further exclude all sources in the pawprint catalogues with $K_s < 12.6$ mag and $J < 13$ mag. This is to avoid saturation and non-linearity effects which increase the photometric scatter at bright magnitudes substantially. These limits are also generous enough to account for differences in the saturation level between the VIRCAM detectors.

4.2.2 Correcting magnitude offsets

The sensitivity of the VISTA-detectors is not perfectly stable, they show variations over long timescales (González-Fernández et al. 2018). We corrected for any systematic magnitude offsets for all pawprints and detectors by using the following procedure. For every individual pawprint and detector the sources with a counterpart in the deep catalogue are selected. This results typically in a sample of 5 000 - 10 000 sources. From this sample we calculate the mean magnitude according to the pawprint catalogue

$\langle m_{\text{pp}} \rangle$ and the mean magnitude according to the deep catalogue $\langle m_{\text{deep}} \rangle$. Next, the difference between these two ($\langle m_{\text{pp}} \rangle - \langle m_{\text{deep}} \rangle$) is subtracted from the magnitudes of the sample in the pawprint catalogue. The differences are generally small, $\sim 99\%$ of them are within ± 0.02 and ± 0.04 mag for the J and K_s -band, respectively. Figure 4.2 shows for all pawprints and bands the fluxbased mean of the corrected magnitudes over all epochs versus the mean of the associated photometric errors (as provided by the PSF pawprint catalogues).

4.3 Identifying variable stars using χ^2 -analysis

Different methods are available to identify variables in multi-epoch data. One of them is the χ^2 -analysis, which calculates the variance of a series of measurements in a given band and relates it to the estimated photometric error. For a set of N measurements it is given by

$$\chi^2 = \frac{1}{N-1} \sum_{i=1}^N \frac{(\text{mag}_i - \overline{\text{mag}})^2}{\sigma_i^2}, \quad (4.1)$$

where σ_i and mag_i are the photometric error and the magnitude of the i -th measurement, respectively, while $\overline{\text{mag}}$ is the mean magnitude. We considered using the Stetson index (Stetson 1996), which identifies correlated variability between two or more bands by using contemporaneous multi-epoch observations. However, only two VMC-epochs are observed back-to-back in J and K_s . As a consequence, only two of the 13 K_s -epochs observed in 2012 - 2017 could have been utilised to compute the Stetson index. Hence, we focused on the χ^2 -analysis for this work.

Given that sources can be detected in up to six pawprints per epoch, three reasonable options are available for how to calculate the χ^2 -values.

1. Epoch magnitudes and photometric errors are derived from the pawprint photometry by taking the fluxbased mean, and then used as input for Eq. 4.1.
2. Every pawprint is viewed as an epoch. Consequently, the magnitudes and

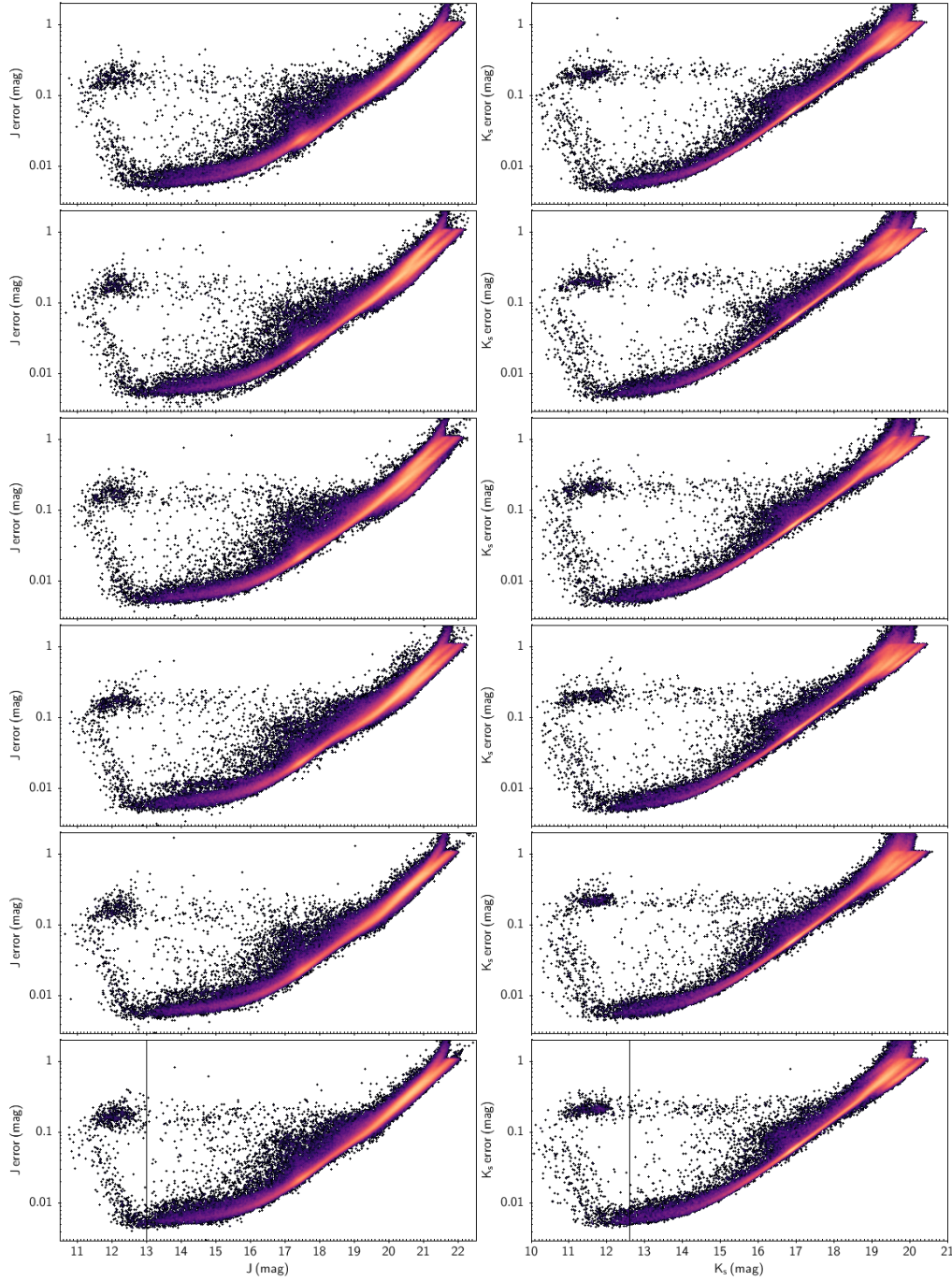


Figure 4.2: Fluxbased mean magnitudes versus mean photometric errors for the J -band (left panels) and the K_s -band (right panels) for Pawprint 1 to 6 (top to bottom row) over all epochs. The vertical lines in the bottom panels indicate the bright magnitude cutoff (Sec. 4.2.1).

photometric errors, as given in the pawprint catalogues, are used to calculate the χ^2 -value.

3. Pawprint magnitudes and photometric errors are used, but each pawprint is analysed separately (e.g. Epoch 1-K1, Epoch 2-K1, Epoch 3-K1, ...). Hence, a χ^2 -distribution is obtained for each pawprint.

The last option will result in two or more χ^2 -values for most sources, as most areas of a VISTA-tile are covered by at least two pawprints. This approach has the advantage of avoiding any complications due to differences between the detectors, since the mag_i values are taken from observations where a given source is always seen on the same detector.

In general, the distribution of χ^2 -values for a large random sample of stars exhibits a narrow peak, populated by non-variable objects which are the majority of the sources. If the photometric error is correctly estimated the peak will be located at $\chi^2 \approx 1$. Stars with luminosity fluctuations exceeding the photometric error create a tail towards high χ^2 -values. If such a star is above a chosen χ^2 -threshold, it is taken to be variable. As the large majority of stars are non-variable, only a small fraction is expected to populate the high χ^2 -value tail. Finding an appropriate threshold for a given catalogue is crucial for the reliable identification of variable stars. The appropriate thresholds may vary between the pawprints, precluding the use of one single threshold for all datasets. This is an additional advantage of option three above, which avoids differences between the pawprints by calculating the χ^2 -distributions individually for the six pawprints.

In Fig. 4.3 and 4.4 we compare the mean photometric error with the standard deviation for each light curve in the K_s and J -band, respectively (the six pawprints are plotted separately to visualise possible differences between them). The distribution is expected to follow a 1:1 relationship indicated by the diagonal green line, in which case the photometric errors correctly represent the observed fluctuations. There is an offset with respect to the 1:1 relation for the K_s -band, which indicates an overestimation of the photometric error in the PSF photometry catalogues. It causes a shift in the peak of the K_s -band χ^2 -histogram away from unity (see distributions in Fig. 4.5). This offset

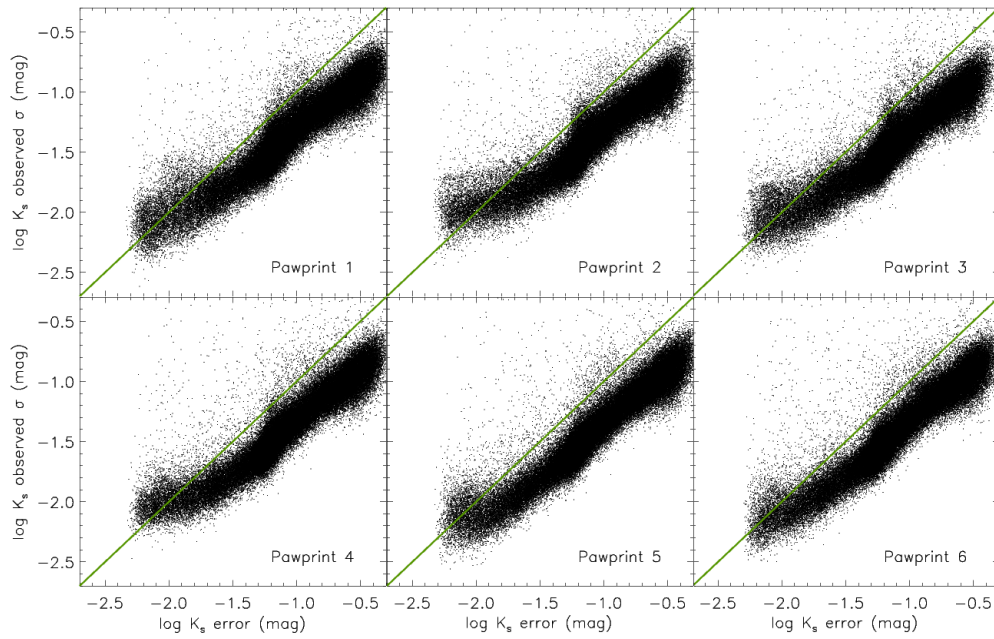


Figure 4.3: Comparison between the mean photometric errors and the observed standard deviation of the K_s -magnitudes. Every plotted source was detected at least 10 times to reduce the number of outliers caused by small number statistics. The green line shows the 1:1 relation.

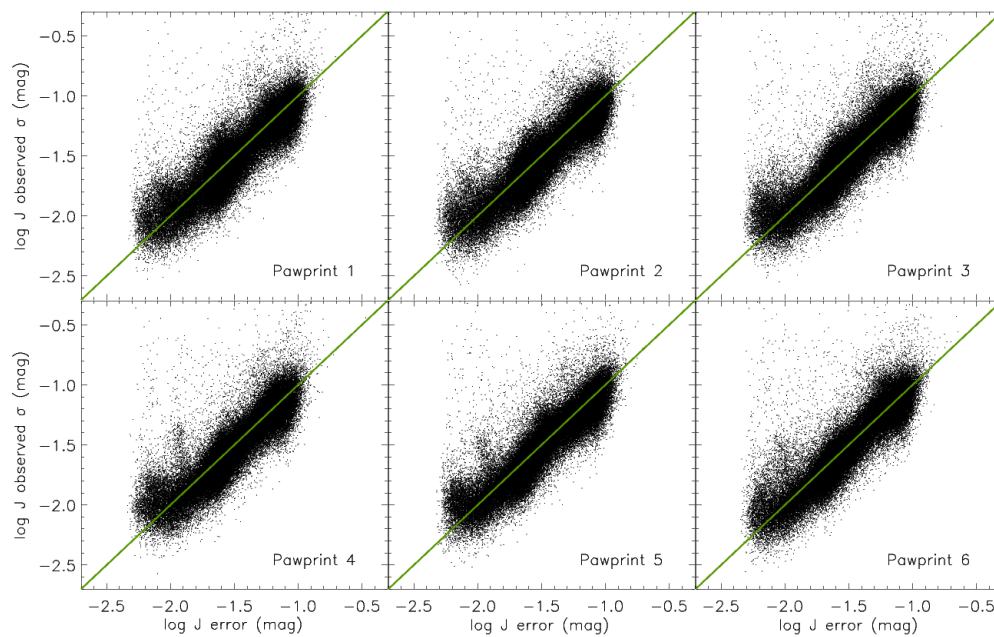


Figure 4.4: Same as Fig. 4.3, but for the J -band.

is not observed in the equivalent J -band plots, i.e. the estimated photometric error in the J -band correctly represent the photometric uncertainty.

The K_s -band distributions seem to approach a plateau (or noise-floor) at small photometric errors, i.e. for bright stars. A plateauing was also observed in Rebull et al. (2014), however they did not have a systematic offset as in our K_s -data. The differences between the pawprints are most pronounced in this plateau regime. The noise floor in Pawprint 4 is ≈ 0.01 mag, but for instance in Pawprint 6 there does not seem to be a noise-floor. In the K_s -band this noise-floor sets in for sources with a $K_s \lesssim 15.5$ mag. As a consequence either some correction has to be applied before calculating the χ^2 -values, or the sample of bright stars has to be treated separately. For the J -band this behaviour is less pronounced, but it is observed for sources with $J \lesssim 15.3$ mag.

As a consequence of the previous discussion we investigate separately the χ^2 -distribution of bright sources with mean magnitudes of $K_s < 15.5$ mag and $J < 15.3$ mag. This gives 6×2 distributions per filter (two magnitude ranges for every pawprint) with their corresponding thresholds for both the bright and faint samples, respectively. Table 4.1 lists all different cases with their thresholds. They are determined by approximating the $\log(\chi^2)$ -distributions with a Gaussian function and taking its 3σ value towards the high value tail. Note that the thresholds for the bright sample vary much more between pawprints than their counterparts calculated for the fainter sample. This reflects the comparatively large pawprint differences seen in the regime where the distributions approach or reach a noise floor (Fig. 4.3 and 4.4). Figures 4.5 and 4.6 show all $\log(\chi^2)$ -distributions with their associated Gaussian approximations. The distributions peak at ~ 1 for the faint sources in the J -band. It is apparent that the peaks of the distributions for the K_s -band are shifted to lower values compared to the J -band. This is a consequence of the overestimation of the K_s photometric error (Fig. 4.3). For the bright sources the peaks are broader and generally shifted towards higher values for both filters. This is due to the flattening of the σ and mean photometric error distribution shown in Fig. 4.3 and 4.4.

To contribute to the χ^2 -distribution calculation, we require that a source is de-

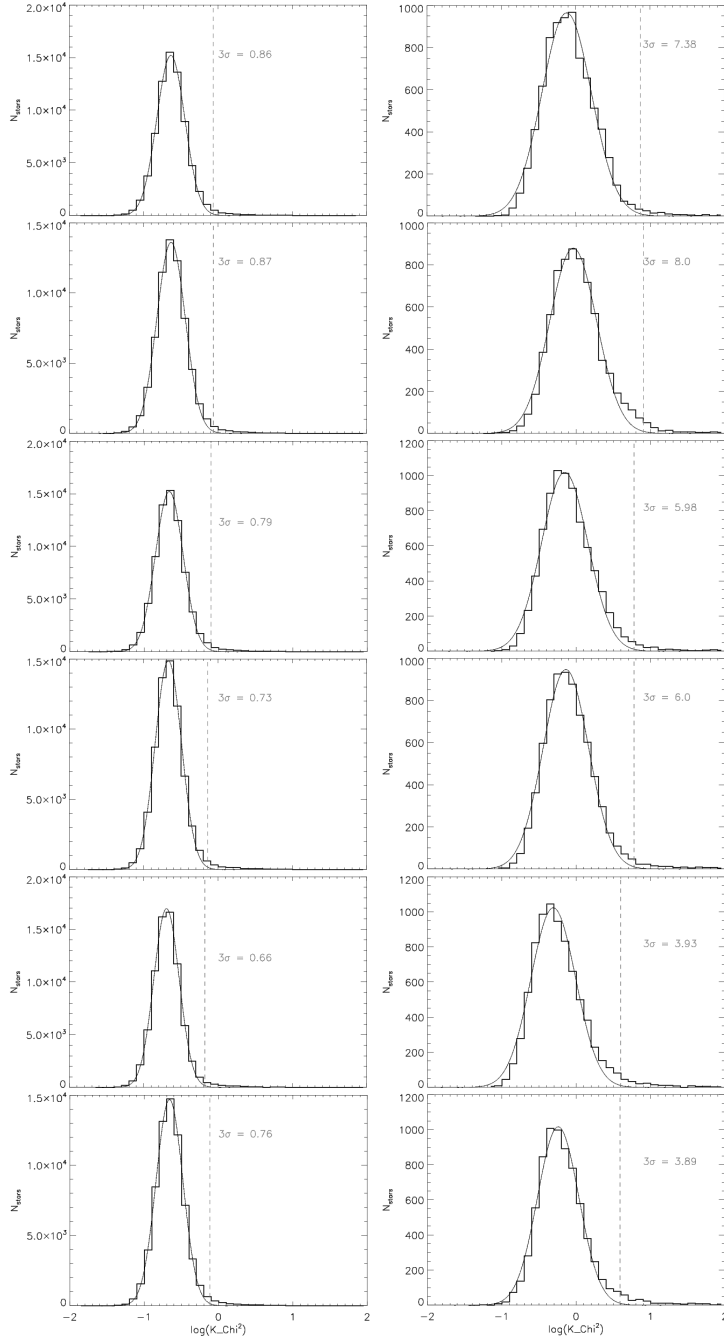


Figure 4.5: χ^2 -distributions for K_s -band photometric data for Pawprint 1 to 6 (top to bottom row): left panels for the faint sample ($K_s \geq 15.5$ mag), right panels for the bright sample. The dashed lines indicate the 3σ thresholds.

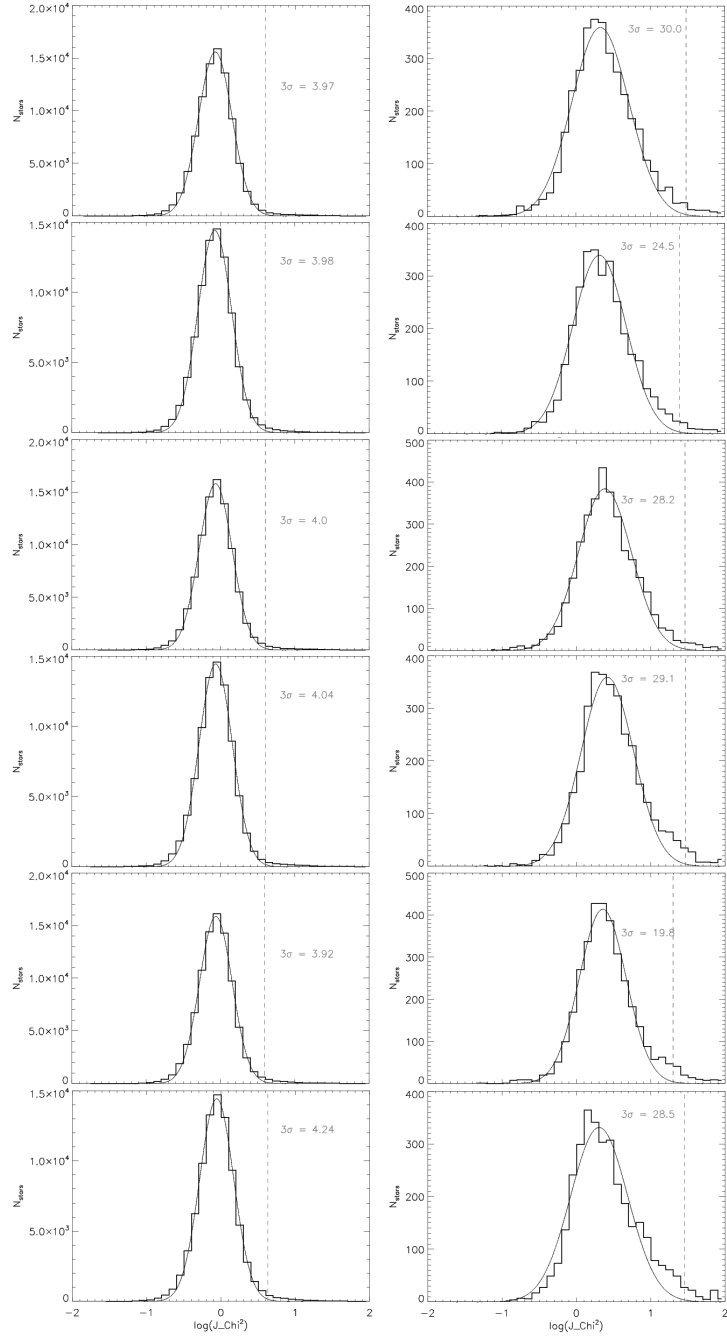


Figure 4.6: As Fig. 4.5, but for J -band photometry.

Table 4.1: χ^2 -thresholds for the different pawprints, filters, and magnitude ranges (Bright sample: $J < 15.3$ mag and $K_s < 15.5$ mag; Faint sample: $J \geq 15.3$ mag and $K_s \geq 15.5$ mag).

Pawprint	Filter	Bright sample	Faint sample
1	J	30.0	3.97
2	J	24.5	3.98
3	J	28.2	4.00
4	J	29.1	4.04
5	J	19.8	3.92
6	J	28.5	4.24
1	K_s	7.38	0.86
2	K_s	8.00	0.87
3	K_s	5.98	0.79
4	K_s	6.00	0.73
5	K_s	3.93	0.66
6	K_s	3.78	0.76

tected in at least ten K_s epochs, and in six J epochs. These requirements eliminate $\sim 99\%$ of sources with $J \gtrsim 19.5$ mag and $K_s \gtrsim 19$ mag. Including those sources would create a shoulder in the χ^2 -distribution towards lower values. We found that the chosen requirements offer a good compromise between depth and sensitivity to variations. The final sample for the χ^2 -analysis contains 328 985 stars (J -band) and 276 204 stars (K_s -band). A large overlap between these samples exists so that in total the χ^2 -values of 362 425 individual stars were analysed.

For a star to be considered variable its χ^2 -value must be above the 3σ -threshold in at least two pawprints for a given filter. This approach is conservative and it basically removes the tile-areas covered by only one pawprint (two stripes of width $\sim 6'$ at the tile-edges), but we prioritise reliability over completeness. It reduces the number of spurious variability detections since such objects are less likely to be above the thresholds of two or more pawprints. With these requirements 3817 of the 362 425 stars are found to be variable. 2492 of them are identified in the J -band, 2521 in the K_s -band, and 1196 are identified in both filters.

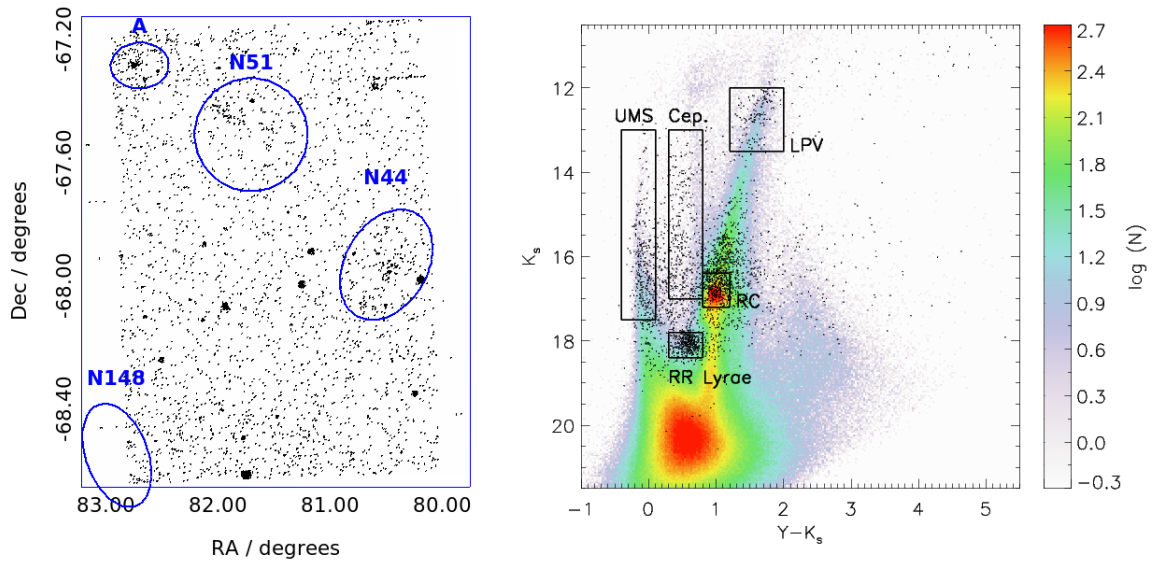


Figure 4.7: **Left panel:** Spatial distribution of the 3817 variable star candidates (black points). The labelled blue ellipses show star forming complexes (see Fig. 3.9). **Right panel:** Distribution of the 3062 unflagged high reliability variables in a $Y - K_s$ CMD. In the background is a Hess diagram of the total stellar population from the deep catalogue. The labelled boxes identify populations discussed in detail in the main text.

4.4 Analysis of the variable stars

4.4.1 General properties

The spatial distribution of the 3817 stars is shown in Fig. 4.7 (left panel), together with the locations of the star forming complexes discussed in Chapter 3. Noticeable are some tight clumps of variables, one of which is at the edge of the N 44 complex. These are coincident with very bright sources and therefore are artifacts that are flagged accordingly. Another noticeable feature are two thin horizontal stripes in the top-right corner, coincident with the top edge of detector 4, which show an overdensity of variables. The split into two separate stripes is due to the different pointings of the telescope. These variables are also flagged. In total, 755 variables are flagged as low reliability variables.

Table 4.2: Number of stars (N_{tot}), number of variable star candidates (N_{var}), and the corresponding fraction for the CMD-regions labeled in Fig. 4.7 (right panel). Note, that N_{tot} is the number of stars that fulfill the minimum detections requirement ($\text{Detections}_{K_s} \geq 10$, $\text{Detections}_J \geq 6$).

Region	N_{tot}	N_{var}	fraction (%)
Cep.	3 631	346	9.5
RR Lyrae	4 787	391	8.2
UMS	4 572	301	6.6
LPV	3 558	132	3.7
RC	71 867	364	0.5
total	362 425	3 062	0.8

In the centre of N 44 and in the top-left quadrant of N 51 a clear increase in the number density of potential variables is visible. These are located where the largest groups of UMS+PMS classified grid elements within these complexes were found (see Fig. 3.9, top panels). At first glance this might indicate a higher fraction of variables in these areas, however the number of stars in general is also increased there. Overall, most variables are distributed across the tile similar to the non-variable field population. This strongly implies that most of the identified variables belong to the field or generally more evolved stellar populations. For an analysis of the variability properties of the young population it is thus necessary to select a reliable sample of young stellar sources (Sec. 4.5).

The right panel of Fig. 4.7 shows the colour-magnitude distribution of the 3062 unflagged variables using photometric data from the deep catalogue. The distribution of the total stellar population of Tile LMC_7_5 is also plotted for comparison. Objects with $K_s > 19$ mag are very rarely found to be variable; due to their photometric uncertainties only variables with large amplitudes can be identified. Furthermore, these stars rarely meet our requirement regarding a minimum number of detections ($\text{Detections}_{K_s} \geq 10$, $\text{Detections}_J \geq 6$).

The most prominent features in the variable star CMD distribution are two clumps located in the RC and RR Lyrae regions. A concentration in the RC is unex-

pected (these stars are not expected to be variable), but a closer investigation shows that the fraction of variable star candidates is in fact considerably smaller than in any other labelled region at the CMD (Table 4.2). Hence, the enhancement of candidates in the RC region is most likely an effect caused by the higher concentration of stars in this CMD region, in combination with the non zero likelihood of having a non variable star above our χ^2 -thresholds. One should also consider that extinction could shift some Cepheids into the red giant branch, and thus also into the RC region.

The highest fractions of variables are found in the RR Lyrae and the Cepheid regions. RR Lyrae are evolved (age >10 Gyr), low-mass ($< 1 M_{\odot}$) stars populating the instability strip of the horizontal branch (e.g. Muraveva et al. 2018b). They conform to period-luminosity and luminosity-metallicity relations which turns them into useful standard candles for distance determinations (e.g. Muraveva et al. 2018b). RR Lyrae exhibit radial pulsations similar to the Cepheids, which are also evolved but more massive stars ranging from $M_{\text{ini}} \sim 3 - 12 M_{\odot}$ (e.g. Anderson et al. 2016). Long known for obeying a relation between period and luminosity (Leavitt & Pickering 1912), they are also widely used as standard candles. In the UMS region the high fraction is likely caused by various forms of early-type variability, such as slowly pulsating B-stars (Wu, Li & Deng 2018), β Cephei stars (Stankov & Handler 2005), or eclipsing binaries (Kourniotis et al. 2014). Finally, the long period variables (LPVs) are cool giant and supergiant stars with a wide range of periods from 10 days up to years (e.g. Feast et al. 1989, Soszyński et al. 2009).

Fig. 4.8 (left panel) shows the CMD distribution for the 755 flagged low reliability variables. For $K_s \lesssim 18.5$ they roughly follow the underlying stellar distribution. As our flagging criteria are unrelated to any specific stellar types, the probability of flagging a star in a certain area of the CMD is proportional to the overall stellar density in this CMD area. Consequently, the identified regions do not display an enhanced fraction of low reliability candidates. For $K_s > 18.5$ most variables are flagged (Fig. 4.8, right panel). This shows that faint stars are predominantly identified as variable if they are in the vicinity of very bright objects or within the two detector stripes, which clearly indicates that the photometry is unreliable. This is why we cannot study variability in

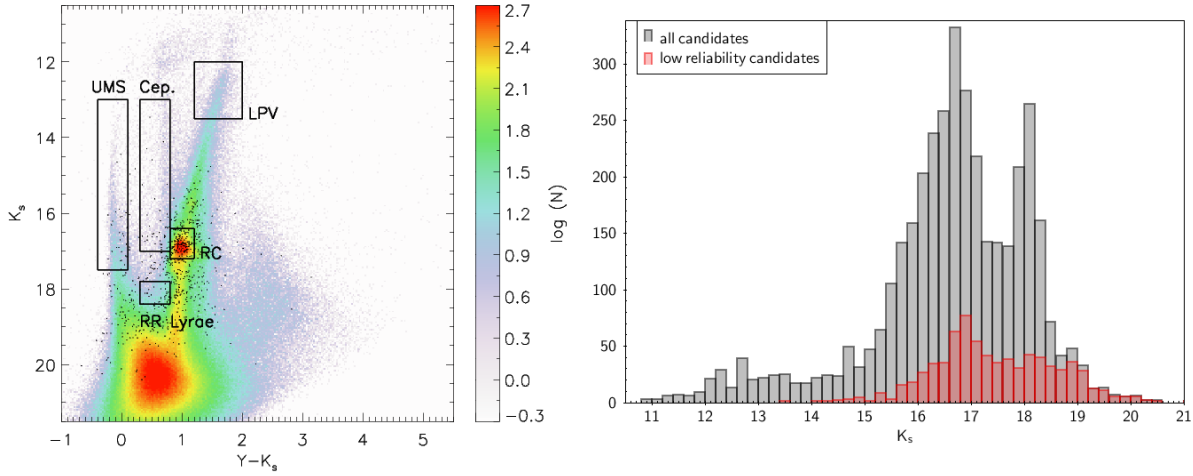


Figure 4.8: **Left panel:** Same as Fig. 4.7 (right panel) but for flagged variables with low reliability. **Right panel:** K_s distribution of all variables (grey) and of the flagged variables (red).

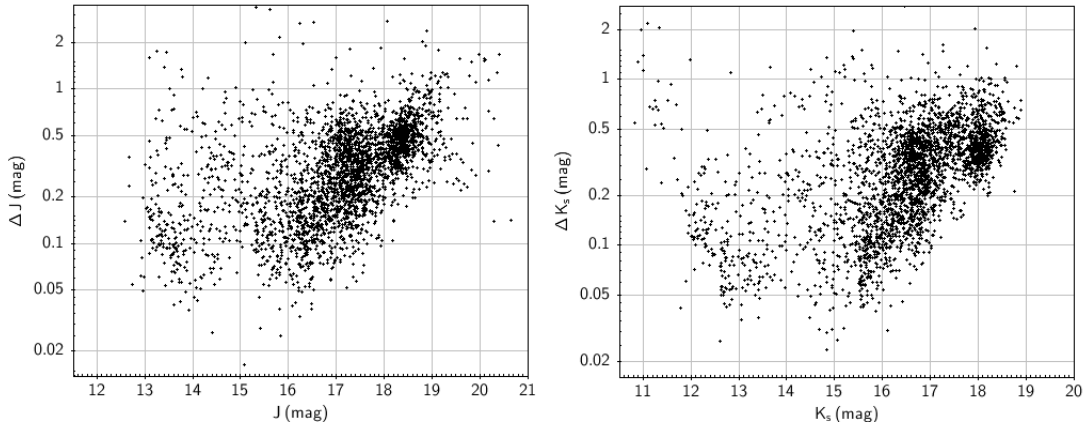


Figure 4.9: **Left panel:** J vs. ΔJ scatter-plot for the 3062 unflagged high reliability variables. **Right panel:** Same as on the left, but for the K_s -band.

the PMS populations described in Chap. 3.

Fig. 4.9 shows magnitude vs. amplitude plots for the J and the K_s -band for the 3062 identified and unflagged variables. Amplitudes are defined as the difference between the brightest and the faintest observed magnitude. The absolute minimum

amplitude for our variables is in both bands ~ 0.03 mag– 0.05 mag. This boundary is reached for $J \lesssim 17$ mag and $K_s \lesssim 16.5$ mag, and is set by our minimum photometric uncertainties. For fainter magnitudes the minimum amplitudes increase due to the larger photometric errors. In both plots a few variables are brighter than the bright magnitude cutoffs ($K_s < 12.6$ mag and $J < 13$ mag); these are variables identified using data from the other band.

4.4.2 Comparison to known samples

The increased variability fraction in CMD regions typical for variables is encouraging. However, it is important to establish how effective our approach is, i.e. what fraction amongst a sample of variables is identified as variable by our method. The Optical Gravitational Lensing Experiment (OGLE) is a sky survey which original goal was to search for dark matter by detecting microlensing phenomena (Udalski, Kubiak & Szymanski 1997). Since its inception in 1992 it was also invaluable in detecting and classifying a multitude of variables (e.g. Udalski et al. 1997; Soszyński et al. 2009; Soszyński et al. 2016).

We use data from the OGLE-III Online Catalog of Variable Stars¹, which is based on observations conducted during the third phase of the survey (Udalski et al. 2008). The OGLE-III survey area covers $\sim 60\%$ of tile LMC_7_5 and our catalogue query returned in total 4119 stars, 3240 of which have a counterpart in the deep VMC catalogue. Their spatial distribution is shown in Fig. 4.10 (left panel). We remove OGLE sources located in areas only covered by one pawprint, which do not fulfil our criteria regarding minimum number of detections (Sec. 4.3), and which are brighter than the bright limit cut-offs (Sec. 4.2.1). This leaves 2289 OGLE sources which are shown in Fig. 4.10 (right panel). Most of them are LPVs (1592), followed by RR Lyrae stars (654), while Cepheids are comparatively few (43). Overall, 445 OGLE stars (109 LPVs, 302 RR Lyrae, 34 Cepheids) were identified as variable using our approach.

¹<http://ogledb.astrouw.edu.pl/ogle/CVS/>

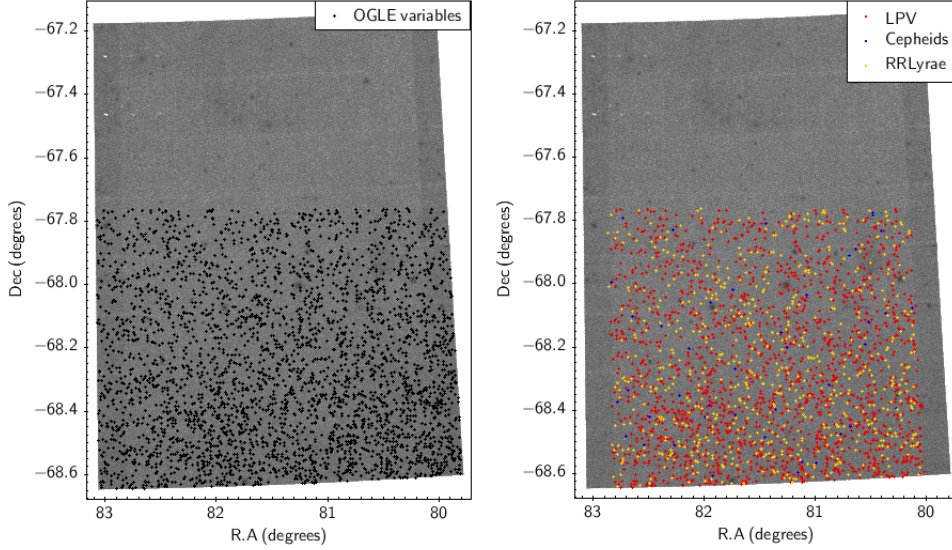


Figure 4.10: **Left panel:** Spatial distribution of the 3240 OGLE variables with counterparts in the deep catalogue. The full extent of Tile LMC_7.5 is shown in the background. **Right panel:** Distribution of the 2289 OGLE variables which are located in areas covered by at least two pawprints, and which fulfil our requirement for the χ^2 -analysis in at least one filter. The datapoints are colour-coded based on their type.

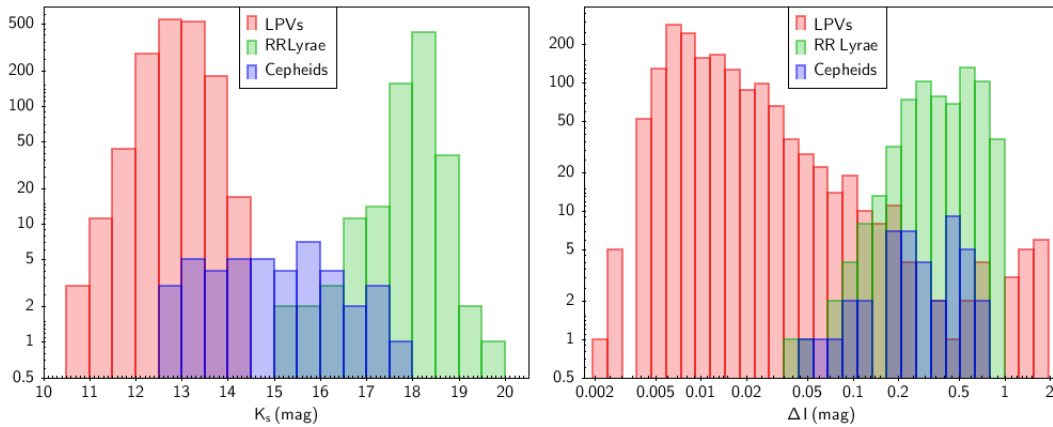


Figure 4.11: **Left panel:** Distribution of the magnitudes for the 2289 OGLE variables, colour-coded based on the variability type. The K_s values are taken from the deep catalogue. **Right panel:** Distribution of amplitudes in the I -band ($0.8 \mu\text{m}$) as given in the OGLE-III catalogue.

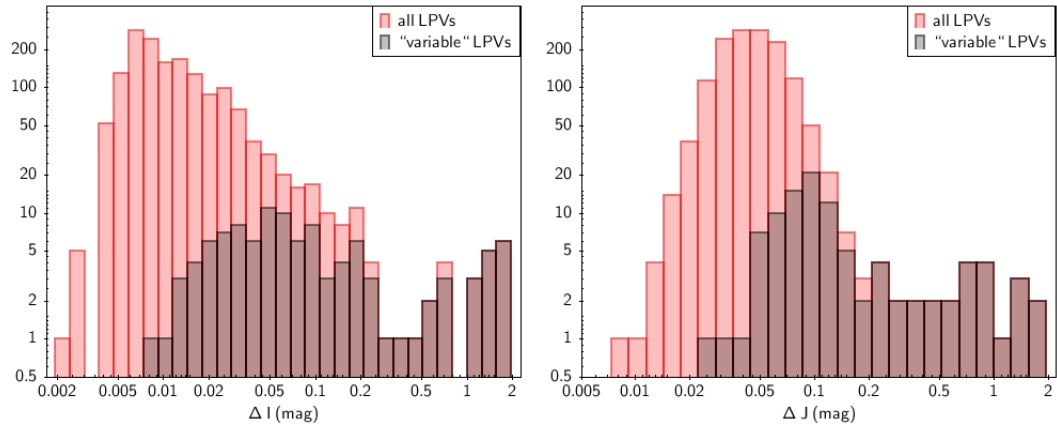


Figure 4.12: **Left panel:** Distribution of the I -band ($0.8 \mu\text{m}$) amplitude for the sample of LPVs (red), and for the LPVs identified as variable by our analysis (black). **Right panel:** As on the left but for the J -band amplitude.

These three types are very distinct in K_s -band magnitude and I -band amplitude as can be seen in Fig. 4.11. The LPVs display a wide range in amplitudes, however most of them have small amplitudes ($\Delta I < 0.1 \text{ mag}$). Due to their brightness ($K_s \lesssim 14 \text{ mag}$), this subsample is useful to find the lower amplitude limit which even bright variables must reach in order to be identified by our method. Indeed, only 109 out of the 1592 LPVs are identified as variable. Figure 4.12 (left panel) reveals that this is due to the small amplitude of most LPVs. In fact, the majority of LPVs with $\Delta I > 0.05 \text{ mag}$ are recovered ($\sim 55\%$). The fraction rises further to $\sim 66\%$ and $\sim 90\%$, for $\Delta I > 0.1 \text{ mag}$ and $\Delta I > 0.2 \text{ mag}$, respectively. Note that these I -band amplitudes are from the OGLE-III catalogue. Figure 4.12 (right panel) shows the amplitudes we find in our J -band data². For a $\Delta J \geq 0.08 \text{ mag}$ we identify $\sim 50\%$ of the LPVs as variable. In the K_s -band the amplitudes need to be slightly higher for a similar success rate: $\sim 50\%$ LPVs are identified for $\Delta K_s \geq 0.11 \text{ mag}$.

The amplitudes of the 43 Cepheids are in general above the amplitude limits

²A few OGLE-LPVs are more luminous than our bright magnitude cutoff in J . Hence, they are not analysed in J due to possible saturation effects. Only the K_s -band photometry is then used for the variability analysis.

established in the LPV analysis. In numbers, 39 and 38 Cepheids exhibit $\Delta J > 0.1$ mag and $\Delta K_s > 0.1$ mag, respectively. In combination with their high luminosities, this leads to a high success rate in identifying them as variables ($\sim 80\%$, 34 out of 43). By comparison, $\gtrsim 90\%$ of the 654 RR Lyrae stars exhibit amplitudes above 0.1 mag in both filters. However, due to their comparatively low luminosities we find only 302 RR Lyrae stars ($\sim 46\%$) to be variable. As Cepheids and RR Lyrae stars have roughly similar amplitudes, both samples can be combined to examine the typical amplitude needed for variability identification across a wide range of magnitudes. Figure 4.13 shows these merged samples in the J vs. ΔJ plane (top panel). As expected, the identified variables tend to populate the upper part of the diagram, indicating high amplitudes. For $J \lesssim 17$ mag most sources with $\Delta J > 0.1$ mag are identified as variable. By $J \approx 18$ mag this limit is $\Delta J \approx 0.2$ mag, and it reaches $\Delta J \approx 0.5$ mag for $J \approx 19$ mag.

In contrast to the LPVs and Cepheids, the success rate of identified variability in RR Lyrae stars varies dramatically depending on the filter. All of the 302 variability detections of the RR Lyrae stars made use of J -band data. Only 8 of them are also variable in the K_s -band. Hence, the amplitude needed for variability detection in K_s is, at typical RR Lyrae magnitudes, larger than the typical RR Lyrae amplitudes. RR Lyrae stars are expected to have smaller amplitudes at longer wavelengths (Monson et al. 2017), which could lead to this discrepancy. However, in our case the main reason is the larger photometric error in the K_s -band compared to similar magnitudes in the J -band (see Fig. 4.2). Indeed, Figure 4.13 shows that the amplitudes of RR Lyrae stars, which form the prominent clump, are very similar in both bands. The K_s vs. ΔK_s plot (bottom panel) suggests a required amplitude of $\Delta K_s \approx 0.5$ mag for $K_s \approx 18$ mag, which is not reached by the RR Lyrae stars.

Based on the results from the comparison with OGLE samples we can conclude the following. To reliably detect variability, i.e, with a completeness of $\gtrsim 50\%$, an amplitude of ~ 0.1 mag is needed for stars with $J \lesssim 17$ mag and $K_s \lesssim 16$ mag. At fainter magnitudes the required amplitude is larger, reaching ~ 0.5 mag for $J \approx 19$ mag and $K_s \approx 18$ mag. Most of the selected young stars (explained in Sec. 4.5) are brighter than these values, we thus expect to find young variables with amplitudes below 0.5 mag.

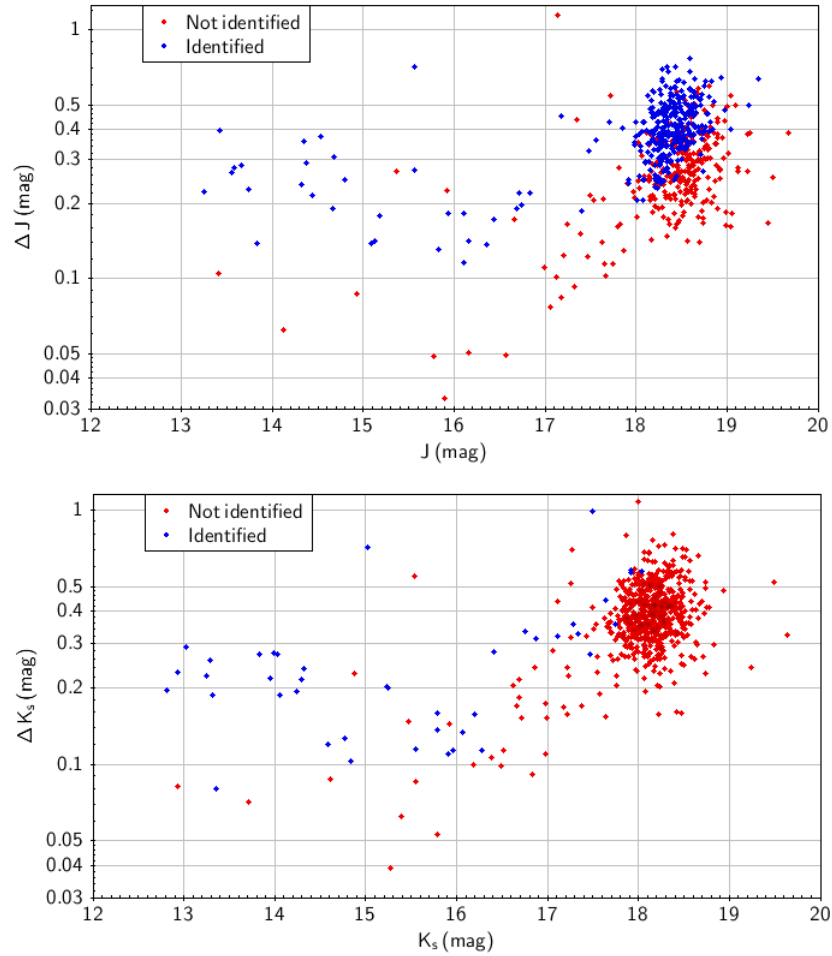


Figure 4.13: **Top panel:** J vs. ΔJ scatter-plot for the Cepheids and RR Lyrae stars combined: identified as variable (blue), not identified as variable (red) in the J -band. **Bottom panel:** Same as on top, but for the K_s -band.

4.4.3 Periodicity tests

The VMC survey is not designed with the goal of determining periods of variable stars. Nevertheless it is useful to consider the sensitivity of our variable star catalogue to a range of periods, since this can provide additional clues about the origin of the observed variability. We make use of periods listed in the OGLE catalogue for the period sensitivity tests.

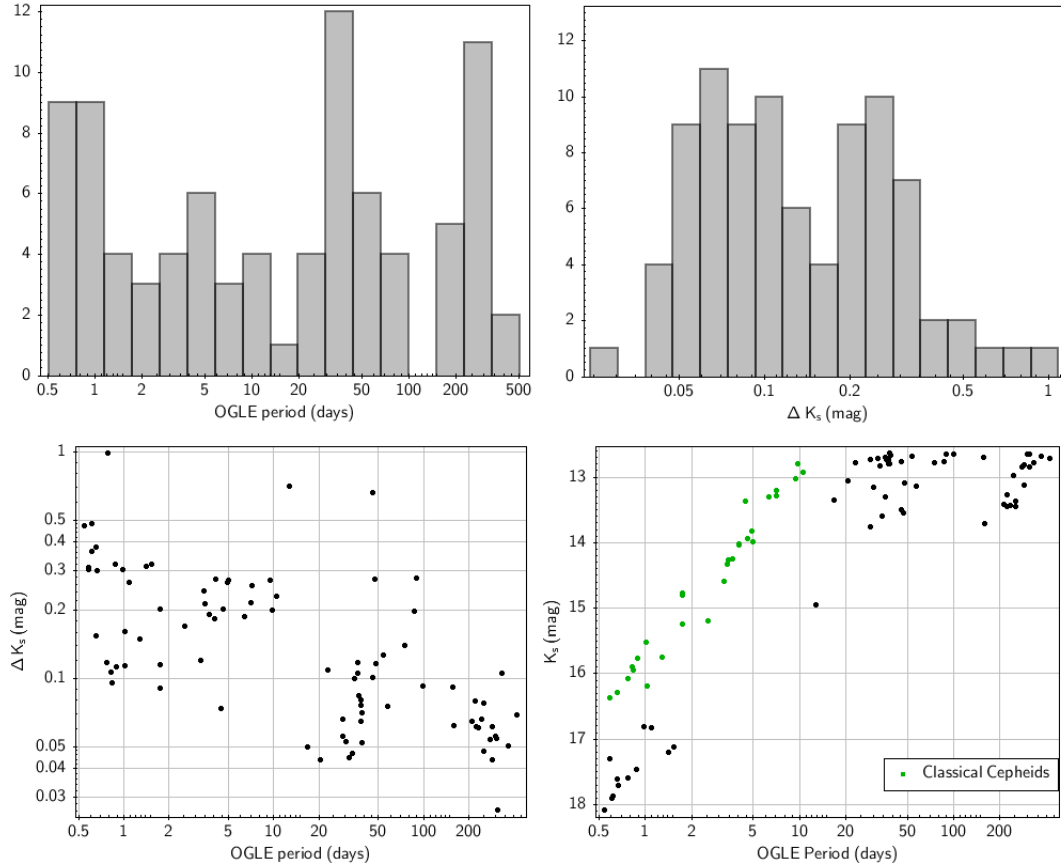


Figure 4.14: Various properties of the 87 OGLE stars found to be variable in the K_s -band. **Top left:** Distribution of the periods according to the OGLE-III catalogue. **Top right:** Distribution of the amplitudes in K_s . **Bottom:** Period vs. K_s amplitude (left) and Period vs. K_s magnitude (right).

Given that the number of epochs is larger for the K_s -band (24 compared to 15 in J), we focus on the K_s -band data for the period analysis. In total, 87 OGLE variables are identified as variables using K_s -band data: 34 Cepheids, 45 LPVs, and 8 RR Lyrae stars. This sample covers a wide range of periods and amplitudes (Fig. 4.14, top panels). We note that intrinsic stellar properties affect our analysis. For instance LPVs are bright with low-amplitude variability, while classical Cepheids tend to be fainter, have shorter periods, but higher amplitudes.

To investigate our ability to detect periodicity in this OGLE sample we use

the LombScargle class from the astropy library³. It is designed to detect periodic signals in unevenly spaced observations (Lomb 1976; Scargle 1982), therefore it is well suited for our data. As input parameters it uses the dates of observation, magnitudes, and photometric errors. Based on the number of epochs and the overall monitoring baseline it is equipped with a heuristic that determines a suitable grid of frequencies to be tested. The highest default frequency is chosen to be 5 times larger than the average Nyquist-frequency $f_{\text{Nyquist}} = \frac{1}{2} f_s$, where f_s is the average sampling rate. For our K_s data with a baseline of 2175 days and 24 epochs this translates into a shortest probed period $P_{\min} \approx 36$ days. This limit is not particularly useful for our highly irregular spacing, where several epochs were obtained in successive nights including two epochs observed in one night. Furthermore, almost 60% of the OGLE stars used in this test have periods less than 36 days. Instead we test a list of periods between the extremes $P_{\min} = 0.55$ days and $P_{\max} = 1000$ days, which covers the full range of the OGLE periods. The LombScargle class fits internally a sinusoidal model of appropriate amplitude to the data for each period given in the list. A power value for every period is calculated (a higher value represents a better fit). In addition, it provides also a false alarm probability (FAP) for every period listed. The period with the highest power is taken to be the period of the lightcurve, usually under the condition that the FAP must be below a defined value.

Different lists of periods containing between 100 and 2000 periods in a logarithmic spacing between P_{\min} and P_{\max} were tested by evaluating how well the calculated periods matched the OGLE periods. We found that a list of 500 periods gives the best results. Above 500 periods there is no further improvement in the periods recovered. Below 500 periods tested the resolution is too coarse. A period was deemed recovered if between the tabulated OGLE period and the computed period there are less than 25 entries in the input period list. This ensures that the error is related to the underlying period resolution; the calculated period must be approximately within $\pm 40\%$ of the OGLE value. The number of tested periods between the calculated period and the

³<http://people.bolyai.elte.hu/~sic/astropy/stats/lombscargle.html#id16>

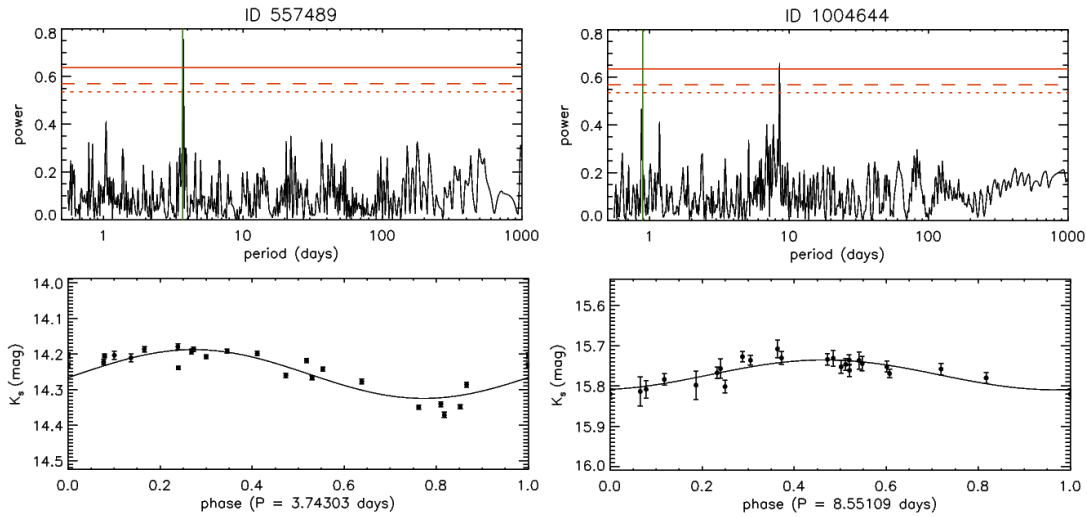


Figure 4.15: **Top left:** Periodogram example for a source with a successfully recovered OGLE period, using the 500 period list. The vertical green line shows the OGLE period (~ 3.7 days). Three horizontal lines indicate the FAP levels of 10% (dotted), 5% (dashed), and 1% (solid). **Bottom left:** Corresponding folded lightcurve for the calculated period, with the sinusoidal model overplotted. **Right panels:** As for the left panels, but for a star where the OGLE period of ~ 0.9 days was not successfully recovered. Note the low amplitude of the variations.

OGLE period is henceforth called period-steps.

Figure 4.15 shows example periodograms and folded lightcurves for sources with a successfully recovered OGLE period (left) and an OGLE period not recovered (right). The example on the left has a clear power-peak consistent with the OGLE period of 3.7 days. One of the 500 probed periods is closer to the OGLE period than the actual highest power period; hence, the period-steps value is one. The folded lightcurve matches the sinusoidal model very well. For the example on the right (OGLE Period ≈ 0.9 days) the period-step value is 150, well above the maximum allowed value of 25. Consequently, the OGLE period was not recovered. Note that the folded lightcurve appears to follow the model well, but its amplitude is comparable to the photometric errors.

Overall, only 36 out of 87 OGLE periods are successfully recovered in our period

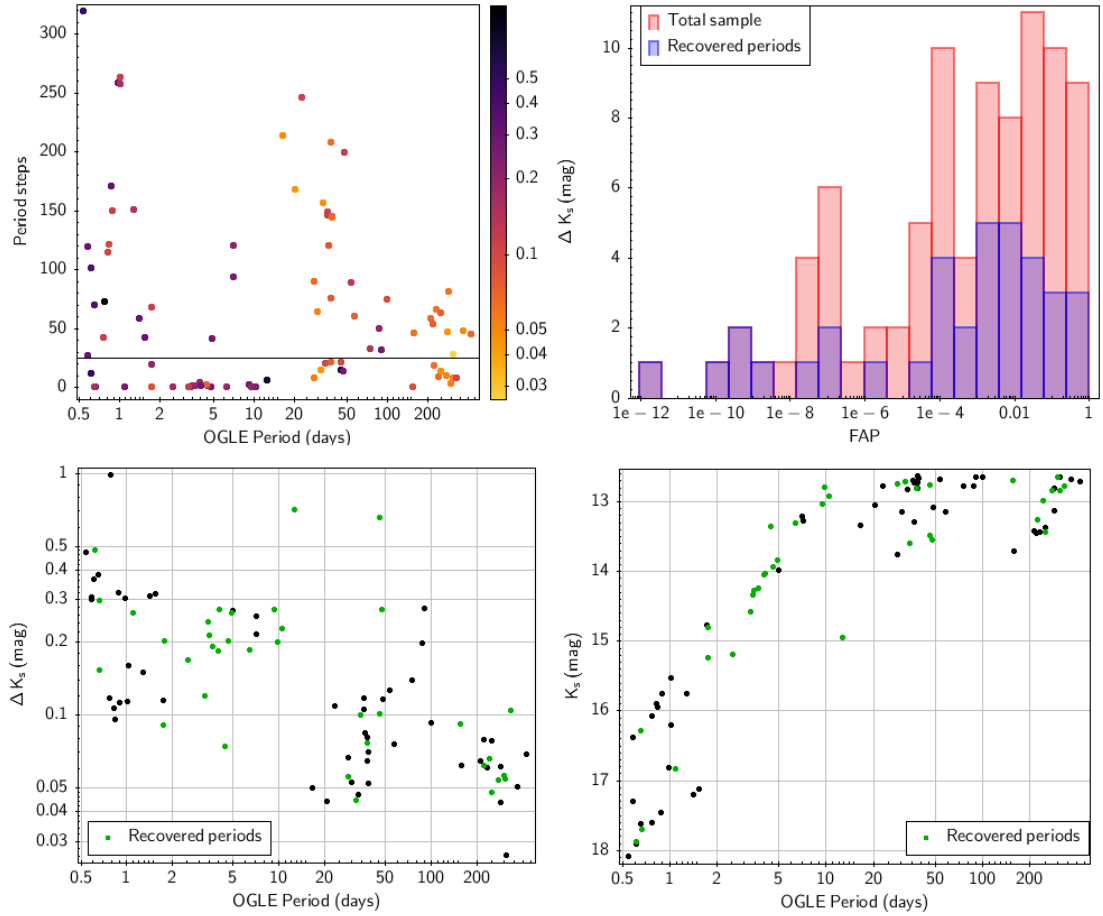


Figure 4.16: **Top left panel:** Period-steps vs. OGLE-period. Stars below the horizontal line (period-steps = 25) are considered successful period detections. The solid circles are colour-coded based on the K_s amplitude. **Top right panel:** Distribution of the FAPs for the OGLE sample, and for the stars with recovered periods. **Bottom panels:** Same as Fig. 4.14 (bottom panels), but with the recovered periods highlighted.

analysis. The distribution of the period-steps for all stars is shown in Fig. 4.16 (top left panel). In the range 2–20 d the OGLE periods are well recovered in general; for 15 out of 19 stars we determined the correct periods ($\sim 79\%$). For $P > 20$ d the success rate drops sharply (15 out of 44, $\sim 34\%$). As shown in the bottom left panel of Fig. 4.16 the amplitudes do not appear to be the reason for this behaviour. Instead the high cadence observations of our own programme probably increased the sensitivity

preferentially in the 2–20 d range. For the shortest periods (< 2 d) the results are also unsatisfactory (6 out of 24, 25%). A possible reason for the low success-rate could be the objects fainter magnitudes, even though magnitudes already decrease gradually for sources with $P \lesssim 5$ d (Fig. 4.16, bottom right panel). We conclude that our observing cadence is not suited to reliably identify such short periods. With the exception of two epochs observed in the same night, all other epochs have at least 1 day separation.

In Fig. 4.16 (right panel) the FAP-distributions for the entire OGLE sample and for the stars with successfully recovered periods is shown. The latter does not suggest a reasonable FAP threshold that could be used as an indicator for a correctly determined period. Therefore, our observational parameters (Number of epochs, total time baseline, cadence) do not seem suited for an automated periodicity search. For the subsequent analysis we do not make use of the FAP as a period reliability indicator, and only consider the periodicity if a visual inspection of the lightcurves corroborates a periodic behaviour.

The findings of our periodicity analysis can be summarised as follows: Periods shorter than 2 d are rarely recovered independent of amplitude. The observing cadence is not sufficient for reliable short period detection. The best sensitivity is achieved in the 2 d–20 d range, where we recover 15 out of 19 OGLE periods ($\sim 79\%$). The additional epochs from our open time programme have a noticeable effect on the sensitivity. For $P > 20$ d period recovery degrades considerably (15 out of 44, 34%). Regarding YSOs we would thus expect to be most sensitive to periodicity caused by rotational modulation of stellar spots, or by phenomena related to the inner disc (Wolk, Rice & Aspin 2013).

4.5 The massive YSO sample

Given the star formation history of the LMC the large majority of stars are comparatively old, with ages > 1 Gyr (Rubele et al. 2012). Consequently, most stars analysed in Sec. 4.3 are not young. In Chapter 3 young stellar populations were identified using

a statistical method, based on overdensities in the CMDs, that does not provide a list of likely YSOs. Furthermore, the method was geared towards PMS stars of relatively low mass ($\lesssim 4 M_{\odot}$, $18 \lesssim K_s \lesssim 22$ mag), therefore these objects do usually not fulfil our detection requirement for χ^2 -analysis. To investigate variability characteristics of young stars in LMC 7.5 (Sec. 2.3), we define a reliable sample of earlier stage, higher mass YSOs.

4.5.1 *Spitzer* source selection

Several wide-field studies on massive star formation in the LMC used *Spitzer* data for the identification and analysis of YSOs (see Sec. 1.4.1). These YSOs are massive and luminous enough to be reliably detected in the individual pawprints. Furthermore, they tend to be in an early evolutionary stage in which stars are more frequently variable (e.g. Cody et al. 2014), and high amplitude variability is more common (e.g. Contreras Peña et al. 2014). To create our massive YSO sample we select stars from the following studies:

- **Gruendl & Chu (2009):** This study carried out independent aperture photometry on archival *Spitzer* data from the LMC to obtain photometry for over 3.5 million sources. The data was obtained from observations of the *Spitzer* SAGE program (Meixner et al. 2006) which mapped the central $7^{\circ} \times 7^{\circ}$ of the LMC. Applying colour and magnitude cuts to remove evolved stars and background galaxies, they identified a sample of 2910 potential YSOs. 150 of them are located within Tile LMC 7.5 in areas covered by at least two pawprints. To further decrease the likelihood of contaminants we selected only sources which are spatially associated with the PMS contours seen in Fig. 3.15, which leaves 79 YSO candidates.
- **Carlson et al. (2012):** This work focuses on nine large star forming complexes in the LMC. Two of them, N 44 and N 51, are located in Tile LMC 7.5. This work uses a combination of SAGE IRAC and MIPS data in the wavelength

range 3.6 - 24 μm , optical photometry ($UBVI$) from the MCPS (Zaritsky et al. 2002; Zaritsky et al. 2004), and NIR data (JHK_s) from the InfraRed Survey Facility (IRSF; Kato et al. 2007). As a first step a colour-magnitude selection in the *Spitzer* bands was applied, followed by a spectral energy distribution (SED) fit based on YSO models from Robitaille et al. (2006). This resulted in a sample of 1045 well-fit YSO candidates out of which 242 are located in N 44 and N 51. Based on the SED fitting 157 stars were classified as Class I, 64 as Class II, and 21 as Class III.

- **Seale et al. (2009):** Based on Gruendl & Chu (2009) analysis this study selected 294 objects which are highly embedded in their natal clouds for follow-up *Spitzer*-IRS spectroscopy. In total, 277 stars had spectral features consistent with embedded YSOs. These features include polycyclic aromatic hydrocarbon emission, ice absorption features, deep silicate absorption, and fine-structure emission lines. Of these, 42 YSOs are located in Tile LMC 7_5, and were added to the YSO sample without further constraints, since this spectroscopically confirmed set is highly reliable. In addition we also add five spectroscopically confirmed YSOs from Jones et al. (2017), which brings the number of high reliability YSOs to 47.

After defining these three samples, comprising in total 368 YSOs, we first eliminate the duplicates by cross-matching the samples. This removes 22 objects resulting in a sample of 346 unique YSOs.

4.5.2 Matching with VMC catalogues

The YSOs are matched with the deep VMC-catalogue. This links every *Spitzer* YSO with the source ID provided by the deep catalogue, which allows the tracking of the YSOs throughout all epochs and pawprints (see Sec. 4.2). Since the astrometric error of the *Spitzer* Infrared Array Camera (IRAC) can be up to $2''$ ⁴, we pick this as the

⁴<https://irsa.ipac.caltech.edu/data/SPITZER/docs/irac/iracinstrumenthandbook/30/>

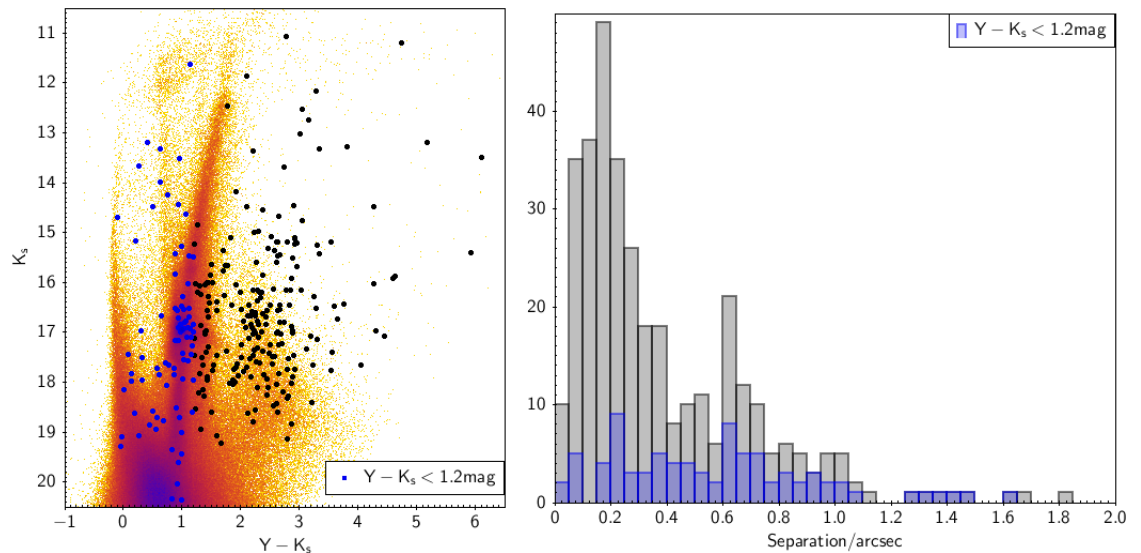


Figure 4.17: **Left panel:** Location of the deep catalogue YSO counterparts in the $Y - K_s$ CMD shown as solid circles. In the background is the total stellar population displayed for comparison. **Right panel:** Distribution of the spatial separation between matched pairs for all YSO counterparts (grey), and for the subsample where the counterparts are comparatively blue ($Y - K_s < 1.2\text{mag}$).

initial catalogue matching radius. This successfully finds a counterpart for every YSO, which is however not an indication that all matches are correct.

The distribution of the YSO counterparts in the $Y - K_s$ CMD shows (Fig. 4.17, left panel) an unexpected abundance of relatively blue sources. In principle, young stars can be located in these CMD areas shortly before they settle onto the main-sequence (see for example the isochrones in Fig. 3.6). However, most YSOs in this sample should be very young and therefore considerably redder. The concentration of YSO counterparts in the RC is also indicative of a contamination by non-YSOs. The spatial separations for the matched pairs show a different distribution for the counterparts that are as blue or bluer than the RC (Fig. 4.17, right panel). These blue sources display a relatively flat separation distribution leading to a high fraction of matches at large separations, while the overall distribution is peaked at smaller separations. For separations $> 0.75''$ the blue sources dominate the distribution. To

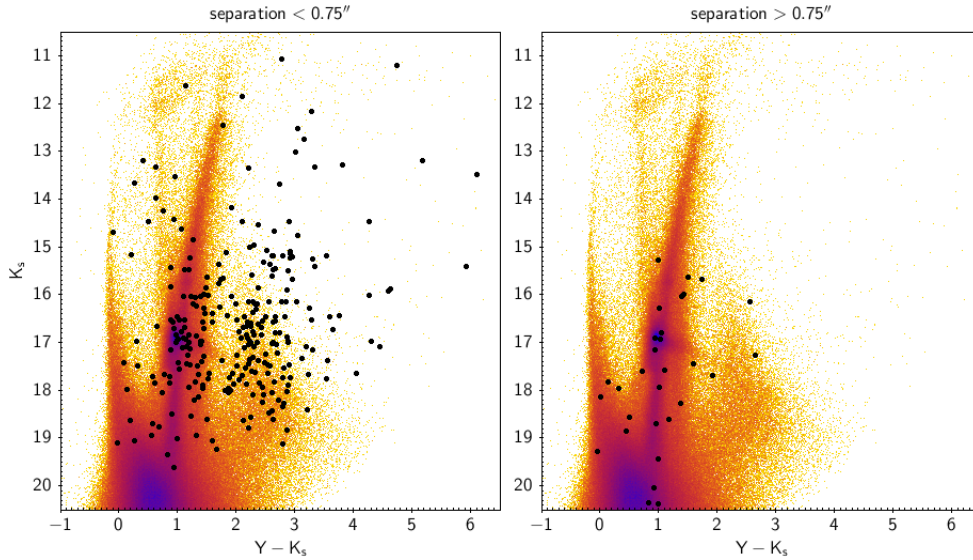


Figure 4.18: **Left panel:** As Fig. 4.17 (left), but only for counterparts with a separation $< 0.75''$. **Right panel:** As on the left, but for counterparts with a separation $> 0.75''$.

increase the reliability of the catalogue matching, only counterparts with a separation of $\leq 0.75''$ are therefore considered. Using this more restrictive radius, 305 YSOs are successfully matched. Figure 4.18 shows how the excluded sources are distributed in the $Y - K_s$ CMD (right panel), compared to the sources remaining (left panel); most of the excluded sources are relatively blue. Nonetheless, the distribution of the remaining objects indicates some contamination, i.e. a still noticeable RC.

4.5.3 Removing contaminants

4.5.3.1 Colour criteria

Spezzi et al. (2015) combined VISTA and *Spitzer* observations to investigate the young stellar content of the Lynds 1630 star forming region located in the Orion molecular cloud. Using multi-colour criteria, 186 YSO candidates were selected which have an age of 1–2 Myr (Spezzi-YSOs from now on). Based on their YSO sample we devised criteria for the removal of contaminants. We note that the Spezzi-YSOs have masses

mostly in the subsolar mass regime, while our YSO sample has masses $\gtrsim 3 M_{\odot}$ (Carlson et al. 2012).

Figure 4.19 displays a $(K_s - [3.6], Y - K_s)$ CCD, including both the Spezzi-YSOs and our massive sample. Both sets of stars deviate substantially from the underlying distribution of more evolved stars, reaching considerably redder colours. However, the two samples also differ amongst each other. Whilst some sources from the Spezzi-YSOs are very red with $K_s - [3.6] > 2$ mag, most show rather moderate colours. In contrast, our YSOs are predominantly redder in $K_s - [3.6]$. This is likely due to an, on average stronger infrared excess. The Spezzi-YSOs are mostly Class II objects (126 out of 186, Spezzi et al. 2015), indicating that these stars have prominent circumstellar discs. However, our largest sample consists mostly of Class I objects (Carlson et al. 2012), which are still surrounded by massive envelopes. Hence, the difference in the CCD distributions is likely associated to difference in evolutionary stage.

We devised empirical colour-cuts (solid lines in Fig. 4.19) as follows:

- $Y - K_s \geq 1.1$ mag
- $K_s - [3.6] \geq 0$ mag
- $Y - K_s \geq 2.2 - 2.2 \times (K_s - [3.6])$

YSOs which are outside of these boundaries are removed from further analysis. This eliminates the cluster of sources located in the RC region at $Y - K_s \approx 2.2$ mag and $K_s - [3.6] \approx 0.15$ mag, and leaves 207 YSOs for subsequent visual inspection (Sec. 4.5.3.2). Figure 4.20 shows the distribution of the 207 YSOs on the $Y - K_s$ CMD, divided into the three sub-samples presented in Sec. 4.5.1. The YSOs from Carlson et al. (2012) are noticeable fainter. As this study targeted specifically star forming complexes, the authors applied fainter and bluer magnitude and colour cuts, which on a galaxy-wide scale would have lead to a significant contamination, but are very effective when used in regions with active star formation. This allows the identification of lower mass candidates missed by other studies, as confirmed by Fig. 4.20.

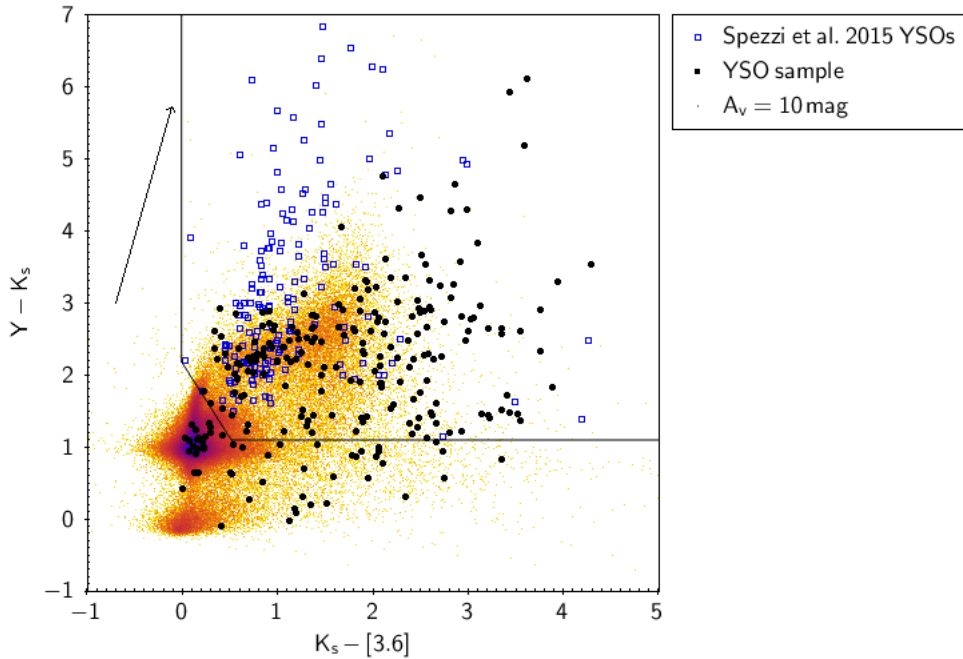


Figure 4.19: $K_s - [3.6]$ vs. $Y - K_s$ CCD showing the YSOs from Spezzi et al. (2015) (blue) and massive YSOs (black). The background is the overall stellar population. The $3.6 \mu\text{m}$ photometry is taken from the SAGE catalogue (Meixner et al. 2006), all other filters are from the VMC deep catalogue. Solid lines show the colour cuts, and the arrow represents the reddening vector for $A_V = 10 \text{ mag}$ (Nishiyama et al. 2009).

4.5.3.2 Visual examination

We make use of the superior VISTA-resolution to identify possible non-YSO sources that still contaminate our samples. Both background galaxies and small “clusters” cannot be entirely removed by using photometric criteria, however some remaining contaminants of those types can be identified by looking at the VMC images. The visual examination is performed on colour composite VISTA images (YJK_s bands); the appearance of 207 YSO candidates is judged based on shape and intensity profile.

We find 12 sources that are spatially resolved and look like galaxies which we then remove from our YSO sample. Figure 4.21 (left panel) shows an example of a possible galaxy seen edge-on.

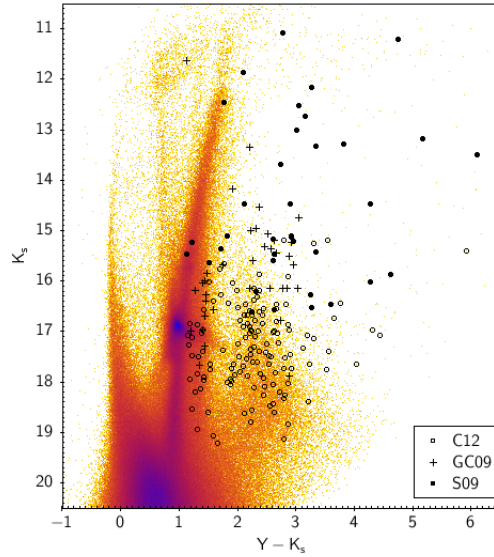


Figure 4.20: CMD with the total stellar population and showing the YSO sources which fulfilled the colour criteria (see text). The type of data-point is coded based on the study which identified the YSO (C12: Carlson et al. 2012; GC09: Gruendl & Chu 2009; S09: Seale et al. 2009).

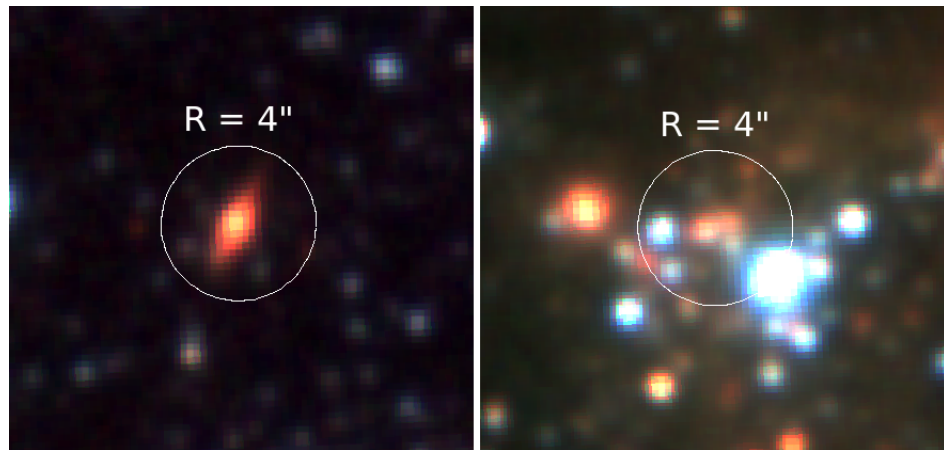


Figure 4.21: **Left panel:** VISTA RGB composite with Y ($1.02 \mu\text{m}$) in blue, J ($1.25 \mu\text{m}$) in green, and K_s ($2.15 \mu\text{m}$) in blue showing a *Spitzer*-identified YSO that is likely a background galaxy. **Right panel:** As on the left, but for source resolved into a group of stars. The radius of the circle corresponds to 1 pc at LMC distance.

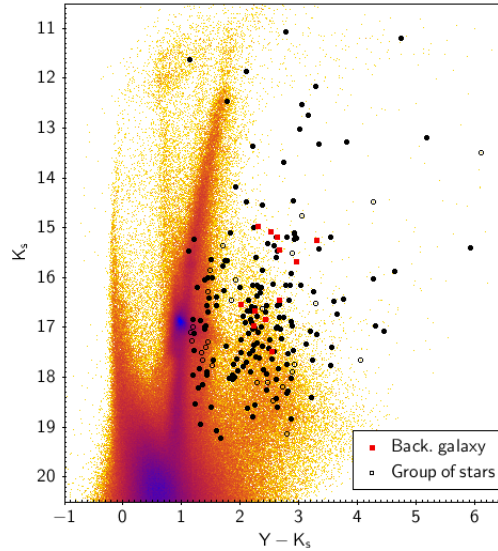


Figure 4.22: As Fig. 4.20, but for background galaxies and star groups.

29 *Spitzer*-YSOs are resolved into two or more sources by VISTA. In this case the VMC-counterpart is flagged, but not removed from the YSO sample. Figure 4.21 (right panel) shows an example of a *Spitzer*-YSO which is resolved into multiple sources in the VMC images. Note that the K_s -band brightness is dominated by two red sources that are both likely to be young. The CMD distribution of background galaxies and groups can be seen in Fig. 4.22. The colours and magnitudes of background galaxies are all within $15 \text{ mag} < K_s < 18 \text{ mag}$ and $2 \text{ mag} < (Y - K_s) < 3.5 \text{ mag}$, consistent with the expected locations of background galaxies (e.g. Kerber et al. 2009). In contrast, the sources found to be part of a group are not confined to a comparatively tight range.

Removal of the possible background galaxies narrowed down the YSO sample to 195 stars. Finally, we check if the YSOs fulfil the requirements for the χ^2 -analysis (Sect. 4.3) and if they are below our bright magnitude cutoff (Sect. 4.2.1) in at least one band. This removes 22 sources (21 have not enough detections, one is too bright in both bands), so that the final YSO sample contains 173 stars. They have a median magnitude of $\overline{K_s} \approx 16.7 \text{ mag}$ with a 10th and 90th percentile of $K_{s,10} \approx 14.5 \text{ mag}$ and $K_{s,90} \approx 17.8 \text{ mag}$. For the J -band the corresponding values are $\overline{J} \approx 18.3 \text{ mag}$,

$J_{10} \approx 16.3$ mag, and $J_{90} \approx 19.5$ mag.

4.6 Results and discussion

Our sample of 173 YSOs was examined for variability according to the selection criteria from Sec. 4.3. As a result 39 objects were found to be variable. For each object the K_s lightcurves are examined and classified based on their appearance. Examples for every class are presented in the corresponding sections. We also investigate the colour, magnitude, and amplitude distributions of the YSO variables.

4.6.1 Lightcurve classification

We classify the lightcurves based on their shape, which may be connected to the physical processes causing the variability. The classes closely follow the scheme adopted by Contreras Peña et al. (2017b) in their study of Galactic young star variables. While they focus on high amplitude stars ($\Delta K_s > 1$ mag), this scheme was also used in Teixeira et al. (2018) for stars of lower amplitudes. The classes are eruptives, dippers, faders, short-term variables (STV), and long period variables YSOs (LPV-YSO). Since our analysis is not very sensitive to long periods (Sec. 4.4.3), we employ the LPV-YSO class as a second level classification (see discussion in Sec. 4.6.2). For the classification we focus mainly on the K_s lightcurves; the number of observed epochs is higher, therefore the time-sampling is better. All YSOs are brighter in the K_s -band which implies smaller photometric errors when compared to the J measurements. As will be shown in Sec. 4.6.3, most YSOs are identified as variable only in the K_s -band. However, in some cases the J lightcurve is helpful in constraining the possible origin of the variability. In the next subsections we describe each classification in detail.

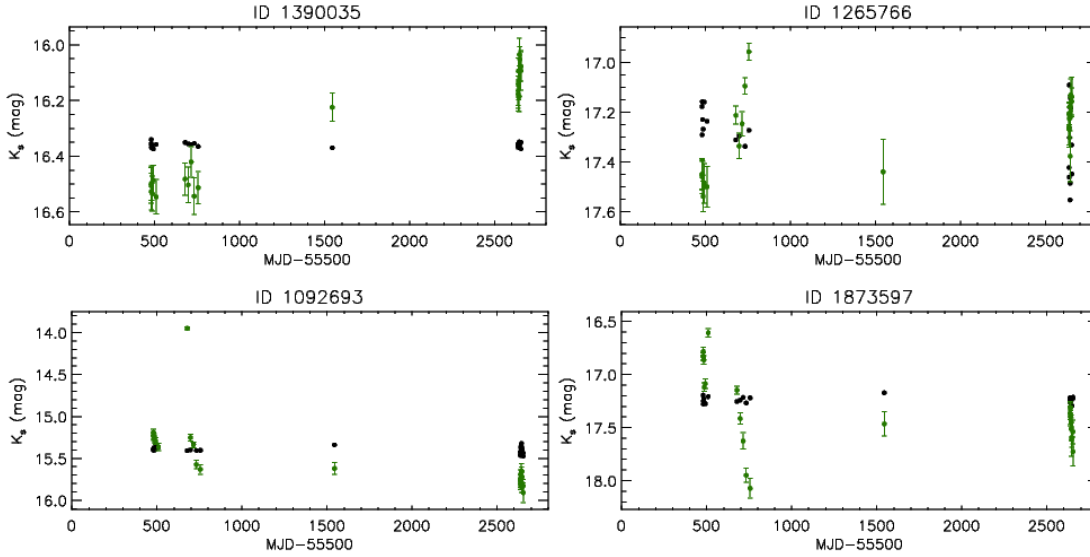


Figure 4.23: Examples for lightcurves of stars identified as eruptives (green circles). The black circles show the lightcurve of a nearby non-variable star (separation $< 3'$) with similar K_s -band magnitude for comparison. Since the photometric errors are very similar we have omitted plotting the errorbars for the companion star. In all lightcurves we use epoch magnitudes obtained from the individual pawprints.

4.6.1.1 Eruptive

Eruptives are aperiodic YSOs which experience outbursts resulting in an increase in luminosity. The outbursts are typically of long duration (> 1 yr, Contreras Peña et al. 2017b), but some YSOs display shorter outbursts. This type of lightcurves are thought to be evidence of accretion events, or of changes in the line-of-sight extinction in which case the star would move along the reddening vector in CCDs (Contreras Peña et al. 2014). FUors and EXors are known examples of stars showing eruptive behaviour (see Sec. 1.2).

The YSOs classed as eruptives display a variety of lightcurves. Figure 4.23 shows four rather distinct examples of eruptive stars. The example in the top left panel is the most commonly observed type in our data; a slow increase in K_s -band magnitude is observed over several years. The lightcurve is typical for FUors, however known Galac-

tic examples usually exhibit larger amplitudes and a faster increase in brightness (e.g. Hartmann & Kenyon 1996), although slower rises have also been observed (Contreras Peña et al. 2017a). The K_s -band magnitude may increase beyond our observational window, therefore the observed amplitude of $\Delta K_s \approx 0.51$ mag (for the particular example in Fig. 4.23) is likely a lower limit. The top right panel shows an YSO with a comparatively sudden outburst, after which it falls back to its quiescent level by the middle of the observing window before a second outburst develops. This object could be periodic and the LombScargle analysis calculates a period of ~ 970 days. In the bottom left panel the object shows a significant peak ($\Delta K_s \approx 1.5$ mag), only seen in one epoch. This magnitude change resembles the sharp luminosity increases seen in EXors (Moody & Stahler 2017). It is the only YSO in our sample with this type of lightcurve. Finally, the star in the bottom right panel experiences a fast initial increase ($\Delta K_s \approx 0.7$ mag) before it drops severely by $\Delta K_s \approx 1.5$ mag, followed by a return to an apparently stable level. We have classified this source also as a dipper due to its behaviour after the initial outburst. Based on its lightcurve a combination of processes, like an accretion event followed by some kind of obscuration, seems likely.

In total, 12 YSOs are classified as eruptive variables which makes this the most common class. In six cases the lightcurves are similar to the one in the top left panel, thus allowing us to calculate only a lower limit for the duration of the outburst (~ 4 yr in the example shown). All three YSO variables with $\Delta K_s > 0.6$ mag (see Fig. 4.31 left panel) are eruptives, although one of them (Fig. 4.23, bottom right) is also classified as a dipper.

4.6.1.2 Fader

Fader are aperiodic variables with declining luminosity. The decline can be slow over the course of months and years or relatively sudden. The physical origins of the change in brightness are similar to that of the eruptives. They can either be a star returning to quiescent levels after an outburst, or the fading can be caused by a long lasting increase in line-of-sight extinction (Findeisen et al. 2013). If extinction is the cause of

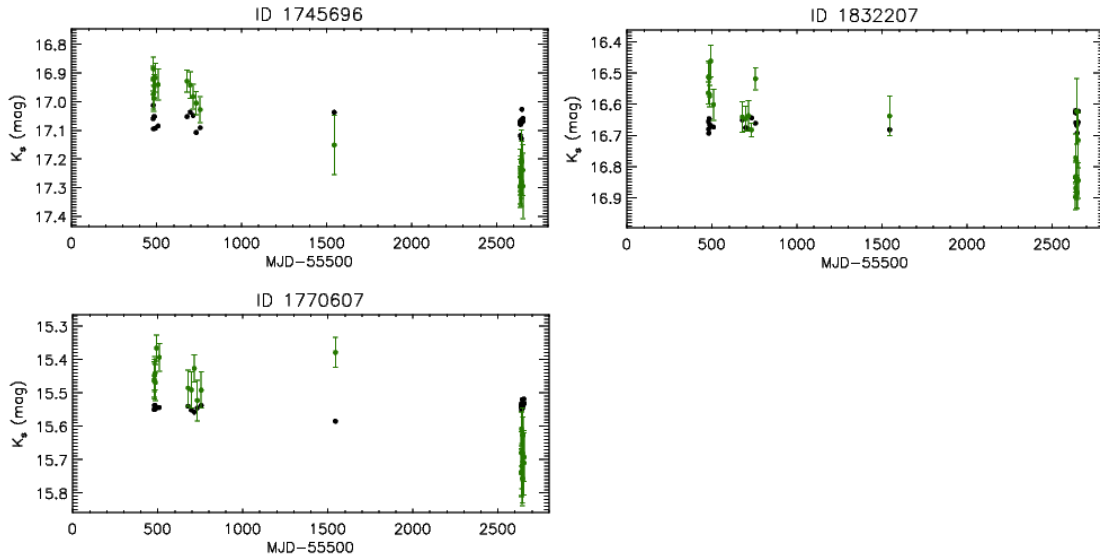


Figure 4.24: As Fig.4.23 but for stars classified as faders. More details in the main text.

the fading, then it would be more pronounced in the J -band.

In contrast to the eruptives, the faders show comparatively similar lightcurve morphologies (examples shown in Fig. 4.24). They all exhibit a slow fading, either observed throughout the entire monitoring time (top left panel), or starting at some later point during the observations (bottom left panel). In some cases we see some short term variability superimposed onto the long-term dimming trend (top right panel). This could hint at a combination of multiple physical processes, e.g. additional modulation due to star spots.

Overall, 10 YSOs are classified as faders. In two cases there is very little or no dimming in the J -band magnitudes, making an obscuration event very unlikely. One object experiences a significantly larger magnitude drop in the J -band ($\Delta J \approx 0.55$ mag, $\Delta K_s \approx 0.3$ mag), strongly supporting extinction as the cause of the fading. For all other faders extinction might play only a minor role, as the fading in the J -band is less pronounced than in the K_s -band (Sec. 4.6.4).

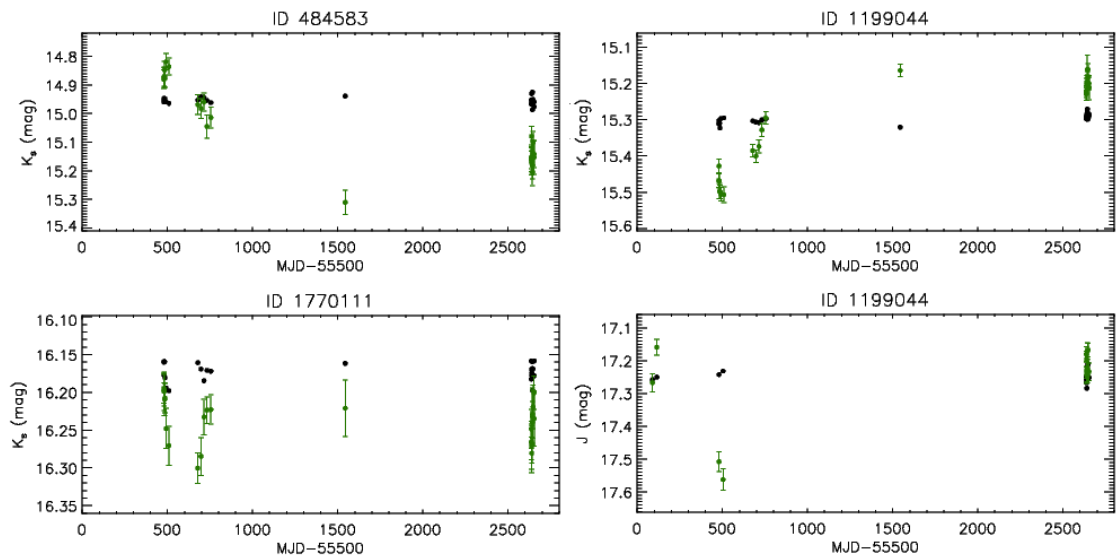


Figure 4.25: As Fig.4.23 but for stars classified as dippers. The lightcurve in the bottom right panel is from the same object as in the top right panel, just for the J -band.

4.6.1.3 Dipper

Dippers experience fading events followed by a return to their normal brightness. This class is generally associated with extinction events and they share some lightcurve morphologies with the fader class. If, for example, the brightening is not within the observation window, the object will usually be classified as a fader.

Some of the dippers have not yet returned to their presumably normal magnitudes by the end of the observation window (Fig. 4.25, top left panel); the brightness remains lower than in the early epochs. The bottom left panel shows an object with a relatively shallow dip ($\Delta K_s \approx 0.1$ mag) of ~ 250 days duration. We find four YSOs with this type of lightcurve. Another example is presented in the right panels. The K_s lightcurve has a similarly narrow dip (top panel), but we apparently missed the beginning of the dimming. In this case the J -band lightcurve is useful (bottom panel), since the first epochs are observed almost a year before any K_s epochs. They strongly suggest that the initial brightness is very similar to the final one. Another dipper is shown in Fig. 4.23

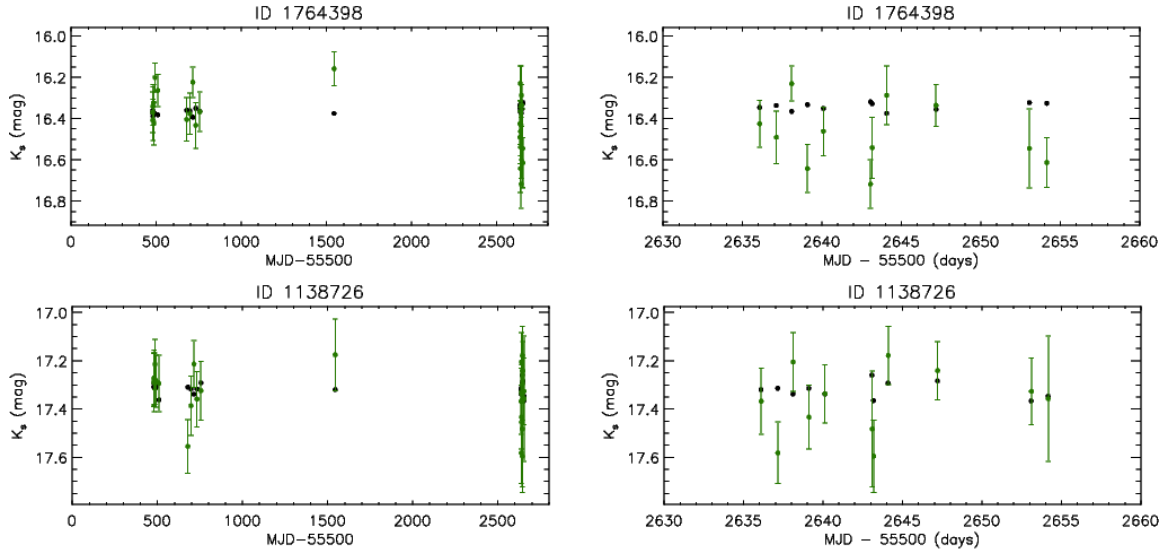


Figure 4.26: K_s lightcurves of two YSOs classified as STVs (left panels). The right panels show a zoom into the high cadence observations at the end of the observation window.

(bottom right panel), where the dip is preceded by an outburst. In total, we classify seven YSOs as dippers.

4.6.1.4 STV

This class comprises stars which show either periodic or aperiodic variations in their luminosity over timescales of < 100 days. This type of variability can be explained either by photospheric phenomena modulated by the rotation of the star (Wolk, Rice & Aspin 2013), by orbital variations in the disc extinction (Rice et al. 2015), or by variable accretion (Bouvier et al. 2003). As our sensitivity towards periodicity is low (Sec. 4.4.3) we do not claim the detection of periodic behaviour for any members of this class. Still, all YSO lightcurves of this class have a best-fit period of < 100 days, according to the LombScargle analysis.

Two examples are shown in Fig. 4.26, with the K_s lightcurve (left panels) and a zoom-in onto the high cadence epochs (right panels). No long-term luminosity trends

are apparent. Instead short-timescale variations dominate, considerably larger than the variations seen in the lightcurves of the comparison star. Eight YSOs are classified as STVs. They tend to display small amplitudes with five of them having $\Delta K_s < 0.3$ mag. Since most J lightcurves show similar amplitudes (for the STVs where we have reasonably sampled J lightcurves), changes in extinction seem unlikely. More probable are either stellar spots or moderate changes in the accretion rate.

4.6.1.5 Not classified

Three YSOs defy classification in any of the four classes above. In the left panels of Fig. 4.27 are two objects that share a very similar K_s lightcurve. They show some similarities to the STV-examples (Fig. 4.26). The LombScargle routine calculates as best fit periods 451 days and 618 days for the top and bottom lightcurve, respectively. Thus the short-timescale fluctuations are apparently less dominant than in the STV classified examples. Upon visual inspection the lightcurves seem to show low-amplitude, cyclic variations which are consistent with possible LPV-YSOs (see further discussion in Sec. 4.6.2).

An interesting (and in our sample) unique K_s lightcurve is shown in the top right panel. Two prominent and short dips of similar amplitude were detected, which suggests a possible eclipsing binary. Interestingly, the J lightcurve does not show these features: the second dip should have been visible in the J -band, since back-to-back observations of both filters were obtained. A visual inspection of the images did not reveal suspicious behaviour like for example intermittent artifacts. This is the only object for which we were unable to classify the lightcurve (so that it makes the only unclassified source in the tables later on).

4.6.2 YSO periodicity

The LombScargle analysis calculates for every lightcurve a best-fit period. Objects with a high likelihood of being periodic are usually identified by their small FAP, how-

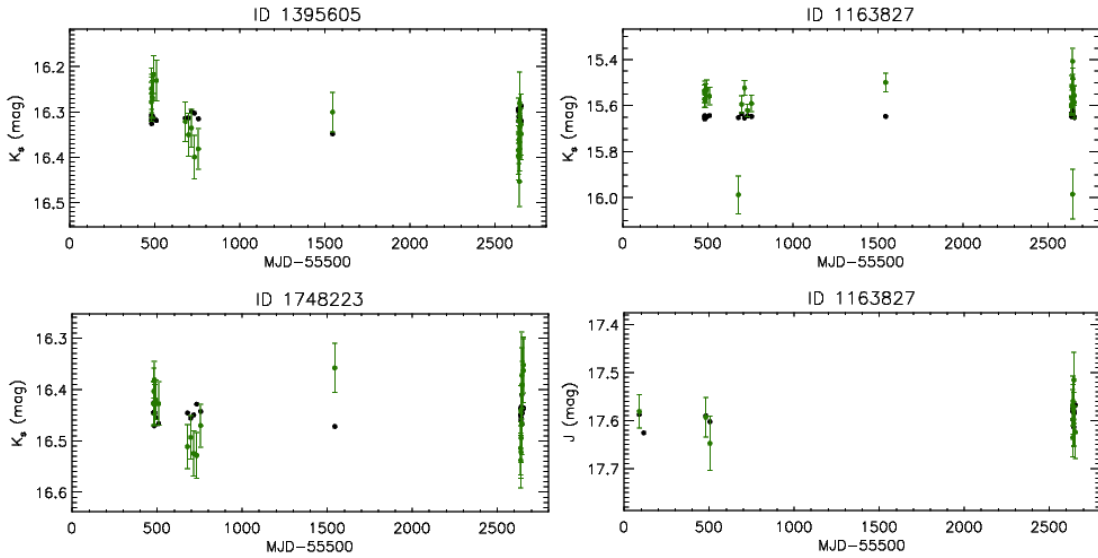


Figure 4.27: Lightcurves of the variable YSOs that are unclassified. The right panels show the K_s lightcurve (top) and J lightcurve (bottom) of the same star.

ever our tests with OGLE variables did not provide a reliable threshold (Sec. 4.4.3). Still, our OGLE analysis shows a relatively high success rate for periods in the 2 d–20 d range. Two YSO variables have a best-fit period in this range, both classified as STVs (Fig. 4.26). Their periods are 3.5 d (top panel) and 2.1 d (bottom panel). Figure 4.28 shows a zoom into the epochs from our high cadence observations, with the model provided by the LombScargle routine (left panels); the right panels show the corresponding folded lightcurves. The model matches the measurements with considerable scatter. Since our sensitivity is the highest in the 2 d – 20 d range, these two sources have tentative period detections in this range. The fact that only two such sources are found is broadly consistent with our YSO sample being very young. Periods in this range are often caused by rotational modulation, which is more readily observed in more evolved Class II or III objects (Contreras Peña et al. 2017b).

The majority of the YSO variables have a computed period > 100 days (30 out of 39), which would qualify them as LPV-YSOs. Such periods could arise from variable accretion modulated by a binary companion (Hodapp et al. 2012), or by obscura-

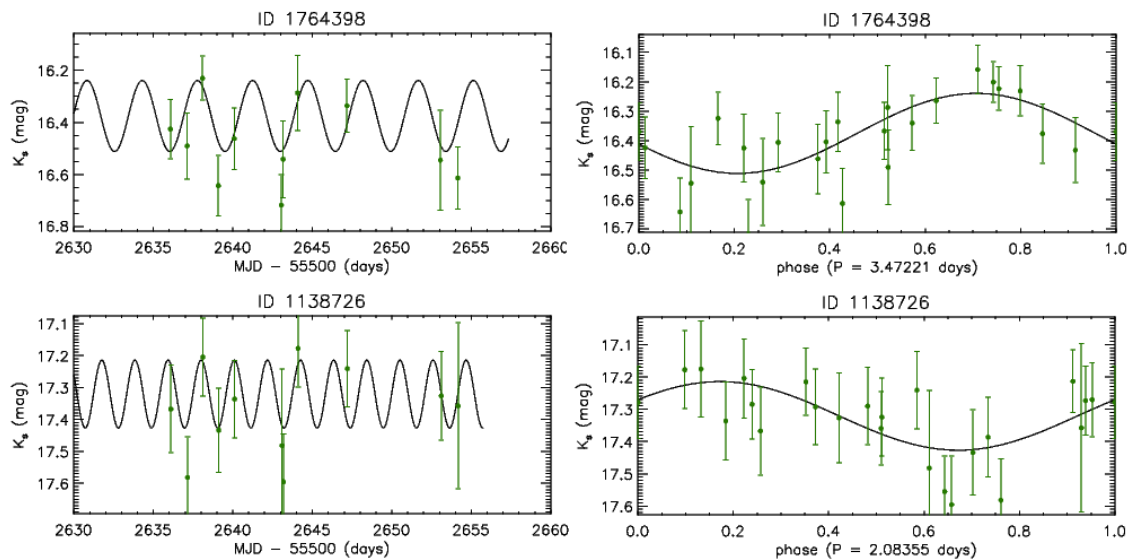


Figure 4.28: Zoomed in K_s lightcurves of two YSOs classified as STVs, with the Lomb-Scargle model of the calculated period overplotted (left panels). The right panels show the corresponding folded lightcurves.

tion due to a circumbinary disc (Contreras Peña et al. 2017b). Our inspection of the lightcurves does not support periodicity, with three possible exceptions. For the two non-classified YSOs shown in Fig. 4.27 (left panels) the lightcurves exhibit reasonably convincing periodicity; their lightcurves and folded lightcurves are shown in Fig. 4.29 (top two rows), exhibiting periods of 451 and 618 days. The sinusoidal models match the measurements reasonably well, but later epochs (MJD - 55500 \approx 2650 days) show a considerable scatter. The third example (bottom row) is a YSO identified as variable only in the J -band (the K_s -band magnitudes are brighter than our cutoff limit). This YSO is classified based on the J lightcurve as an eruptive. However, the K_s measurements can be fitted by a ~ 494 days period, strongly suggesting that this YSO might indeed be periodic. Consequently, the three stars shown in Fig. 4.29 are classified as LPV-YSOs. The LPV-YSO previously classified as eruptive still also keeps its original classification. In summary, at most five YSOs could be tentatively classified as periodic: two with $2 < P < 20$ days and three with $P > 100$ days.

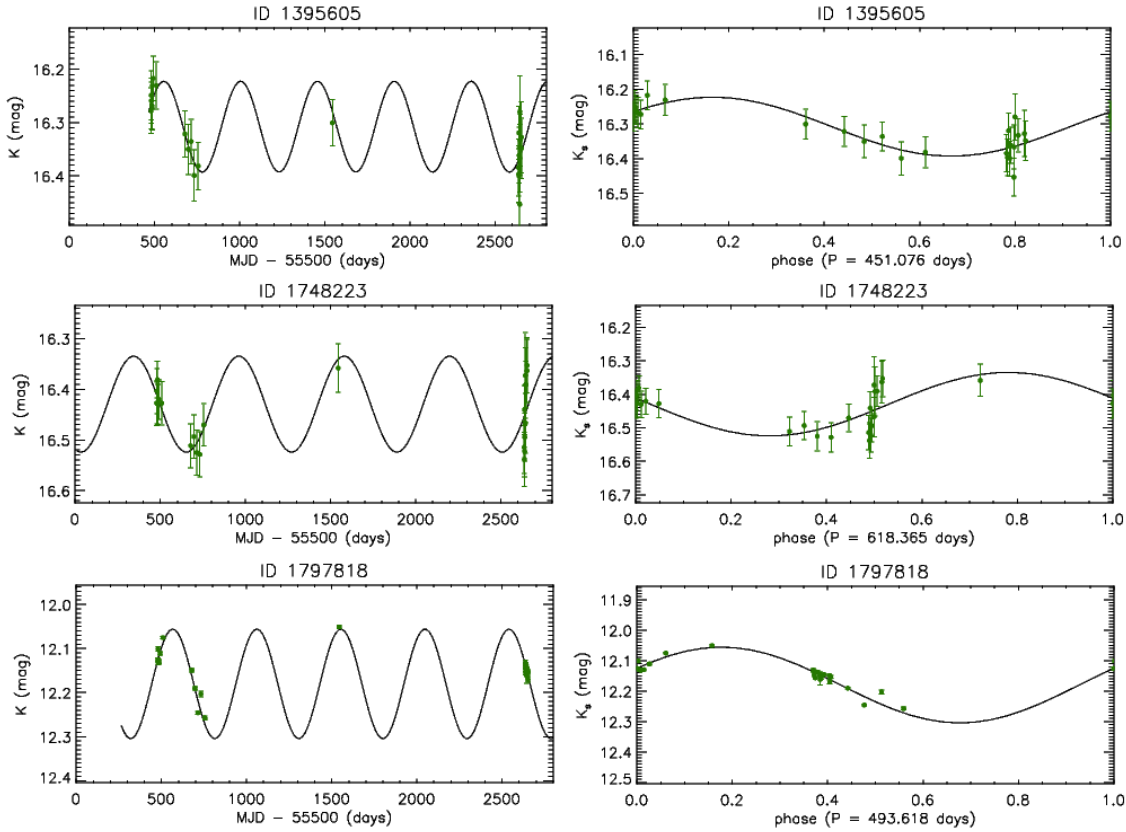


Figure 4.29: **Left panels:** K_s lightcurves of possible LPV-YSOs with their models overplotted. **Right panels:** Corresponding folded lightcurves.

4.6.3 Properties of the variable YSOs

Figure 4.30 shows the location of the YSO variables in a CMD (left panel) and a CCD (right panel). Variability seems more prevalent amongst the brighter YSOs, however this is likely a selection effect since larger amplitudes are needed for faint stars to be identified as variable. The overall variability fraction is $\sim 22.5\%$ (39 out of 173), increasing for $K_s < 17$ mag to $\sim 32.7\%$ (34 out of 104). For YSOs with $K_s < 16$ mag (the regime where we achieve the best sensitivity, see Sec. 4.4.2) the fraction is $\sim 36.7\%$ (18 out of 49). NIR-variability is more common amongst very red sources. Slightly over half of the YSOs with $Y - K_s > 3$ mag (16 out of 30) show variability, compared

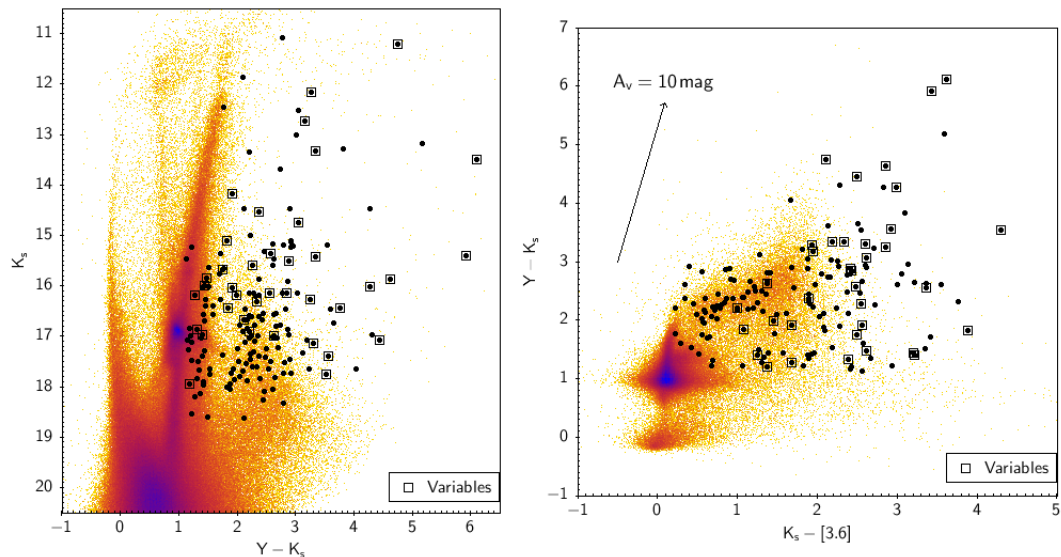


Figure 4.30: **Left panel:** CMD with the YSO sample (circles), and the variable YSOs (squares). **Right panel:** As on the left, but as a CCD.

to only $\sim 16\%$ (23 out of 143) for $Y - K_s < 3$ mag. Assuming that the redder stars are younger, we see a trend towards more widespread variability for less evolved sources. However, a selection effect could be at play since redder objects tend to be brighter, making it more likely to identify variability.

The variable YSOs exhibit considerable IR-excesses (Fig. 4.30, right panel). The mean colours for the entire sample of 173 YSOs are $\langle Y - K_s \rangle = 2.43 \pm 0.06$ mag and $\langle K_s - [3.6] \rangle = 1.88 \pm 0.10$ mag. For the YSO variables the corresponding colours are $\langle Y - K_s \rangle_{\text{var}} = 2.82 \pm 0.07$ mag and $\langle K_s - [3.6] \rangle_{\text{var}} = 2.46 \pm 0.08$ mag. These values for the YSO variables cannot be explained by a higher reddening alone. This indicates that the YSO variables exhibit on average a larger IR-excess, which supports the fact that they tend to be younger.

Out of the 39 variables, 31 are found to be variable only in the K_s -band, while six fulfilled the criteria in both bands. Two YSO variables are identified solely based on J -band data; however, for these stars only the J -band data was examined since they are brighter than the bright cutoff limit in the K_s -band. Both stars showed variations

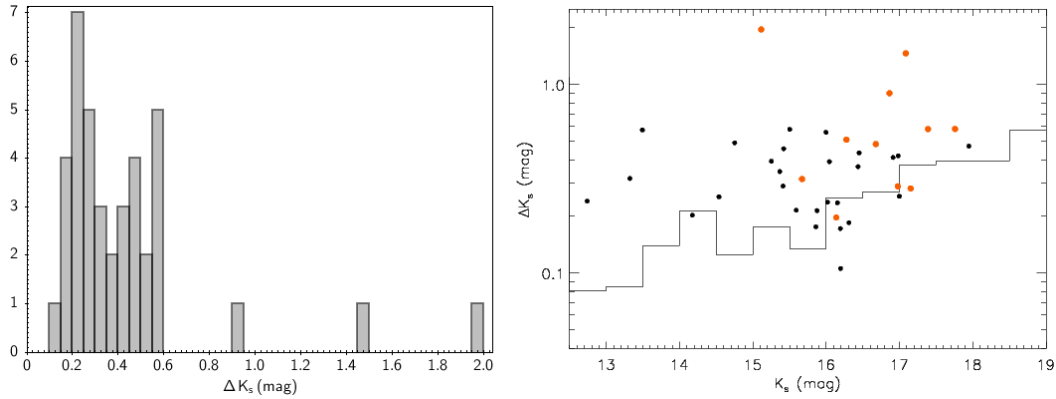


Figure 4.31: **Left panel:** Distribution of the K_s -amplitudes (ΔK_s) for the variable YSOs. **Right panel:** K_s vs. ΔK_s plot for the variable YSOs (solid circles). Objects classified as eruptives are highlighted in red. The histogram shows the median- ΔK_s for all detected variables in magnitude bins of 0.5 mag width.

in the K_s -band that are larger than expected from the photometric error alone. The difference between the bands regarding variability detection is caused by the fact that the YSOs are considerably fainter in J . Out of the 28 YSOs with $13 \text{ mag} < J < 17 \text{ mag}$, 5 are variable in the J -band ($\sim 18\%$). For the K_s -band there are 31 variables out of 97 YSOs ($\sim 32\%$) for $13 \text{ mag} < K_s < 17 \text{ mag}$. Assuming that the variability fraction in the J -band is the same as in the K_s -band, one would expect on average 8.9 variables in a sample of 28 YSOs. The probability for finding five variables can then be calculated using Poisson statistics.

$$P(k) = \frac{\lambda^k e^{-\lambda}}{k!} \quad (4.2)$$

Using $\lambda = 8.9$ and $k = 5$ gives a probability of 0.063. For $k \leq 5$ the probability is $P(k \leq 5) \approx 0.122$, which shows that an apparently (!) lower fraction is not unlikely. Furthermore, the smaller number of epochs in the J -band reduces the sensitivity towards certain types of variables.

The YSO amplitudes are mostly in the range $0.1 \text{ mag} < \Delta K_s < 0.6 \text{ mag}$ as shown in Fig. 4.31 (left panel). Note, that the observed amplitudes are lower limits, since we might have missed the true maximum and minimum of the lightcurves. Only two of our

Table 4.3: Number of variables, mean amplitudes, the standard deviations, and the median amplitudes for all classes. The sum is 41 instead of 39 because one star was classified as eruptive and dipper, and another as eruptive and LPV-YSO.

	N	mean(ΔK_s) [mag]	SD(ΔK_s) [mag]	median(ΔK_s) [mag]
Eruptives	12	0.67	0.51	0.51
Faders	10	0.35	0.12	0.39
Dippers	7	0.46	0.43	0.35
STVs	8	0.32	0.13	0.29
LPV-YSO	3	0.21	0.02	0.21
unclassified	1	–	–	–

variables have $\Delta K_s > 1$ mag. Nevertheless, YSOs display above average amplitudes when compared to the total sample of 3817 variables. Figure 4.31 (right panel) shows K_s vs. ΔK_s for both samples. The histogram represents the median- ΔK_s for the total variable sample in 0.5 mag bins. Most YSO variables (30 out of 39) are located above the histogram bins, indicating that YSO variability is characterised by larger than average amplitudes. For the Milky Way this is also the case: $\sim 50\%$ of all variables with $\Delta K_s > 1$ mag were likely YSOs (Contreras Peña et al. 2017b).

Faders and STVs show similar mean amplitudes with a relatively low scatter (Table 4.3), while for the dippers and eruptives a significantly larger scatter is observed. Eruptives display the largest mean amplitude and the five highest amplitude YSOs belong to this class. The three LPV-YSOs show all similarly low amplitudes.

Out of the 2521 stars identified as variable in the K_s -band (Sec. 4.3), we find 40 high-reliability variables with $\Delta K_s > 1$ mag. Of these 40 sources, 25 are broadly associated with the PMS contours (see Sec. 3.5.1.1 and Fig. 4.32) for known star forming regions. Two were included in our sample of 39 YSOs and are classified as eruptives. The remainder of the sources either have no previous *Spitzer* classification (12 objects), or have no *Spitzer* point-source counterpart (9 objects). A further two sources have SEDs not well-fit by YSO models according to Carlson et al. (2012). Therefore, most sources may be YSOs but were not included in our high-reliability YSO sample. Thus

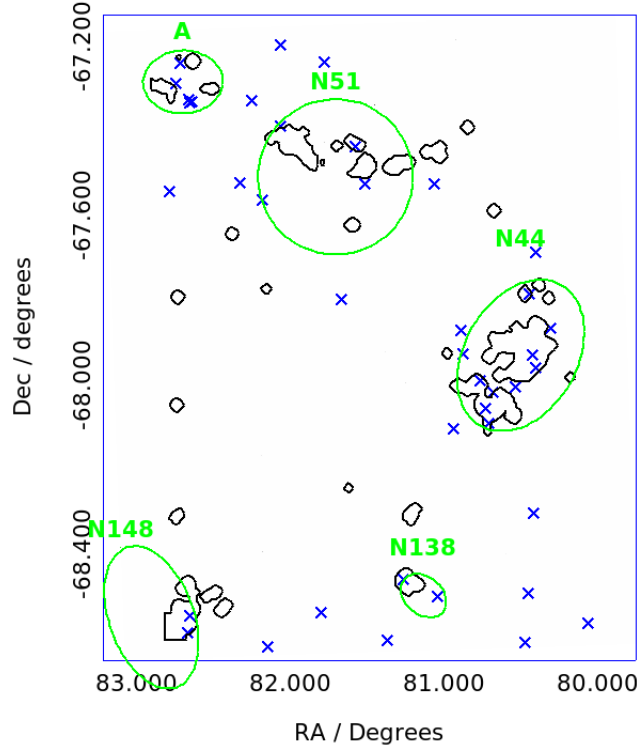


Figure 4.32: Spatial distribution of the 40 high-amplitude variables ($\Delta K_s > 1$ mag; crosses). The labelled blue ellipses show star forming complexes, the black contours indicate areas with significant PMS populations (see Fig. 3.9). There is a tendency for the high-amplitude variables to be associated with known star forming regions.

we can speculate that large amplitude variables, characterised by $\Delta K_s > 1$ mag, could well be primarily associated with YSOs, similar to what is seen in the Galaxy (Contreras Peña et al. 2017b). Note however, that their sample consisted mostly of low to intermediate mass YSOs which were typically undetected in the Y or even the J band. Our high-amplitude variables display magnitudes similar to the YSOs from Carlson et al. (2012), indicating masses of $\gtrsim 3 M_\odot$.

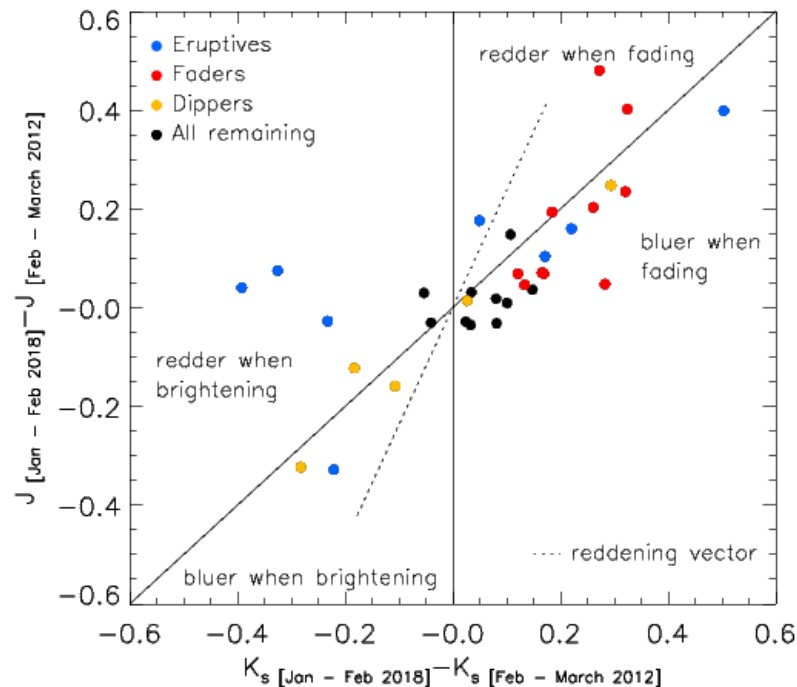


Figure 4.33: Amplitudes for the J and K_s -band, using the magnitude averages for the time-periods as specified in the axis-labels. The circles are colour-coded based on the lightcurve classification of the corresponding YSO.

4.6.4 Long-term variability and colour analysis

We investigate the long-term behaviour of the YSO variables by calculating the difference between the mean magnitudes from two time-periods. The first period from February and March 2012, contains two J -epochs and seven K_s -epochs. The second period includes all observations from our open time program (January – February 2018) and contains 11 epochs in both filters (Tab. A.1 and A.2). While two earlier J -epochs are available (from early 2011), they have no counterpart in the K_s -band.

Figure 4.33 shows the differences in magnitude for these two periods in both bands. Since most sources are located in the top-right and the bottom-left quadrant, there is a generally positive correlation between the J and the K_s -band. For objects with datapoints close to the 1:1 diagonal, the variability is basically colour-less. Objects

with extinction-related variability should be close to the dotted line that shows the reddening vector. In this regime a variable star gets redder when fading and bluer when brightening. The YSO variables are mostly concentrated near the 1:1 diagonal, with only few being in proximity of the reddening line. This apparently indicates that for most of our variables extinction is not the main cause of the observed variability. However, a possible explanation is wavelength-independent, grey extinction caused by large (compared to the wavelength) dust grains. Grey extinction was observed for example in the 30 Doradus complex in the LMC (De Marchi et al. 2016). Interestingly, all but two faders seem consistent with grey extinction related variability. One is close to the reddening line, indicative of variability associated with standard extinction. The other fader gets considerably bluer when fading. Considering that we observed three eruptives which reddened significantly while brightening, this fader might be an eruptive returning to a quiescent state. This colour-behaviour opposite to the common reddening laws is often seen for variables for which unsteady accretion (Poppenhaeger et al. 2015) or changes in the disc geometry (Rice et al. 2015) are the main physical processes driving the observed variations. The other eruptives exhibit either only small colour changes or get redder when fading. Hence, their variability seems to originate from changes in the line-of-sight extinction. Dippers are all distributed closely around the 1:1 diagonal, showing a negligible colour change hinting at grey extinction as the possible cause. For the STVs, LPV-YSOs, and the unclassified sources we generally do not find relevant long-term changes in their luminosity.

4.6.5 Comparison to Galactic studies

Galactic variability studies of massive YSOs in the NIR show a significant spread in variability fraction ranging from values similar to ours ($\sim 26\%$ in Teixeira et al. 2018) to $> 50\%$ (Borissova et al. 2016), although the latter study likely also included less massive objects. Many non-physical factors influence this fraction, such as total time-baseline, cadence, sensitivity to small amplitudes, or the criteria for classification as variable. Nevertheless, it is apparent that NIR-variability is a common feature among

Table 4.4: Numbers of YSO variables of a given classification in Contreras Peña et al. (2017b) and Teixeira et al. (2018), abbreviated as CP17 and T18, respectively.

	CP17	T18	This work
Eruptives	106	41	12
Faders	39	18	10
Dippers	45	20	7
STVs	162	49	8
LPV-YSOs	65	62	3
Eclipsing binaries	24	0	0
no class	0	0	1
total	441	190	41

YSOs also in the LMC.

Table 4.4 shows how many variables belong to a given class for two Galactic YSO-studies (Contreras Peña et al. 2017b; Teixeira et al. 2018) and for this work. Both Galactic studies use NIR-data from the VISTA Variables in The Via Lactea (VVV) public survey with an observing window spanning five years, which is similar to our total time-baseline of ~ 6 years. Eruptives are generally the most common class amongst the aperiodic classes (eruptives, faders, dippers), and eruptive behaviour is seen in roughly one quarter of the YSO sample for all three studies. Noticeable is the high number of STVs in both Galactic studies, while their fraction is smaller in our work. This might be connected to our relative insensitivity towards periodic variability, likely due to the fact that the number of epochs is small compared to the VVV data (~ 50 epochs in Contreras Peña et al. 2017b). Note however that the STV class can also contain aperiodic stars. The LPV-YSO fraction is also significantly smaller in this work, due to the low sensitivity towards long periods.

The distribution of the variable YSO amplitudes (Fig. 4.31) is consistent with Borissova et al. (2016), where most variables (21 out of 27) have amplitudes between 0.2 mag and 0.5 mag, with the other six exhibiting $\Delta K_s > 0.5$ mag. This is a ratio very similar to our sample; we report a $\Delta K_s > 0.5$ mag for 10 out of 39 YSOs. In contrast, Teixeira et al. (2018) finds that a majority of their YSO variables have an

K_s -amplitude larger than 0.5 mag (123 of 190). We performed the Kolmogorov-Smirnov test and calculated the probability that their amplitude distribution and ours are drawn from the same distribution (null-hypothesis probability), which resulted in 1.34×10^{-7} . Hence, the difference is highly significant. We note that 54 of their YSO variables are coincident with clumps detected at $870 \mu m$. Hence, they are likely extremely young which increases the probability of high-amplitude variability (Contreras Peña et al. 2014). Indeed, *all* 54 members of this subsample show a $\Delta K_s > 0.5$ mag. Removing them and recalculating the null-hypothesis probability for the remaining 136 YSOs gives 0.91×10^{-3} . Hence, there is a statistically significant difference between the amplitude distributions, which might be due to environmental effects like metallicity or due to population effects (e.g differences in evolutionary stage or masses). A meaningful comparison with the amplitude distribution from Contreras Peña et al. (2017b) cannot be made since they focus entirely on high-amplitude variables ($\Delta K_s > 1$ mag).

Since massive Magellanic YSOs exhibit larger mass accretion rates compared to Galactic YSOs (see Sec. 1.3.2), one could have expected larger amplitudes for YSO variables in our sample. The present work does not support this view. The amplitudes are either found to be similar (compared to Borissova et al. 2016) or smaller (compared to Teixeira et al. 2018). It could be simply a population effect, with our YSO sample being slightly more evolved, which would tend to reduce the accretion rates. The higher gas-to-dust ratio in the LMC might also contribute to keeping the amplitudes small. For the LMC this ratio is ~ 3 times larger than in the Galaxy (Welty, Xue & Wong 2012), hence column density changes due to inhomogeneities crossing the line-of-sight lead to a correspondingly smaller change in extinction. Consequently, for YSOs where extinction plays any role in causing photometric variability, a lower metallicity might actually have the effect of reducing the amplitudes.

4.7 Summary and conclusions

We use NIR data from the VMC survey combined with observations from our open time program to investigate the variability of 173 high-reliability YSOs in the LMC. These observations provide 15 J -epochs and 24 K_s -epochs, covering a time-span of ~ 6 years. Photometric variability was identified by applying a χ^2 -analysis on the pawprint photometry catalogues for both bands separately. The thresholds above which a star is considered variable are defined based on distributions of the χ^2 -values, which depend on filter, pawprint, and magnitude-range. The YSO sample is selected from three *Spitzer* studies. After spatially correlating these catalogues with the VMC deep catalogue, we apply additional steps to remove possible contaminants, which includes colour-cuts combining *Spitzer*- and VISTA-filters, and visual examination of the sources. The main results of our variability analysis are as follows:

- Based on comparing all stars we identify as variable with the OGLE sample, the minimum amplitude required to reliably identify variability in our dataset is ~ 0.1 mag for $J \lesssim 17$ mag and $K_s \lesssim 16$ mag. For fainter objects the minimum amplitudes increase due to the growing photometric errors and reach ~ 0.5 mag in both bands for $J \approx 19$ mag and $K_s \approx 18$ mag.
- Of the 1592 LPVs, 654 RR Lyrae, and 43 Cepheids from the OGLE sample in our study area we identify 109 LPVs, 302 RR Lyrae, and 34 Cepheids as variable. The low fraction of identified LPVs is a result of predominantly small amplitudes (< 0.1 mag). For Cepheids we have a high success rate, since they are bright ($13 \text{ mag} \lesssim K_s \lesssim 16 \text{ mag}$) and exhibit comparatively large amplitudes. RR Lyrae stars have a reduced success rate due to their faintness.
- Using the LombScargle period analysis we tested whether the OGLE periods can be recovered from our NIR lightcurves. Within the range $2 \text{ d} < P < 20 \text{ d}$ $\sim 79\%$ of the OGLE periods are recovered (15 out of 19). For periods outside of this range the success rate is only $\sim 31\%$ (21 out of 68). Our cadence is not

suited to identify $P < 2$ d.

- Out of the 173 YSOs, 39 are identified as variable using the χ^2 -test ($\sim 22.5\%$). This fraction increases to $\sim 36.7\%$ for bright YSOs ($K_s < 16$ mag), the regime in which we achieve the best sensitivity. This fraction is within the broad range found in Galactic studies, albeit towards the lower end. Notably, the variability fraction increases substantially for very red sources. For $Y - K_s > 3$ mag, $\sim 53\%$ of the YSOs (16 out of 30) show variability, but we cannot exclude selection effects.
- In the $K_s - [3.6]$ vs. $Y - K_s$ CCD the variable YSOs exhibit, on average, a larger IR-excess than the overall YSO sample. This suggests that the variables tend to have more significant discs or envelopes, i.e. they tend to be at an earlier evolutionary stage. Consequently, variability appears to be more common for least evolved YSOs.
- All but three variable YSOs have moderate amplitudes in the range $0.1 \text{ mag} < \Delta K_s < 0.6 \text{ mag}$. Compared to the amplitudes of all identified variables (i.e. including non-YSOs), YSOs tend to show above average amplitudes. 30 variable YSOs are above the median amplitudes of the entire variable population. This implies that YSOs are dominant in samples of high amplitude variables in agreement with Galactic studies (Contreras Peña et al. 2017b).
- The YSO variables are classified based on the appearance of their K_s -band lightcurves. Our sample includes: 12 eruptives, 10 faders, seven dippers, eight STVs, three LPV-YSOs, and one unclassified object. Two YSOs are members of two classes (eruptive/dipper and dipper/LPV-YSO) as they show signatures of both classes. Eruptives tend to have large amplitudes compared to the other classes. The five YSOs with the highest amplitudes are all eruptives.
- Long-term variability and colour changes are investigated by comparing the mean magnitudes in both bands for the early epochs (February and March

2012), and for the most recent epochs (January and February 2018). In general, the J and K_s variability correlate. Most YSO variables have either negligible colour changes or get bluer when fading. The results seem consistent with variability caused by unsteady accretion and/or variable grey extinction.

- We found two YSOs with periods in the range $2 \text{ d} < P < 20 \text{ d}$ (where the sensitivity of our method is best). This suggests that periodicity in this range is rare for our sample, consistent with what is expected for an early stage YSO population. The lightcurves of three additional YSOs indicate a possible periodicity with longer periods of $\sim 450 \text{ d}$, $\sim 490 \text{ d}$, and $\sim 620 \text{ d}$.
- In total 40 stars from the entire sample of variables detected in the K_s -band exhibit $\Delta K_s > 1 \text{ mag}$. While only two of them are amongst the analysed YSO variables, 25 are broadly associated with star forming complexes. Therefore, many of them might be YSOs.
- NIR-variability is a common feature amongst YSOs in the LMC, occurring with similar frequency as in Galactic samples. The fractions of aperiodic classes (faders, dippers, eruptives) are broadly consistent with results from Galactic studies. However, we report slightly fewer STVs and much fewer LPV-YSOs, likely because of the low sensitivity especially towards long periods. The amplitude distribution is either similar or tends towards smaller values, depending on which Galactic study our sample is compared to. It is statistically significant and could be due to environmental differences like metallicity, but we cannot exclude possible differences between the YSO populations.

5 Conclusions, summary and prospects

In this thesis, the first large-scale study of intermediate and low mass PMS populations down to $\sim 1 M_{\odot}$ in the LMC was presented (Chap. 3). An area of $\sim 1.2 \text{ kpc}^2$ was examined via statistical analysis of star colours and magnitudes using YJK_s PSF photometric data from the VMC survey (Chap. 2). Additional proprietary NIR-data was combined with the VMC observations to conduct the first systematic variability study of massive YSOs in the LMC (Chap. 4). 173 high-reliability *Spitzer*-identified massive YSOs were selected and their lightcurves analysed regarding shape, amplitude and periodicity.

In this section I will discuss the results of this thesis in the context of the goals outlined in the introduction (Chap. 1). This is followed by an outlook into possible future studies.

5.1 PMS populations

The statistical analysis of magnitude and colour distributions in K_s vs. $(Y - K_s)$ CMDs revealed ~ 2260 PMS stars (a conservative lower limit) with $1 \lesssim M_*/M_{\odot} \lesssim 4$. These sources mostly concentrate in previously known large star forming complexes. Some PMS density structures lack young massive stars and were therefore missed by previous studies focusing on OB-associations. This shows that the study of low/intermediate PMS stars is necessary to quantify the full extent of ongoing and recent star formation.

The number of stars in the PMS structures showed a power-law distribution which is expected for scale-free processes (Elmegreen & Falgarone 1996). Furthermore, the large structures are hierarchically organised and consist of smaller and higher density subgroups. VMC studies investigating young UMS stars in two other tiles of the LMC found power-law size and mass distributions (Sun et al. 2017b; Sun et al. 2017a). A very similar UMS study in the SMC reported essentially the same results (Sun et al. 2018). The development of a hierarchy with large congregations housing denser substructures

seems independent of environment or metallicity. In NGC 1566, a large spiral galaxy with near solar metallicity (Wofford et al. 2016), a hierarchical morphology was also observed (Gouliermis et al. 2017). The identified young stellar conglomerations exhibit a size distribution that can be approximated by a power-law over a wide range of scales, indicative of scale-free processes. In the different environment provided by NGC 6822, an irregular dwarf galaxy with a low metallicity ($Z \approx 0.2 Z_{\odot}$; Skillman, Terlevich & Melnick 1989), the structural behaviour of the detected stellar systems leads to the same conclusions (Gouliermis et al. 2010). In both galaxies the studies only took massive stars into account (NGC 1566: $\gtrsim 15 M_{\odot}$, NGC 6822: $\gtrsim 5 M_{\odot}$) due to the larger distances compared to the LMC. It is reasonable to expect that the results of these studies would not have changed by taking PMS stars into account, since all stars originate from molecular clouds which imprint their gas distribution onto the young clusters and associations.

The PMS populations are located along ridges of bright FIR ($70 - 500 \mu\text{m}$) dust emission. We find a correlation between dust emission and number of young stars for regions that house both PMS and massive stars. This correlation seems to be the strongest for $70 \mu\text{m}$ (see Fig. 3.15, right panels). Indeed, Li et al. (2010) proposed the use of $70 \mu\text{m}$ emission as an SFR indicator. However, we do not find a correlation between dust emission and number of PMS stars for regions lacking massive stars. This is probably because massive stars dominate the radiative output, and are therefore mostly responsible for powering the reradiated FIR emission. Hence our observed correlation breaks down, once no or only few massive stars are present in a region. PMS-only regions are also more affected by the incompleteness of the VMC data, so any possible correlation with the FIR emission is more difficult to observe. We also note that Li et al. (2010) reported a larger scatter in the SFR-to- $70 \mu\text{m}$ correlation for $Z \lesssim 0.5 Z_{\odot}$. This is likely caused by the clumpiness and low dust abundance of the ISM in low-metallicity environments (Cormier et al. 2012). The fraction of unattenuated starlight – which consequently does not contribute to the FIR dust emission – is then likely to depend strongly on the geometry and direction of observations, increasing the scatter. These effects could mask our ability to detect a correlation between dust

emission and number of young stars, which should be especially significant in the less massive PMS-only regions.

5.2 YSO variability

Using χ^2 -analysis on a sample of 173 high-reliability *Spitzer* YSOs compiled from the literature, photometric variability was revealed for 39 of them ($\sim 22.5\%$). Considering that for the entire stellar sample covered by the pawprint catalogues 3817 of the 362 425 stars are found to be variable ($\sim 1.1\%$), it becomes clear that variability in LMC YSOs is more common than in a random stellar sample. The same results have been consistently found in Galactic studies (e.g. Carpenter, Hillenbrand & Skrutskie 2001; Wolk, Rice & Aspin 2013; Borissova et al. 2016; Teixeira et al. 2018), where the fraction of variables is broadly similar to our results. The variability for the 39 YSOs was mostly identified in the K_s -band, which can probably be attributed to the higher luminosities compared to the also analysed J -band. Consequently, they were classified based on the K_s -lightcurve shape, using the classification scheme introduced in Contreras Peña et al. (2017b). We identified in 12 eruptives, 10 faders, seven dippers, eight STVs, three LPV-YSOs and one unclassified YSO. Two YSOs are classified as members of two classes.

The observed amplitudes, defined as the difference between the brightest and the faintest observed magnitude, are moderate and all but three are within $0.1 \text{ mag} < \Delta K_s < 0.6 \text{ mag}$, with two YSOs exhibiting $\Delta K_s > 1 \text{ mag}$. The comparison of the amplitude distribution with Galactic studies focusing on massive YSOs is inconclusive. Borissova et al. (2016) has a similar amplitude distribution, however the study from Teixeira et al. (2018) finds larger amplitudes. This difference is statistically significant as the analysis in Sec. 4.6.5 showed. Assuming the low metallicity environment of the LMC as the only cause for deviations in the amplitude distributions, there are several mechanisms that can shift the distributions towards either smaller or larger values.

The larger mass-accretion rates found in the LMC compared to similar Galactic

stars (see Sec. 1.3.2) could be suggestive of larger amplitudes, which were not observed in this work. This is not necessarily in conflict with higher mass-accretion rates, as it is unsteady accretion that leads to photometric variability and not steady accretion rate. Still, a larger mass influx implies more massive discs which are more prone to gravitational instabilities (Evans et al. 2015), thereby leading to stronger variations in the accretion rate. However, this can only affect YSOs where unsteady accretion is the dominant process causing photometric variability. A small fraction of such YSOs in our sample would therefore limit the impact on the amplitude distribution. Another possible influence on the amplitude distribution is associated with the disc-lifetimes. As discussed in Sec. 1.3.2 some studies suggest shorter disc-lifetimes at low metallicities. In this case, more variables with smaller amplitudes are expected compared to Galactic samples of similar age. However, these variables would also tend to be periodic as their variability is predominantly caused by rotational modulation of photospheric phenomena. Moreover, the periods would then be in the 2 d–20 d range where we have the best sensitivity towards periodicity (Sec. 4.4.3). Since we only found two variables in this range the short lifetime scenario does not seem convincing. A change towards smaller amplitudes can also be caused by the larger gas-to-dust ratios in low metallicity environments, which tends to reduce the changes in extinction when inhomogeneities cross the line-of-sight. The colour analysis in Sec. 4.6.4 revealed that the colour shifts of most YSO variables do not follow typical reddening laws. Instead they exhibit colour-less variability or get bluer when fading. Since colour-less variability can be caused by grey extinction, the larger gas-to-dust ratio in the LMC could indeed have shifted the amplitude distribution of our YSO sample towards smaller values.

Lastly, the fraction of periodic variables (5 out of 39, $\sim 13\%$) is significantly lower than found in Galactic studies (Table 4.4). However, this is likely related to our overall poor sensitivity towards periodicity. Metallicity might play some role in this, but we cannot prove or disprove it with the results in this work.

5.3 Future prospects

The algorithm developed for the PMS identification and classification in Chap. 3 can be used for other LMC tiles without significant modifications. This will give a galaxy-wide overview of the distribution of young stellar populations including the PMS population. However, we expect that the lower mass limit of $\sim 1 - 2 M_{\odot}$ for Tile LMC_7.5 might change for other tiles. The catalogue data at the corresponding magnitudes suffers from low completeness and is very sensitive to crowding. Hence, at tiles covering the densely populated bar region the lower mass limit might be higher.

Applying the Chap. 3 approach to the SMC is also viable. However, just accounting for the larger distance modulus (by about 0.5 mag) is probably not sufficient, i.e. more modifications are necessary. In contrast to the LMC, which is viewed close to face-on, the SMC has a complicated geometry and shows a significant line-of-sight depth. It is dominated by a bar-like structure in NE–SW direction and exhibits a wing extending to the East (de Grijs & Bono 2015). Using VMC data Rubele et al. (2015) derived a mean inclination of 39° , with the easternmost part being ~ 8 kpc closer to us than regions in the southwest (~ 54 kpc vs. ~ 62 kpc). Consequently, the distance modulus variations are larger than for the LMC, although they are still at a moderate 0.3 mag. In particular, this might affect our reddening correction procedure which uses the colour-distribution of RC stars in the RC box (Fig. 3.2, top panels). A simple widening of the RC box to incorporate a larger K_s -magnitude range would increase contamination by non-RC sources. A solution might be a procedure that first determines the location of the RC in the CMD. Note that some few tiles in the eastern parts of the SMC showed a “double-RC”, attributed to a tidally stripped population at a smaller distance (Subramanian et al. 2017). These tiles might require additional work, possibly in the form of a separate treatment for both RCs. After implementing and testing of the modifications, the SMC PMS populations could be identified and classified in the same way as for the LMC.

Besides the VMC data, the Survey of the MAgellanic Stellar History (SMASH; Nidever et al. 2017) could provide an interesting complement to study young stellar

populations in the MCs. SMASH maps an area of 480 deg^2 containing the LMC, SMC, and their stellar halos using *ugriz* bands, i.e. a wavelength range between ~ 350 and 950 nm . The reached 5σ depths are 23.9, 24.8, 24.5, 24.2, and 23.5 mag with a seeing of 1.22, 1.13, 1.01, 0.95, and 0.90 arcsec (*ugriz*). This would be sufficient to identify PMS stars down to $\sim 0.7 M_{\odot}$ for an age of 1 Myr ($\sim 1.2 M_{\odot}$ for 10 Myr), which is even deeper than what was achieved in this work. Note however, that the *ugriz* bands suffer from higher extinction compared to the NIR bands of the VMC. It will depend on the line of sight extinction towards the young population if there is indeed a depth advantage. In any case, SMASH covers areas not observed by the VMC, therefore a study of PMS populations using SMASH could extend beyond the boundaries of the VMC survey. It would also be interesting to combine the VMC & SMASH catalogues to develop a PMS-identification strategy that takes advantage of the extended photometric baseline.

5.4 Beyond the LMC

The ongoing wide-field study of resolved star formation and young stellar populations in the LMC provides a valuable insight into star forming conditions typical for the early universe. However, it still covers only one type of environment regarding metallicity and galaxy-type. Also, the LMC is a special case of an interacting, irregular dwarf galaxy, therefore it might not be representative of its type. It is therefore desirable to extend resolved studies beyond the LMC. With the advent of next generation observatories it will become feasible to conduct such studies for Local Group galaxies down to the intermediate stellar mass range.

The James Webb Space Telescope (JWST; Gardner et al. 2006) with its focus on IR wavelengths ($0.6 - 28.5 \mu\text{m}$) is perfectly suited to uncover embedded young stellar populations. It is equipped with the NIR imager NIRcam (Horner & Rieke 2004), operating at $0.6 - 5.0 \mu\text{m}$. Thus it covers the VMC wavelength regime and the two bluest bands available to *Spitzer*, but at a significantly higher resolution. NIRcams pixel-scale is either $\sim 0.031''$ for the short wavelength channel ($0.6 - 2.3 \mu\text{m}$) or $\sim 0.063''$ for the

long wavelength channel ($2.4\text{--}5.0\ \mu\text{m}$). Its field-of-view is only 2.2×2.2 arcmin, which is much smaller than one tile. However, at the distances of Andromeda (M31; ~ 770 kpc; Karachentsev et al. 2004) and Triangulum (M33; ~ 840 kpc; Madore & Freedman 1991), the two other large spirals in the Local Group, this corresponds to $\sim 500\times 500$ pc. This is enough to cover large star forming complexes including their surroundings in one pointing. Since NIRCams spatial resolution is $\sim 0.1''$, the physical resolution at these distances would still be ~ 0.4 pc, not much worse than what was achieved in the LMC with the VMC survey (~ 0.25 pc). Hence, it would allow to conduct similar studies as in this work for these two galaxies and their satellites, expanding greatly the types of galactic environments that can be thoroughly investigated.

A Observational epochs

Table A.1: Pawprints of K_s observations and associated photometric data.

UT date	Pawprint	MJD	T_{exp} (s)	Seeing (")
2012-02-22	Epoch 1-K1	55979.068	375	0.75
2012-02-22	Epoch 1-K2	55979.074	375	0.91
2012-02-22	Epoch 1-K3	55979.081	375	0.82
2012-02-22	Epoch 1-K4	55979.088	375	0.83
2012-02-22	Epoch 1-K5	55979.095	375	0.75
2012-02-22	Epoch 1-K6	55979.101	375	0.82
2012-02-23	Epoch 2-K1	55980.080	175	0.78
2012-02-23	Epoch 2-K2	55980.087	175	0.80
2012-02-23	Epoch 2-K3	55980.091	175	0.78
2012-02-23	Epoch 2-K4	55980.094	175	0.72
2012-02-23	Epoch 2-K5	55980.098	175	0.86
2012-02-23	Epoch 2-K6	55980.101	175	0.80
2012-02-24	Epoch 3-K1	55981.054	375	0.76
2012-02-24	Epoch 3-K2	55981.061	375	0.84
2012-02-24	Epoch 3-K3	55981.067	375	0.84
2012-02-24	Epoch 3-K4	55981.074	375	0.97
2012-02-24	Epoch 3-K5	55981.081	375	0.80
2012-02-24	Epoch 3-K6	55981.087	375	0.74
2012-02-26	Epoch 4-K1	55983.115	200	0.79
2012-02-26	Epoch 4-K2	55983.119	200	0.82
2012-02-26	Epoch 4-K3	55983.123	200	0.93
2012-02-26	Epoch 4-K4	55983.127	200	0.81
2012-02-26	Epoch 4-K5	55983.131	200	0.90
2012-02-26	Epoch 4-K6	55983.135	200	0.85
2012-02-29	Epoch 5-K1	55986.054	375	0.76
2012-02-29	Epoch 5-K2	55986.061	375	0.80
2012-02-29	Epoch 5-K3	55986.067	375	0.78
2012-02-29	Epoch 5-K4	55986.074	375	0.82
2012-02-29	Epoch 5-K5	55986.080	375	0.80
2012-02-29	Epoch 5-K6	55986.087	375	0.82

Table A.1: Pawprints of K_s observations continued.

UT date	Pawprint	MJD	T_{exp} (s)	Seeing (")
2012-03-06	Epoch 6-K1	55992.066	375	1.10
2012-03-06	Epoch 6-K2	55992.073	375	1.06
2012-03-06	Epoch 6-K3	55992.080	375	0.97
2012-03-06	Epoch 6-K4	55992.086	375	0.90
2012-03-06	Epoch 6-K5	55992.093	375	0.92
2012-03-06	Epoch 6-K6	55992.100	375	0.85
2012-03-23	Epoch 7-K1	56009.010	375	0.96
2012-03-23	Epoch 7-K2	56009.017	375	0.90
2012-03-23	Epoch 7-K3	56009.024	375	0.96
2012-03-23	Epoch 7-K4	56009.030	375	0.88
2012-03-23	Epoch 7-K5	56009.037	375	0.85
2012-03-23	Epoch 7-K6	56009.044	375	0.82
2012-09-08	Epoch 8-K1	56178.345	375	0.92
2012-09-08	Epoch 8-K2	56178.352	375	0.80
2012-09-08	Epoch 8-K3	56178.358	375	0.76
2012-09-08	Epoch 8-K4	56178.365	375	0.79
2012-09-08	Epoch 8-K5	56178.372	375	0.79
2012-09-08	Epoch 8-K6	56178.378	375	0.90
2012-09-27	Epoch 9-K1	56197.284	375	0.87
2012-09-27	Epoch 9-K2	56197.291	375	0.86
2012-09-27	Epoch 9-K3	56197.298	375	0.81
2012-09-27	Epoch 9-K4	56197.305	375	0.74
2012-09-27	Epoch 9-K5	56197.312	375	0.79
2012-09-27	Epoch 9-K6	56197.318	375	0.72
2012-10-14	Epoch 10-K1	56214.326	375	0.98
2012-10-14	Epoch 10-K2	56214.332	375	0.99
2012-10-14	Epoch 10-K3	56214.339	375	0.97
2012-10-14	Epoch 10-K4	56214.346	375	0.93
2012-10-14	Epoch 10-K5	56214.352	375	0.92
2012-10-14	Epoch 10-K6	56214.359	375	0.92
2012-11-01	Epoch 11-K1	56232.241	375	0.76
2012-11-01	Epoch 11-K2	56232.248	375	0.81
2012-11-01	Epoch 11-K3	56232.254	375	0.71
2012-11-01	Epoch 11-K4	56232.261	375	0.65
2012-11-01	Epoch 11-K5	56232.268	375	0.63
2012-11-01	Epoch 11-K6	56232.274	375	0.81
2012-11-24	Epoch 12-K1	56255.158	375	0.81
2012-11-24	Epoch 12-K2	56255.165	375	0.85

Table A.1: Pawprints of K_s observations continued.

UT date	Pawprint	MJD	T_{exp} (s)	Seeing (")
2012-11-24	Epoch 12-K3	56255.173	375	0.81
2012-11-24	Epoch 12-K4	56255.180	375	0.72
2012-11-24	Epoch 12-K5	56255.187	375	0.70
2012-11-24	Epoch 12-K6	56255.193	375	0.64
2015-01-22	Epoch 13-K1	57044.029	375	1.04
2015-01-22	Epoch 13-K2	57044.036	375	1.10
2015-01-22	Epoch 13-K3	57044.042	375	1.11
2015-01-22	Epoch 13-K4	57044.049	375	1.05
2015-01-22	Epoch 13-K5	57044.056	375	0.95
2015-01-22	Epoch 13-K6	57044.062	375	0.95
2018-01-18	Epoch 14-K1	58136.069	480	0.67
2018-01-18	Epoch 14-K2	58136.077	480	0.85
2018-01-18	Epoch 14-K3	58136.085	480	0.73
2018-01-18	Epoch 14-K4	58136.094	480	0.67
2018-01-18	Epoch 14-K5	58136.102	480	0.68
2018-01-18	Epoch 14-K6	58136.110	480	0.74
2018-01-19	Epoch 15-K1	58137.119	480	0.73
2018-01-19	Epoch 15-K2	58137.128	480	0.67
2018-01-19	Epoch 15-K3	58137.137	480	0.67
2018-01-19	Epoch 15-K4	58137.145	480	0.68
2018-01-19	Epoch 15-K5	58137.153	480	0.69
2018-01-19	Epoch 15-K6	58137.162	480	0.67
2018-01-20	Epoch 16-K1	58138.080	480	0.84
2018-01-20	Epoch 16-K2	58138.089	480	1.00
2018-01-20	Epoch 16-K3	58138.097	480	1.01
2018-01-20	Epoch 16-K4	58138.106	480	0.89
2018-01-20	Epoch 16-K5	58138.114	480	0.86
2018-01-20	Epoch 16-K6	58138.123	480	0.85
2018-01-21	Epoch 17-K1	58139.078	480	0.64
2018-01-21	Epoch 17-K2	58139.087	480	0.67
2018-01-21	Epoch 17-K3	58139.095	480	0.68
2018-01-21	Epoch 17-K4	58139.104	480	0.64
2018-01-21	Epoch 17-K5	58139.112	480	0.67
2018-01-21	Epoch 17-K6	58139.121	480	0.67
2018-01-22	Epoch 18-K1	58140.082	480	0.67
2018-01-22	Epoch 18-K2	58140.090	480	0.72
2018-01-22	Epoch 18-K3	58140.098	480	0.73
2018-01-22	Epoch 18-K4	58140.107	480	0.73

Table A.1: Pawprints of K_s observations continued.

UT date	Pawprint	MJD	T_{exp} (s)	Seeing (")
2018-01-22	Epoch 18-K5	58140.116	480	0.77
2018-01-22	Epoch 18-K6	58140.124	480	0.78
2018-01-25	Epoch 19-K1	58143.046	480	0.59
2018-01-25	Epoch 19-K2	58143.055	480	0.59
2018-01-25	Epoch 19-K3	58143.063	480	0.57
2018-01-25	Epoch 19-K4	58143.071	480	0.54
2018-01-25	Epoch 19-K5	58143.080	480	0.55
2018-01-25	Epoch 19-K6	58143.088	480	0.52
2018-01-25	Epoch 20-K1	58143.152	480	0.62
2018-01-25	Epoch 20-K2	58143.160	480	0.67
2018-01-25	Epoch 20-K3	58143.169	480	0.66
2018-01-25	Epoch 20-K4	58143.177	480	0.66
2018-01-25	Epoch 20-K5	58143.186	480	0.70
2018-01-25	Epoch 20-K6	58143.194	480	0.69
2018-01-26	Epoch 21-K1	58144.071	480	0.93
2018-01-26	Epoch 21-K2	58144.080	480	0.95
2018-01-26	Epoch 21-K3	58144.088	480	1.00
2018-01-26	Epoch 21-K4	58144.096	480	0.97
2018-01-26	Epoch 21-K5	58144.105	480	0.98
2018-01-26	Epoch 21-K6	58144.113	480	0.93
2018-01-29	Epoch 22-K1	58147.171	480	0.78
2018-01-29	Epoch 22-K2	58147.179	480	0.95
2018-01-29	Epoch 22-K3	58147.188	480	0.85
2018-01-29	Epoch 22-K4	58147.196	480	0.87
2018-01-29	Epoch 22-K5	58147.205	480	0.89
2018-01-29	Epoch 22-K6	58147.213	480	0.78
2018-02-04	Epoch 23-K1	58153.053	480	0.64
2018-02-04	Epoch 23-K2	58153.061	480	0.69
2018-02-04	Epoch 23-K3	58153.070	480	0.73
2018-02-04	Epoch 23-K4	58153.105	480	0.75
2018-02-04	Epoch 23-K5	58153.114	480	0.75
2018-02-04	Epoch 23-K6	58153.122	480	0.68
2018-02-05	Epoch 24-K1	58154.146	480	0.65
2018-02-05	Epoch 24-K2	58154.154	480	0.69
2018-02-05	Epoch 24-K3	58154.163	480	0.69
2018-02-05	Epoch 24-K4	58154.171	480	0.70
2018-02-05	Epoch 24-K5	58154.180	480	0.76
2018-02-05	Epoch 24-K6	58154.188	480	0.71

Table A.2: Pawprints of J observations and associated photometric data.

UT date	Pawprint	MJD	T _{exp} (s)	Seeing (")
2011-01-28	Epoch 1-J1	55589.158	400	0.91
2011-01-28	Epoch 1-J2	55589.165	400	0.86
2011-01-28	Epoch 1-J3	55589.171	400	0.80
2011-01-28	Epoch 1-J4	55589.176	400	0.83
2011-01-28	Epoch 1-J5	55589.184	400	0.95
2011-01-28	Epoch 1-J6	55589.190	400	0.89
2011-02-23	Epoch 2-J1	55615.061	400	0.98
2011-02-23	Epoch 2-J2	55615.067	400	0.99
2011-02-23	Epoch 2-J3	55615.074	400	1.01
2011-02-23	Epoch 2-J4	55615.080	400	1.20
2011-02-23	Epoch 2-J5	55615.086	400	1.19
2011-02-23	Epoch 2-J6	55615.092	400	1.11
2012-02-23	Epoch 3-J1	55980.059	200	0.79
2012-02-23	Epoch 3-J2	55980.062	200	0.80
2012-02-23	Epoch 3-J3	55980.066	200	0.85
2012-02-23	Epoch 3-J4	55980.069	200	0.74
2012-02-23	Epoch 3-J5	55980.072	200	0.88
2012-02-23	Epoch 3-J6	55980.076	200	0.87
2012-03-18	Epoch 4-J1	56004.029	200	0.92
2012-03-18	Epoch 4-J2	56004.032	200	1.01
2012-03-18	Epoch 4-J3	56004.036	200	1.04
2012-03-18	Epoch 4-J4	56004.039	200	0.95
2012-03-18	Epoch 4-J5	56004.043	200	0.93
2012-03-18	Epoch 4-J6	56004.046	200	0.88
2018-01-18	Epoch 5-J1	58136.120	90	0.72
2018-01-18	Epoch 5-J2	58136.121	90	0.80
2018-01-18	Epoch 5-J3	58136.123	90	0.80
2018-01-18	Epoch 5-J4	58136.125	90	0.84
2018-01-18	Epoch 5-J5	58136.127	90	0.88
2018-01-18	Epoch 5-J6	58136.128	90	0.81
2018-01-19	Epoch 6-J1	58137.171	90	0.65
2018-01-19	Epoch 6-J2	58137.173	90	0.66
2018-01-19	Epoch 6-J3	58137.174	90	0.66
2018-01-19	Epoch 6-J4	58137.176	90	0.66
2018-01-19	Epoch 6-J5	58137.178	90	0.65
2018-01-19	Epoch 6-J6	58137.180	90	0.67
2018-01-20	Epoch 7-J1	58138.131	90	0.89
2018-01-20	Epoch 7-J2	58138.133	90	0.86

Table A.2: Pawprints of J observations continued.

UT date	Pawprint	MJD	T_{exp} (s)	Seeing (")
2018-01-20	Epoch 7-J3	58138.135	90	0.88
2018-01-20	Epoch 7-J4	58138.137	90	0.88
2018-01-20	Epoch 7-J5	58138.138	90	0.82
2018-01-20	Epoch 7-J6	58138.140	90	0.88
2018-01-21	Epoch 8-J1	58139.129	90	0.76
2018-01-21	Epoch 8-J2	58139.131	90	0.79
2018-01-21	Epoch 8-J3	58139.133	90	0.77
2018-01-21	Epoch 8-J4	58139.135	90	0.78
2018-01-21	Epoch 8-J5	58139.137	90	0.81
2018-01-21	Epoch 8-J6	58139.139	90	0.76
2018-01-22	Epoch 9-J1	58140.133	90	0.81
2018-01-22	Epoch 9-J2	58140.135	90	0.81
2018-01-22	Epoch 9-J3	58140.137	90	0.79
2018-01-22	Epoch 9-J4	58140.138	90	0.77
2018-01-22	Epoch 9-J5	58140.140	90	0.76
2018-01-22	Epoch 9-J6	58140.142	90	0.83
2018-01-25	Epoch 10-J1	58143.097	90	0.53
2018-01-25	Epoch 10-J2	58143.099	90	0.58
2018-01-25	Epoch 10-J3	58143.101	90	0.61
2018-01-25	Epoch 10-J4	58143.103	90	0.59
2018-01-25	Epoch 10-J5	58143.105	90	0.60
2018-01-25	Epoch 10-J6	58143.106	90	0.65
2018-01-25	Epoch 11-J1	58143.203	90	0.74
2018-01-25	Epoch 11-J2	58143.204	90	0.74
2018-01-25	Epoch 11-J3	58143.206	90	0.74
2018-01-25	Epoch 11-J4	58143.208	90	0.74
2018-01-25	Epoch 11-J5	58143.210	90	0.75
2018-01-25	Epoch 11-J6	58143.212	90	0.71
2018-01-26	Epoch 12-J1	58144.122	90	1.05
2018-01-26	Epoch 12-J2	58144.124	90	1.01
2018-01-26	Epoch 12-J3	58144.126	90	1.02
2018-01-26	Epoch 12-J4	58144.128	90	0.94
2018-01-26	Epoch 12-J5	58144.130	90	0.96
2018-01-26	Epoch 12-J6	58144.132	90	0.97
2018-01-29	Epoch 13-J1	58147.222	90	0.92
2018-01-29	Epoch 13-J2	58147.224	90	1.00
2018-01-29	Epoch 13-J3	58147.226	90	1.03
2018-01-29	Epoch 13-J4	58147.228	90	1.03

Table A.2: Pawprints of J observations continued.

UT date	Pawprint	MJD	T_{exp} (s)	Seeing (")
2018-01-29	Epoch 13-J5	58147.230	90	1.00
2018-01-29	Epoch 13-J6	58147.231	90	0.97
2018-02-04	Epoch 14-J1	58153.130	90	0.69
2018-02-04	Epoch 14-J2	58153.132	90	0.74
2018-02-04	Epoch 14-J3	58153.134	90	0.72
2018-02-04	Epoch 14-J4	58153.136	90	0.74
2018-02-04	Epoch 14-J5	58153.137	90	0.68
2018-02-04	Epoch 14-J6	58153.139	90	0.68
2018-02-05	Epoch 15-J1	58154.197	90	0.82
2018-02-05	Epoch 15-J2	58154.198	90	1.11
2018-02-05	Epoch 15-J3	58154.200	90	0.91
2018-02-05	Epoch 15-J4	58154.206	90	0.91
2018-02-05	Epoch 15-J5	58154.208	90	0.81
2018-02-05	Epoch 15-J6	58154.210	90	0.88

Bibliography

Allison R. J., Goodwin S. P., Parker R. J., de Grijs R., Portegies Zwart S. F., Kouwenhoven M. B. N., 2009, *ApJL*, 700, L99

Ambrocio-Cruz P., Le Coarer E., Rosado M., Russeil D., Amram P., Laval A., Epinat B., Ramírez M., Odonne M., Goldes G., 2016, *MNRAS*, 457, 2048

Anderson R. I., Saio H., Ekström S., Georgy C., Meynet G., 2016, *A&A*, 591, A8

Andre P., Ward-Thompson D., Barsony M., 1993, *ApJ*, 406, 122

Audard M., Abraham P., Dunham M. M., Green J. D., Grosso N., Hamaguchi K., Kastner J. H., Kóspál Á., Lodato G., Romanova M. M., Skinner S. L., Vorobyov E. I., Zhu Z., 2014, in Beuther H., Klessen R. S., Dullemond C. P., Henning T., eds, *Protostars and Planets VI*, p. 387

Axon D. J., Ellis R. S., 1976, *Mon. Not. R. astr. Soc.*, 177, 499

Baraffe I., Homeier D., Allard F., Chabrier G., 2015, *A&A*, 577, A42

Beccari G., Petr-Gotzens M. G., Boffin H. M. J., Romaniello M., Fedele D., Carraro G., De Marchi G., de Wit W.-J., Drew J. E., Kalari V. M., Manara C. F., Martin E. L., Mieske S., Panagia N., Testi L., Vink J. S., Walsh J. R., Wright N. J., 2017, *A&A*, 604, A22

Bergin E. A., Tafalla M., 2007, *Annu. Rev. Astron. Astrophys.*, 45, 339

Bernard J.-P., Reach W. T., Paradis D., Meixner M., Paladini R., Kawamura A., Onishi T., Vijn U., Gordon K., Indebetouw R., Hora J. L., Whitney B., Blum R., Meade M., Babler B., Churchwell E. B., Engelbracht C. W., For B.-Q., Misselt K., Leitherer C., Cohen M., Boulanger F., Frogel J. A., Fukui Y., Gallagher J., Gorjian V., Harris J., Kelly D., Latter W. B., Madden S., Markwick-Kemper C.,

- Mizuno A., Mizuno N., Mould J., Nota A., Oey M. S., Olsen K., Panagia N., Perez-Gonzalez P., Shibai H., Sato S., Smith L., Staveley-Smith L., Tielens A. G. G. M., Ueta T., Van Dyk S., Volk K., Werner M., Zaritsky D., 2008, *AJ*, 136, 919
- Besla G., Kallivayalil N., Hernquist L., van der Marel R. P., Cox T. J., Kereš D., 2012, *MNRAS*, 421, 2109
- Bhandare A., Kuiper R., Henning T., Fendt C., Marleau G.-D., Kölligan A., 2018, *A&A*, 618, A95
- Biazzo K., Beccari G., De Marchi G., Panagia N., 2019, *ApJ*, 875(1), 51
- Bica E., Bonatto C., Dutra C. M., Santos J. F. C., 2008, *MNRAS*, 389, 678
- Bok B. J., 1966, *Annu. Rev. Astron. Astrophys.*, 4, 95
- Bonnell I. A., Bate M. R., 2006, *Mon. Not. R. astr. Soc.*, 370(1), 488
- Bonnell I. A., Davies M. B., 1998, *MNRAS*, 295, 691
- Book L. G., Chu Y.-H., Gruendl R. A., Fukui Y., 2009, *AJ*, 137, 3599
- Borissova J., Ramírez Alegría S., Alonso J., Lucas P. W., Kurtev R., Medina N., Navarro C., Kuhn M., Gromadzki M., Retamales G., Fernandez M. A., Agurto-Gangas C., Chené A. N., Minniti D., Contreras Pena C., Catelan M., Decany I., Thompson M. A., Morales E. F. E., Amigo P., 2016, *AJ*, 152(3), 74
- Bouvier J., Bertout C., 1989, *A&A*, 211, 99
- Bouvier J., Cabrit S., Fernandez M., Martin E. L., Matthews J. M., 1993, *A&A*, 272, 176
- Bouvier J., Grankin K. N., Alencar S. H. P., Dougados C., Fernández M., Basri G., Batalha C., Guenther E., Ibrahimov M. A., Magakian T. Y., Melnikov S. Y., Petrov P. P., Rud M. V., Zapatero Osorio M. R., 2003, *A&A*, 409, 169

- Bressan A., Marigo P., Girardi L., Salasnich B., Dal Cero C., Rubele S., Nanni A., 2012, *MNRAS*, 427, 127
- Briceño C., Calvet N., Hernández J., Vivas A. K., Hartmann L., Downes J. J., Berlind P., 2005, *AJ*, 129, 907
- Cañas C. I., Bender C. F., Mahadevan S., Fleming S. W., Beatty T. G., Covey K. R., De Lee N., Hearty F. R., García-Hernández D. A., Majewski S. R., Schneider D. P., Stassun K. G., Wilson R. F., 2018, *ApJL*, 861(1), L4
- Cardelli J. A., Clayton G. C., Mathis J. S., 1989, *ApJ*, 345, 245
- Carlson L. R., Sewilo M., Meixner M., Romita K. A., Lawton B., 2012, *A&A*, 542, A66
- Carpenter J. M., Hillenbrand L. A., Skrutskie M. F., 2001, *AJ*, 121, 3160
- Casey C. M., Narayanan D., Cooray A., 2014, *Phys. Rep.*, 541, 45
- Catelan M., Minniti D., Lucas P. W., Alonso-García J., Angeloni R., Beamín J. C., Bonatto C., Borissova J., Contreras C., Cross N., Dékány I., Emerson J. P., Eyheramendy S., Geisler D., González-Solares E., Helminiak K. G., Hempel M., Irwin M. J., Ivanov V. D., Jordán A., Kerins E., Kurtev R., Mauro F., Moni Bidin C., Navarrete C., Pérez P., Pichara K., Read M., Rejkuba M., Saito R. K., Sale S. E., Toledo I., 2011, in McWilliam A., ed., *RR Lyrae Stars, Metal-Poor Stars, and the Galaxy Vol. 5*, p. 145
- Chen C.-H. R., Chu Y.-H., Gruendl R. A., Gordon K. D., Heitsch F., 2009, *ApJ*, 695, 511
- Cignoni M., Sabbi E., van der Marel R. P., Tosi M., Zaritsky D., Anderson J., Lennon D. J., Aloisi A., de Marchi G., Gouliermis D. A., Grebel E. K., Smith L. J., Zeidler P., 2015, *ApJ*, 811, 76
- Cioni M.-R. L., 2009, *A&A*, 506, 1137

- Cioni M.-R. L., Clementini G., Girardi L., Guandalini R., Gullieuszik M., Miszalski B., Moretti M.-I., Ripepi V., Rubele S., Bagheri G., Bekki K., Cross N., de Blok W. J. G., de Grijs R., Emerson J. P., Evans C. J., Gibson B., Gonzales-Solares E., Groenewegen M. A. T., Irwin M., Ivanov V. D., Lewis J., Marconi M., Marquette J.-B., Mastropietro C., Moore B., Napiwotzki R., Naylor T., Oliveira J. M., Read M., Sutorius E., van Loon J. T., Wilkinson M. I., Wood P. R., 2011, *A&A*, 527, A116
- Cody A. M., Stauffer J., Baglin A., Micela G., Rebull L. M., Flaccomio E., Morales-Calderón M., Aigrain S., Bouvier J., Hillenbrand L. A., Gutermuth R., Song I., Turner N., Alencar S. H. P., Zwintz K., Plavchan P., Carpenter J., Findeisen K., Carey S., Terebey S., Hartmann L., Calvet N., Teixeira P., Vrba F. J., Wolk S., Covey K., Poppenhaeger K., Günther H. M., Forbrich J., Whitney B., Affer L., Herbst W., Hora J., Barrado D., Holtzman J., Marchis F., Wood K., Medeiros Guimarães M., Lillo Box J., Gillen E., McQuillan A., Espaillat C., Allen L., D'Alessio P., Favata F., 2014, *AJ*, 147, 82
- Contreras Peña C., Lucas P. W., Froebrich D., Kumar M. S. N., Goldstein J., Drew J. E., Adamson A., Davis C. J., Barentsen G., Wright N. J., 2014, *MNRAS*, 439(2), 1829
- Contreras Peña C., Lucas P. W., Kurtev R., Minniti D., Caratti o Garatti A., Marocco F., Thompson M. A., Froebrich D., Kumar M. S. N., Stimson W., Navarro Molina C., Borissova J., Gledhill T., Terzi R., 2017a, *Mon. Not. R. astr. Soc.*, 465(3), 3039
- Contreras Peña C., Lucas P. W., Minniti D., Kurtev R., Stimson W., Navarro Molina C., Borissova J., Kumar M. S. N., Thompson M. A., Gledhill T., Terzi R., Froebrich D., Caratti o Garatti A., 2017b, *MNRAS*, 465(3), 3011
- Cook D. O., Dale D. A., Johnson B. D., Van Zee L., Lee J. C., Kennicutt R. C., Calzetti D., Staudaher S. M., Engelbracht C. W., 2014, *MNRAS*, 445, 881

- Cormier D., Lebouteiller V., Madden S. C., Abel N., Hony S., Galliano F., Baes M., Barlow M. J., Cooray A., De Looze I., Galametz M., Karczewski O. L., Parkin T. J., Rémy A., Sauvage M., Spinoglio L., Wilson C. D., Wu R., 2012, *A&A*, 548, A20
- Cross N. J. G., Collins R. S., Mann R. G., Read M. A., Sutorius E. T. W., Blake R. P., Holliman M., Hambly N. C., Emerson J. P., Lawrence A., Noddle K. T., 2012, *A&A*, 548, A119
- Da Rio N., Gouliermis D. A., Gennaro M., 2010, *ApJ*, 723(1), 166
- Da Rio N., Gouliermis D. A., Henning T., 2009, *ApJ*, 696, 528
- Dalton G. B., Caldwell M., Ward A. K., Whalley M. S., Woodhouse G., Edeson R. L., Clark P., Beard S. M., Gallie A. M., Todd S. P., Strachan J. M. D., Bezawada N. N., Sutherland W. J., Emerson J. P., 2006, *Proc. SPIE Vol. 6269*, p. 62690X
- de Grijs R., Anders P., 2006, *MNRAS*, 366, 295
- de Grijs R., Bono G., 2015, *AJ*, 149, 179
- de Grijs R., Goodwin S. P., 2008, *MNRAS*, 383, 1000
- de Grijs R., Gilmore G. F., Johnson R. A., Mackey A. D., 2002, *MNRAS*, 331, 245
- de Grijs R., Wicker J. E., Bono G., 2014, *AJ*, 147, 122
- De Marchi G., Beccari G., Panagia N., 2013a, *ApJ*, 775, 68
- De Marchi G., Beccari G., Panagia N., 2013b, *ApJ*, 775, 68
- De Marchi G., Panagia N., Romaniello M., Sabbi E., Sirianni M., Prada Moroni P. G., Degl'Innocenti S., 2011, *ApJ*, 740, 11
- De Marchi G., Panagia N., Sabbi E., Lennon D., Anderson J., van der Marel R., Cignoni M., Grebel E. K., Larsen S., Zaritsky D., Zeidler P., Gouliermis D., Aloisi A., 2016, *Mon. Not. R. astr. Soc.*, 455(4), 4373

- Dobbs C. L., Pringle J. E., 2013, *MNRAS*, 432(1), 653
- Dobbs C. L., Krumholz M. R., Ballesteros-Paredes J., Bolatto A. D., Fukui Y., Heyer M., Low M. M. M., Ostriker E. C., Vázquez-Semadeni E., 2014, in Beuther H., Klessen R. S., Dullemond C. P., Henning T., eds, *Protostars and Planets VI*, p. 3
- Durisen R. H., Boss A. P., Mayer L., Nelson A. F., Quinn T., Rice W. K. M., 2007, *Protostars and Planets V*, , 607
- Edwards S., Hartigan P., Ghandour L., Andrulis C., 1994, *AJ*, 108
- Eiroa C., Oudmaijer R. D., Davies J. K., de Winter D., Garzón F., Palacios J., Alberdi A., Ferlet R., Grady C. A., Collier Cameron A., Deeg H. J., Harris A. W., Horne K., Merín B., Miranda L. F., Montesinos B., Mora A., Penny A., Quirrenbach A., Rauer H., Schneider J., Solano E., Tsapras Y., Wesselius P. R., 2002, *A&A*, 384, 1038
- Elmegreen B. G., Falgarone E., 1996, *ApJ*, 471, 816
- Elmegreen B. G., 2008, in de Koter A., Smith L. J., Waters L. B. F. M., eds, *Mass Loss from Stars and the Evolution of Stellar Clusters*, *Astronomical Society of the Pacific Conference Series Vol. 388*, p. 249
- Emerson J., McPherson A., Sutherland W., 2006, *The Messenger*, 126, 41
- Ercolano B., Clarke C. J., 2010, *MNRAS*, 402, 2735
- Evans C. J., Taylor W. D., Hénault-Brunet V., Sana H., de Koter A., Simón-Díaz S., Carraro G., Bagnoli T., Bastian N., Bestenlehner J. M., Bonanos A. Z., Bressert E., Brott I., Campbell M. A., Cantiello M., Clark J. S., Costa E., Crowther P. A., de Mink S. E., Doran E., Dufton P. L., Dunstall P. R., Friedrich K., Garcia M., Gieles M., Gräfener G., Herrero A., Howarth I. D., Izzard R. G., Langer N., Lennon D. J., Maíz Apellániz J., Markova N., Najarro F., Puls J., Ramirez O. H., Sabín-Sanjulián C., Smartt S. J., Stroud V. E., van Loon J. T., Vink J. S., Walborn N. R., 2011, *A&A*, 530, A108

- Evans M. G., Ilee J. D., Boley A. C., Caselli P., Durisen R. H., Hartquist T. W., Rawlings J. M. C., 2015, *MNRAS*, 453, 1147
- Fazio G. G., Hora J. L., Allen L. E., Ashby M. L. N., Barmby P., Deutsch L. K., Huang J. S., Kleiner S., Marengo M., Megeath S. T., Melnick G. J., Pahre M. A., Patten B. M., Polizotti J., Smith H. A., Taylor R. S., Wang Z., Willner S. P., Hoffmann W. F., Pipher J. L., Forrest W. J., McMurty C. W., McCreight C. R., McKelvey M. E., McMurray R. E., Koch D. G., Moseley S. H., Arendt R. G., Mentzell J. E., Marx C. T., Losch P., Mayman P., Eichhorn W., Krebs D., Jhabvala M., Gezari D. Y., Fixsen D. J., Flores J., Shakoorzadeh K., Jungo R., Hakun C., Workman L., Karpati G., Kichak R., Whitley R., Mann S., Tollestrup E. V., Eisenhardt P., Stern D., Gorjian V., Bhattacharya B., Carey S., Nelson B. O., Glaccum W. J., Lacy M., Lowrance P. J., Laine S., Reach W. T., Stauffer J. A., Surace J. A., Wilson G., Wright E. L., Hoffman A., Domingo G., Cohen M., 2004, *ApJS*, 154(1), 10
- Feast M. W., Glass I. S., Whitelock P. A., Catchpole R. M., 1989, *Mon. Not. R. astr. Soc.*, 241, 375
- Findeisen K., Hillenbrand L., Ofek E., Levitan D., Sesar B., Laher R., Surace J., 2013, *ApJ*, 768(1), 93
- Fleck, Jr. R. C., 1996, *ApJ*, 458, 739
- Fukui Y., Mizuno N., Yamaguchi R., Mizuno A., Onishi T., 2001, *PASJ*, 53(6), L41
- Gaczkowski B., Preibisch T., Ratzka T., Roccatagliata V., Ohlendorf H., Zinnecker H., 2013, *A&A*, 549, A67
- Gardner J. P., Mather J. C., Clampin M., Doyon R., Greenhouse M. A., Hammel H. B., Hutchings J. B., Jakobsen P., Lilly S. J., Long K. S., Lunine J. I., McCaughrean M. J., Mountain M., Nella J., Rieke G. H., Rieke M. J., Rix H.-W., Smith E. P., Sonneborn G., Stiavelli M., Stockman H. S., Windhorst R. A., Wright G. S., 2006, *Sp. Sci. Rev.*, 123, 485

- Gennaro M., Brandner W., Stolte A., Henning T., 2011, MNRAS, 412, 2469
- Gilmozzi R., Kinney E. K., Ewald S. P., Panagia N., Romaniello M., 1994, ApJL, 435, L43
- Girardi L., Salaris M., 2001, MNRAS, 323, 109
- Girardi L., Goudfrooij P., Kalirai J. S., Kerber L., Kozhurina-Platais V., Rubele S., Bressan A., Chandar R., Marigo P., Platais I., Puzia T. H., 2013, MNRAS, 431, 3501
- Glatt K., Grebel E. K., Koch A., 2010, A&A, 517, A50
- Glover S. C. O., Clark P. C., 2012, MNRAS, 426(1), 377
- Goldreich P., Kwan J., 1974, ApJ, 189, 441
- González-Fernández C., Hodgkin S. T., Irwin M. J., González-Solares E., Koposov S. E., Lewis J. R., Emerson J. P., Hewett P. C., Yoldaş A. K., Riello M., 2018, MNRAS, 474, 5459
- Gordon K. D., Roman-Duval J., Bot C., Meixner M., Babler B., Bernard J.-P., Bolatto A., Boyer M. L., Clayton G. C., Engelbracht C., Fukui Y., Galametz M., Galliano F., Hony S., Hughes A., Indebetouw R., Israel F. P., Jameson K., Kawamura A., Leboutteiller V., Li A., Madden S. C., Matsuura M., Misselt K., Montiel E., Okumura K., Onishi T., Panuzzo P., Paradis D., Rubio M., Sandstrom K., Sauvage M., Seale J., Sewilo M., Tchernyshyov K., Skibba R., 2014, ApJ, 797(2), 85
- Gouliermis D. A., 2018, PASP, 130(7), 072001
- Gouliermis D., Brandner W., Henning T., 2005, ApJ, 623(2), 846
- Gouliermis D., Brandner W., Henning T., 2006, ApJL, 636, L133
- Gouliermis D., Kontizas M., Kontizas E., Korakitis R., 2003, A&A, 405, 111

- Gouliermis D. A., Dolphin A. E., Brandner W., Henning T., 2006, *ApJS*, 166, 549
- Gouliermis D. A., Henning T., Brandner W., Dolphin A. E., Rosa M., Brandl B., 2007, *ApJL*, 665, L27
- Gouliermis D. A., Schmeja S., Klessen R. S., de Blok W. J. G., Walter F., 2010, *ApJ*, 725(2), 1717
- Gouliermis D. A., Dolphin A. E., Robberto M., Gruendl R. A., Chu Y.-H., Gennaro M., Henning T., Rosa M., Da Rio N., Brandner W., Romaniello M., De Marchi G., Panagia N., Zinnecker H., 2011, *ApJ*, 738, 137
- Gouliermis D. A., Schmeja S., Dolphin A. E., Gennaro M., Tognelli E., Prada Moroni P. G., 2012, *ApJ*, 748, 64
- Gouliermis D. A., Elmegreen B. G., Elmegreen D. M., Calzetti D., Cignoni M., Gallagher, John S. I., Kennicutt R. C., Klessen R. S., Sabbi E., Thilker D., Ubeda L., Aloisi A., Adamo A., Cook D. O., Dale D., Grasha K., Grebel E. K., Johnson K. E., Sacchi E., Shabani F., Smith L. J., Wofford A., 2017, *Mon. Not. R. astr. Soc.*, 468(1), 509
- Grebel E. K., Chu Y.-H., 2000, *AJ*, 119(2), 787
- Gruendl R. A., Chu Y.-H., 2009, *ApJS*, 184, 172
- Gry C., Boulanger F., Nehmé C., Pineau des Forêts G., Habart E., Falgarone E., 2002, *A&A*, 391, 675
- Haisch, Karl E. J., Lada E. A., Lada C. J., 2001, *ApJ*, 553(2), L153
- Harris J., Zaritsky D., 2009, *AJ*, 138, 1243
- Hartmann L., Kenyon S. J., 1996, *Annu. Rev. Astron. Astrophys.*, 34, 207
- Hartmann L., 1998, *Accretion Processes in Star Formation*

- Hartmann L., Hewett R., Calvet N., 1994, *ApJ*, 426, 669
- Hayashi C., 1966, *Annu. Rev. Astron. Astrophys.*, 4, 171
- Henize K. G., 1956, *ApJS*, 2, 315
- Herbig G. H., 1952, *J. R. Astron. Soc. Canada*, 46, 222
- Herbig G. H., 1960, *ApJS*, 4, 337
- Herbig G. H., 1977, *ApJ*, 217, 693
- Herbig G. H., 2007, *AJ*, 133(6), 2679
- Hoare M. G., Franco J., 2007, *Astrophysics and Space Science Proceedings*, 1, 61
- Hodapp K. W., Chini R., Watermann R., Lemke R., 2012, *ApJ*, 744(1), 56
- Hollenbach D. J., Yorke H. W., Johnstone D., 2000, in Mannings V., Boss A. P., Russell S. S., eds, *Protostars and Planets IV*, p. 401
- Hony S., Gouliermis D. A., Galliano F., Galametz M., Cormier D., Chen C.-H. R., Dib S., Hughes A., Klessen R. S., Roman-Duval J., Smith L., Bernard J.-P., Bot C., Carlson L., Gordon K., Indebetouw R., Lebouteiller V., Lee M.-Y., Madden S. C., Meixner M., Oliveira J., Rubio M., Sauvage M., Wu R., 2015, *MNRAS*, 448, 1847
- Horner S. D., Rieke M. J., 2004, in Mather J. C., ed., *Proc. SPIE, Society of Photo-Optical Instrumentation Engineers (SPIE) Conference Series Vol. 5487*, p. 628
- Hunter D. A., Elmegreen B. G., Dupuy T. J., Mortonson M., 2003, *AJ*, 126, 1836
- Indebetouw R., Johnson K. E., Conti P., 2004, *AJ*, 128, 2206
- Irwin M. J., Lewis J., Hodgkin S., Bunclark P., Evans D., McMahon R., Emerson J. P., Stewart M., Beard S., 2004, in Quinn P. J., Bridger A., eds, *Optimizing Scientific Return for Astronomy through Information Technologies*, *Proc. SPIE Vol. 5493*, p. 411

- Ivanov V. D., Cioni M.-R. L., Bekki K., de Grijs R., Emerson J., Gibson B. K., Kamath D., van Loon J. T., Piatti A. E., For B.-Q., 2016, *A&A*, 588, A93
- Javadi A., van Loon J. T., Khosroshahi H. G., Tabatabaei F., Hamedani Golshan R., Rashidi M., 2017, *MNRAS*, 464, 2103
- Jeans J. H., 1902, *Philosophical Transactions of the Royal Society of London Series A*, 199, 1
- Jones O. C., Woods P. M., Kemper F., Kraemer K. E., Sloan G. C., Srinivasan S., Oliveira J. M., van Loon J. T., Boyer M. L., Sargent B. A., 2017, *MNRAS*, 470(3), 3250
- Joy A. H., 1945, *ApJ*, 102, 168
- Karachentsev I. D., Karachentseva V. E., Huchtmeier W. K., Makarov D. I., 2004, *AJ*, 127(4), 2031
- Kato D., Nagashima C., Nagayama T., Kurita M., Koerwer J. F., Kawai T., Yamamuro T., Zenno T., Nishiyama S., Baba D., 2007, *PASJ*, 59, 615
- Kerber L. O., Girardi L., Rubele S., Cioni M.-R., 2009, *A&A*, 499, 697
- Klessen R. S., Glover S. C. O., 2016, *Star Formation in Galaxy Evolution: Connecting Numerical Models to Reality*, Saas-Fee Advanced Course, Volume 43, ISBN 978-3-662-47889-9, Springer-Verlag Berlin Heidelberg, 2016, p. 85, 43, 85
- Kourniotis M., Bonanos A. Z., Soszyński I., Poleski R., Krikelis G., Udalski A., Szymański M. K., Kubiak M., Pietrzyński G., Wyrzykowski Ł., Ulaczyk K., Kozłowski S., Pietrukowicz P., 2014, *A&A*, 562, A125
- Kroupa P., 2001, *MNRAS*, 322, 231
- Kroupa P., 2002, *Science*, 295, 82
- Krumholz M. R., 2015, arXiv e-prints, , arXiv:1511.03457

- Krumholz M. R., Klein R. I., McKee C. F., 2012, *ApJ*, 754(1), 71
- Krumholz M. R., McKee C. F., Klein R. I., 2005, *Nature*, 438(7066), 332
- Kuiper R., Klahr H., Beuther H., Henning T., 2010, *ApJ*, 722(2), 1556
- Lada C. J., 1987, in Peimbert M., Jugaku J., eds, *Star Forming Regions*, IAU Symposium Vol. 115, p. 1
- Larson R. B., 1973, *Annu. Rev. Astron. Astrophys.*, 11, 219
- Leavitt H. S., Pickering E. C., 1912, *Harvard College Observatory Circular*, 173, 1
- Li Y., Calzetti D., Kennicutt R. C., Hong S., Engelbracht C. W., Dale D. A., Moustakas J., 2010, *ApJ*, 725(1), 677
- Liu Q., de Grijs R., Deng L. C., Hu Y., Baraffe I., Beaulieu S. F., 2009a, *MNRAS*, 396, 1665
- Liu Q., de Grijs R., Deng L. C., Hu Y., Beaulieu S. F., 2009b, *A&A*, 503, 469
- Lomb N. R., 1976, *Ap&SS*, 39(2), 447
- Lucas P. W., Smith L. C., Contreras Peña C., Froebrich D., Drew J. E., Kumar M. S. N., Borissova J., Minniti D., Kurtev R., Monguió M., 2017, *MNRAS*, 472(3), 2990
- Lucke P. B., Hodge P. W., 1970, *AJ*, 75, 171
- Lynden-Bell D., Pringle J. E., 1974, *MNRAS*, 168, 603
- Madore B. F., Freedman W. L., 1991, *PASP*, 103, 933
- Manara C. F., Rosotti G., Testi L., Natta A., Alcalá J. M., Williams J. P., Ansdell M., Miotello A., van der Marel N., Tazzari M., Carpenter J., Guidi G., Mathews G. S., Oliveira I., Prusti T., van Dishoeck E. F., 2016, *A&A*, 591, L3
- Marks M., Kroupa P., Dabringhausen J., Pawłowski M. S., 2012, *MNRAS*, 422, 2246

- Martín-Navarro I., Vazdekis A., La Barbera F., Falcón-Barroso J., Lyubenova M., van de Ven G., Ferreras I., Sánchez S. F., Trager S. C., García-Benito R., Mast D., Mendoza M. A., Sánchez-Blázquez P., González Delgado R., Walcher C. J., The CALIFA Team, 2015, *ApJL*, 806, L31
- Massey P., Silkey M., Garmany C. D., Degioia-Eastwood K., 1989, *AJ*, 97, 107
- Massey P., Parker J. W., Garmany C. D., 1989, *AJ*, 98, 1305
- Mathis J. S., 1990, *Annu. Rev. Astron. Astrophys.*, 28, 37
- McKee C. F., Tan J. C., 2003, *ApJ*, 585(2), 850
- Meingast S., Alves J., Mardones D., Teixeira P. S., Lombardi M., Großschedl J., Ascenso J., Bouy H., Forbrich J., Goodman A., Hacar A., Hasenberger B., Kainulainen J., Kubiak K., Lada C., Lada E., Moitinho A., Petr-Gotzens M., Rodrigues L., Román-Zúñiga C. G., 2016, *A&A*, 587, A153
- Meixner M., Gordon K. D., Indebetouw R., Hora J. L., Whitney B., Blum R., Reach W., Bernard J.-P., Meade M., Babler B., Engelbracht C. W., For B.-Q., Misselt K., Vijn U., Leitherer C., Cohen M., Churchwell E. B., Boulanger F., Frogel J. A., Fukui Y., Gallagher J., Gorjian V., Harris J., Kelly D., Kawamura A., Kim S., Latter W. B., Madden S., Markwick-Kemper C., Mizuno A., Mizuno N., Mould J., Nota A., Oey M. S., Olsen K., Onishi T., Paladini R., Panagia N., Perez-Gonzalez P., Shibai H., Sato S., Smith L., Staveley-Smith L., Tielens A. G. G. M., Ueta T., van Dyk S., Volk K., Werner M., Zaritsky D., 2006, *AJ*, 132, 2268
- Meixner M., Panuzzo P., Roman-Duval J., Engelbracht C., Babler B., Seale J., Hony S., Montiel E., Sauvage M., Gordon K., Misselt K., Okumura K., Chaniel P., Beck T., Bernard J.-P., Bolatto A., Bot C., Boyer M. L., Carlson L. R., Clayton G. C., Chen C.-H. R., Cormier D., Fukui Y., Galametz M., Galliano F., Hora J. L., Hughes A., Indebetouw R., Israel F. P., Kawamura A., Kemper F., Kim S., Kwon E., Lebouteiller V., Li A., Long K. S., Madden S. C., Matsuura M.,

- Muller E., Oliveira J. M., Onishi T., Otsuka M., Paradis D., Poglitsch A., Reach W. T., Robitaille T. P., Rubio M., Sargent B., Sewilo M., Skibba R., Smith L. J., Srinivasan S., Tielens A. G. G. M., van Loon J. T., Whitney B., 2013, *AJ*, 146, 62
- Moeckel N., Bate M. R., 2010, *MNRAS*, 404, 721
- Mollá M., García-Vargas M. L., Bressan A., 2009, *MNRAS*, 398, 451
- Monson A. J., Beaton R. L., Scowcroft V., Freedman W. L., Madore B. F., Rich J. A., Seibert M., Kollmeier J. A., Clementini G., 2017, *AJ*, 153(3), 96
- Moody M. S. L., Stahler S. W., 2017, *A&A*, 600, A133
- Morales-Calderón M., Stauffer J. R., Hillenbrand L. A., Gutermuth R., Song I., Rebull L. M., Plavchan P., Carpenter J. M., Whitney B. A., Covey K., Alves de Oliveira C., Winston E., McCaughrean M. J., Bouvier J., Guieu S., Vrba F. J., Holtzman J., Marchis F., Hora J. L., Wasserman L. H., Terebey S., Megeath T., Guinan E., Forbrich J., Huélamo N., Riviere-Marichalar P., Barrado D., Stapelfeldt K., Hernández J., Allen L. E., Ardila D. R., Bayo A., Favata F., James D., Werner M., Wood K., 2011, *ApJ*, 733, 50
- Moretti M. I., Clementini G., Muraveva T., Ripepi V., Marquette J. B., Cioni M. R. L., Marconi M., Girardi L., Rubele S., Tisserand P., de Grijs R., Groenewegen M. A. T., Guandalini R., Ivanov V. D., van Loon J. T., 2014, *MNRAS*, 437(3), 2702
- Muraveva T., Subramanian S., Clementini G., Cioni M. R. L., Palmer M., van Loon J. T., Moretti M. I., de Grijs R., Molinaro R., Ripepi V., Marconi M., Emerson J., Ivanov V. D., 2018a, *MNRAS*, 473(3), 3131
- Muraveva T., Delgado H. E., Clementini G., Sarro L. M., Garofalo A., 2018b, *MNRAS*, 481(1), 1195
- Myers P. C., Goodman A. A., 1988, *ApJ*, 329, 392

- Myers A. T., McKee C. F., Cunningham A. J., Klein R. I., Krumholz M. R., 2013, *ApJ*, 766(2), 97
- Natta A., Whitney B. A., 2000, *A&A*, 364, 633
- Nidever D. L., Olsen K., Walker A. R., Vivas A. K., Blum R. D., Kaleida C., Choi Y., Conn B. C., Gruendl R. A., Bell E. F., Besla G., Muñoz R. R., Gallart C., Martin N. F., Olszewski E. W., Saha A., Monachesi A., Monelli M., de Boer T. J. L., Johnson L. C., Zaritsky D., Stringfellow G. S., van der Marel R. P., Cioni M.-R. L., Jin S., Majewski S. R., Martinez-Delgado D., Monteagudo L., Noël N. E. D., Bernard E. J., Kunder A., Chu Y.-H., Bell C. P. M., Santana F., Frechem J., Medina G. E., Parkash V., Serón Navarrete J. C., Hayes C., 2017, *AJ*, 154(5), 199
- Niederhofer F., Hilker M., Bastian N., Silva-Villa E., 2015, *A&A*, 575, A62
- Niederhofer F., Bastian N., Kozhurina-Platais V., Larsen S., Hollyhead K., Lardo C., Cabrera-Ziri I., Kacharov N., Platais I., Salaris M., Cordero M., Dalessandro E., Geisler D., Hilker M., Li C., Mackey D., Mucciarelli A., 2017, *MNRAS*, 465, 4159
- Niederhofer F., Cioni M.-R. L., Rubele S., Schmidt T., Bekki K., de Grijs R., Emerson J., Ivanov V. D., Oliveira J. M., Petr-Gotzens M. G., Ripepi V., Sun N.-C., van Loon J. T., 2018, *A&A*, 612, A115
- Nishiyama S., Tamura M., Hatano H., Kato D., Tanabé T., Sugitani K., Nagata T., 2009, *ApJ*, 696(2), 1407
- Offner S. S. R., McKee C. F., 2011, *ApJ*, 736(1), 53
- Oliveira J. M., van Loon J. T., Stanimirović S., Zijlstra A. A., 2006, *MNRAS*, 372(4), 1509
- Oliveira J. M., van Loon J. T., Chen C. H. R., Tielens A. G. G. M., Sloan G. C., Woods P. M., Kemper F., Indebetouw R., Gordon K. D., Boyer M. L., Shiao B., Madden S., Speck A. K., Meixner M., Marengo M., 2009, *ApJ*, 707(2), 1269

- Paczyński B., Stanek K. Z., 1998, *ApJL*, 494, L219
- Panagia N., Romaniello M., Scuderi S., Kirshner R. P., 2000, *ApJ*, 539, 197
- Pang X., Grebel E. K., Allison R. J., Goodwin S. P., Altmann M., Harbeck D., Moffat A. F. J., Drissen L., 2013, *ApJ*, 764, 73
- Parsons H., Thompson M. A., Chrysostomou A., 2009, *MNRAS*, 399(3), 1506
- Pecaut M. J., Mamajek E. E., 2013, *ApJS*, 208, 9
- Pei Y. C., Fall S. M., Hauser M. G., 1999, *ApJ*, 522, 604
- Pfalzner S., 2008, *A&A*, 492(3), 735
- Pfalzner S., Parmentier G., Steinhausen M., Vincke K., Menten K., 2014, *ApJ*, 794, 147
- Piatti A. E., Guandalini R., Ivanov V. D., Rubele S., Cioni M.-R. L., de Grijs R., For B.-Q., Clementini G., Ripepi V., Anders P., Oliveira J. M., 2014, *A&A*, 570, A74
- Piatti A. E., Ivanov V. D., Rubele S., Marconi M., Ripepi V., Cioni M.-R. L., Oliveira J. M., Bekki K., 2016, *MNRAS*, 460, 383
- Pilbratt G. L., Riedinger J. R., Passvogel T., Crone G., Doyle D., Gageur U., Heras A. M., Jewell C., Metcalfe L., Ott S., Schmidt M., 2010, *A&A*, 518, L1
- Popescu B., Hanson M. M., Elmegreen B. G., 2012, *ApJ*, 751, 122
- Poppenhaeger K., Cody A. M., Covey K. R., Günther H. M., Hillenbrand L. A., Plavchan P., Rebull L. M., Stauffer J. R., Wolk S. J., Espaillat C., Forbrich J., Gutermuth R. A., Hora J. L., Morales-Calderón M., Song I., 2015, *AJ*, 150(4), 118
- Preibisch T., Roccatagliata V., Gaczowski B., Ratzka T., 2012, *A&A*, 541, A132

- Rebull L. M., Cody A. M., Covey K. R., Günther H. M., Hillenbrand L. A., Plavchan P., Poppenhaeger K., Stauffer J. R., Wolk S. J., Gutermuth R., Morales-Calderón M., Song I., Barrado D., Bayo A., James D., Hora J. L., Vrba F. J., Alves de Oliveira C., Bouvier J., Carey S. J., Carpenter J. M., Favata F., Flaherty K., Forbrich J., Hernandez J., McCaughrean M. J., Megeath S. T., Micela G., Smith H. A., Terebey S., Turner N., Allen L., Ardila D., Bouy H., Guieu S., 2014, *AJ*, 148, 92
- Rémy-Ruyer A., Madden S. C., Galliano F., Galametz M., Takeuchi T. T., Asano R. S., Zhukovska S., Lebouteiller V., Cormier D., Jones A., Bocchio M., Baes M., Bendo G. J., Boquien M., Boselli A., DeLooze I., Doublier-Pritchard V., Hughes T., Karczewski O. L., Spinoglio L., 2014, *A&A*, 563, A31
- Rice T. S., Reipurth B., Wolk S. J., Vaz L. P., Cross N. J. G., 2015, *AJ*, 150, 132
- Riebel D., Boyer M. L., Srinivasan S., Whitelock P., Meixner M., Babler B., Feast M., Groenewegen M. A. T., Ita Y., Meade M., Shiao B., Whitney B., 2015, *ApJ*, 807(1), 1
- Rieke G. H., Young E. T., Engelbracht C. W., Kelly D. M., Low F. J., Haller E. E., Beeman J. W., Gordon K. D., Stansberry J. A., Misselt K. A., Cadien J., Morrison J. E., Rivlis G., Latter W. B., Noriega-Crespo A., Padgett D. L., Stapelfeldt K. R., Hines D. C., Egami E., Muzerolle J., Alonso-Herrero A., Blaylock M., Dole H., Hinz J. L., Le Floc'h E., Papovich C., Pérez-González P. G., Smith P. S., Su K. Y. L., Bennett L., Frayer D. T., Henderson D., Lu N., Masci F., Pesenson M., Rebull L., Rho J., Keene J., Stolovy S., Wachter S., Wheaton W., Werner M. W., Richards P. L., 2004, *ApJS*, 154(1), 25
- Ripepi V., Cioni M.-R. L., Moretti M. I., Marconi M., Bekki K., Clementini G., de Grijs R., Emerson J., Groenewegen M. A. T., Ivanov V. D., Molinaro R., Muraveva T., Oliveira J. M., Piatti A. E., Subramanian S., van Loon J. T., 2017, *MNRAS*, 472(1), 808

- Robitaille T. P., Whitney B. A., Indebetouw R., Wood K., Denzmore P., 2006, *ApJS*, 167(2), 256
- Roccatagliata V., Preibisch T., Ratzka T., Gaczkowski B., 2013, *A&A*, 554, A6
- Roman-Duval J., Gordon K. D., Meixner M., Bot C., Bolatto A., Hughes A., Wong T., Babler B., Bernard J.-P., Clayton G. C., Fukui Y., Galametz M., Galliano F., Glover S., Hony S., Israel F., Jameson K., Leboutteiller V., Lee M.-Y., Li A., Madden S., Misselt K., Montiel E., Okumura K., Onishi T., Panuzzo P., Reach W., Remy-Ruyer A., Robitaille T., Rubio M., Sauvage M., Seale J., Sewilo M., Staveley-Smith L., Zhukovska S., 2014, *ApJ*, 797(2), 86
- Rubele S., Girardi L., Kozhurina-Platais V., Goudfrooij P., Kerber L., 2011, *MNRAS*, 414, 2204
- Rubele S., Kerber L., Girardi L., Cioni M.-R., Marigo P., Zaggia S., Bekki K., de Grijs R., Emerson J., Groenewegen M. A. T., Gullieuszik M., Ivanov V., Miszalski B., Oliveira J. M., Tatton B., van Loon J. T., 2012, *A&A*, 537, A106
- Rubele S., Girardi L., Kerber L., Cioni M.-R. L., Piatti A. E., Zaggia S., Bekki K., Bressan A., Clementini G., de Grijs R., Emerson J. P., Groenewegen M. A. T., Ivanov V. D., Marconi M., Marigo P., Moretti M.-I., Ripepi V., Subramanian S., Tatton B. L., van Loon J. T., 2015, *MNRAS*, 449, 639
- Rubele S., Pastorelli G., Girardi L., Cioni M.-R. L., Zaggia S., Marigo P., Bekki K., Bressan A., Clementini G., de Grijs R., Emerson J., Groenewegen M. A. T., Ivanov V. D., Muraveva T., Nanni A., Oliveira J. M., Ripepi V., Sun N.-C., van Loon J. T., 2018, *MNRAS*, 478(4), 5017
- Russell S. C., Dopita M. A., 1992, *ApJ*, 384, 508
- Sabbi E., Anderson J., Lennon D. J., van der Marel R. P., Aloisi A., Boyer M. L., Cignoni M., de Marchi G., de Mink S. E., Evans C. J., Gallagher, III J. S., Gordon

- K., Gouliermis D. A., Grebel E. K., Koekemoer A. M., Larsen S. S., Panagia N., Ryon J. E., Smith L. J., Tosi M., Zaritsky D., 2013, *AJ*, 146, 53
- Sabbi E., Lennon D. J., Anderson J., Cignoni M., van der Marel R. P., Zaritsky D., De Marchi G., Panagia N., Gouliermis D. A., Grebel E. K., Gallagher, III J. S., Smith L. J., Sana H., Aloisi A., Tosi M., Evans C. J., Arab H., Boyer M., de Mink S. E., Gordon K., Koekemoer A. M., Larsen S. S., Ryon J. E., Zeidler P., 2016, *ApJS*, 222, 11
- Salaris M., Cassisi S., 2006, *Evolution of Stars and Stellar Populations*
- Scargle J. D., 1982, *ApJ*, 263, 835
- Schneider F. R. N., Ramírez-Agudelo O. H., Tramper F., Bestenlehner J. M., Castro N., Sana H., Evans C. J., Sabín-Sanjulián C., Simón-Díaz S., Langer N., Fossati L., Gräfener G., Crowther P. A., de Mink S. E., de Koter A., Gieles M., Herrero A., Izzard R. G., Kalari V., Klessen R. S., Lennon D. J., Mahy L., Maíz Apellániz J., Markova N., van Loon J. T., Vink J. S., Walborn N. R., 2018a, *A&A*, 618, A73
- Schneider F. R. N., Sana H., Evans C. J., Bestenlehner J. M., Castro N., Fossati L., Gräfener G., Langer N., Ramírez-Agudelo O. H., Sabín-Sanjulián C., Simón-Díaz S., Tramper F., Crowther P. A., de Koter A., de Mink S. E., Dufton P. L., Garcia M., Gieles M., Hénauld-Brunet V., Herrero A., Izzard R. G., Kalari V., Lennon D. J., Maíz Apellániz J., Markova N., Najarro F., Podsiadlowski P., Puls J., Taylor W. D., van Loon J. T., Vink J. S., Norman C., 2018b, *Science*, 359, 69
- Schulz N. S., 2012, *The Formation and Early Evolution of Stars*
- Seale J. P., Looney L. W., Chu Y.-H., Gruendl R. A., Brandl B., Chen C.-H. R., Brandner W., Blake G. A., 2009, *ApJ*, 699, 150
- Seale J. P., Meixner M., Sewiło M., Babler B., Engelbracht C. W., Gordon K., Hony S., Misselt K., Montiel E., Okumura K., Panuzzo P., Roman-Duval J., Sauvage

- M., Boyer M. L., Chen C. H. R., Indebetouw R., Matsuura M., Oliveira J. M., Srinivasan S., van Loon J. T., Whitney B., Woods P. M., 2014, *AJ*, 148(6), 124
- Sembach K. R., Howk J. C., Ryans R. S. I., Keenan F. P., 2000, *ApJ*, 528, 310
- Shu F. H., Adams F. C., Lizano S., 1987, *Annu. Rev. Astron. Astrophys.*, 25, 23
- Skibba R. A., Engelbracht C. W., Aniano G., Babler B., Bernard J.-P., Bot C., Carlson L. R., Galametz M., Galliano F., Gordon K., Honny S., Israel F., Lebouteiller V., Li A., Madden S., Meixner M., Misselt K., Montiel E., Okumura K., Panuzzo P., Paradis D., Roman-Duval J., Rubio M., Sauvage M., Seale J., Srinivasan S., van Loon J. T., 2012, *ApJ*, 761, 42
- Skillman E. D., Terlevich R., Melnick J., 1989, *Mon. Not. R. astr. Soc.*, 240, 563
- Skrutskie M. F., Meyer M. R., Whalen D., Hamilton C., 1996, *AJ*, 112, 2168
- Skrutskie M. F., Cutri R. M., Stiening R., Weinberg M. D., Schneider S., Carpenter J. M., Beichman C., Capps R., Chester T., Elias J., Huchra J., Liebert J., Lonsdale C., Monet D. G., Price S., Seitzer P., Jarrett T., Kirkpatrick J. D., Gizis J. E., Howard E., Evans T., Fowler J., Fullmer L., Hurt R., Light R., Kopan E. L., Marsh K. A., McCallon H. L., Tam R., Van Dyk S., Wheelock S., 2006, *AJ*, 131, 1163
- Smith R. C., Points S. D., Chu Y.-H., Winkler P. F., Aguilera C., Leiton R., MCELS Team, 2005, *American Astronomical Society Meeting Abstracts*, *Bulletin of the American Astronomical Society* Vol. 37, p. 1200
- Solomon P. M., Rivolo A. R., Barrett J., Yahil A., 1987, *ApJ*, 319, 730
- Soszyński I., Udalski A., Szymański M. K., Kubiak M., Pietrzyński G., Wyrzykowski L., Szewczyk O., Ulaczyk K., Poleski R., 2009, *Acta Astronomica*, 59(3), 239
- Soszyński I., Pawlak M., Pietrukowicz P., Udalski A., Szymański M. K., Wyrzykowski L., Ulaczyk K., Poleski R., Kozłowski S., Skowron D. M., 2016, *Acta Astronomica*, 66(4), 405

- Spezzi L., de Marchi G., Panagia N., Sicilia-Aguilar A., Ercolano B., 2012, *MNRAS*, 421, 78
- Spezzi L., Petr-Gotzens M. G., Alcalá J. M., Jørgensen J. K., Stanke T., Lombardi M., Alves J. F., 2015, *A&A*, 581, A140
- Stahler S. W., Palla F., 2005, *The Formation of Stars*
- Stanimirović S., Staveley-Smith L., Jones P. A., 2004, *ApJ*, 604, 176
- Stankov A., Handler G., 2005, *ApJS*, 158, 193
- Stetson P. B., 1996, *PASP*, 108, 851
- Subramanian S., Subramaniam A., 2009, *A&A*, 496, 399
- Subramanian S., Rubele S., Sun N.-C., Girardi L., de Grijs R., van Loon J. T., Cioni M.-R. L., Piatti A. E., Bekki K., Emerson J., Ivanov V. D., Kerber L., Marconi M., Ripepi V., Tatton B. L., 2017, *Mon. Not. R. astr. Soc.*, 467(3), 2980
- Sun N.-C., de Grijs R., Subramanian S., Bekki K., Bell C. P. M., Cioni M.-R. L., Ivanov V. D., Marconi M., Oliveira J. M., Piatti A. E., Ripepi V., Rubele S., Tatton B. L., van Loon J. T., 2017a, *ApJ*, 849, 149
- Sun N.-C., de Grijs R., Subramanian S., Cioni M.-R. L., Rubele S., Bekki K., Ivanov V. D., Piatti A. E., Ripepi V., 2017b, *ApJ*, 835, 171
- Sun N.-C., de Grijs R., Cioni M.-R. L., Rubele S., Subramanian S., van Loon J. T., Bekki K., Bell C. P. M., Ivanov V. D., Marconi M., Muraveva T., Oliveira J. M., Ripepi V., 2018, *ApJ*, 858, 31
- Sutherland W., Emerson J., Dalton G., Atad-Ettedgui E., Beard S., Bennett R., Bezawada N., Born A., Caldwell M., Clark P., Craig S., Henry D., Jeffers P., Little B., McPherson A., Murray J., Stewart M., Stobie B., Terrett D., Ward K., Whalley M., Woodhouse G., 2015, *A&A*, 575, A25

- Tatton B. L., van Loon J. T., Cioni M.-R., Clementini G., Emerson J. P., Girardi L., de Grijs R., Groenewegen M. A. T., Gullieuszik M., Ivanov V. D., Moretti M. I., Ripepi V., Rubele S., 2013, *A&A*, 554, A33
- Teixeira G. D. C., Kumar M. S. N., Smith L., Lucas P. W., Morris C., Borissova J., Monteiro M. J. P. F. G., Caratti o Garatti A., Contreras Peña C., Froebrich D., Gameiro J. F., 2018, *A&A*, 619, A41
- Tielens A. G. G. M., 2010, *The Physics and Chemistry of the Interstellar Medium*
- Tout C. A., Livio M., Bonnell I. A., 1999, *MNRAS*, 310, 360
- Udalski A., Olech A., Szymanski M., Kaluzny J., Kubiak M., Mateo M., Krzeminski W., Stanek K. Z., 1997, *Acta Astronomica*, 47, 1
- Udalski A., Szymanski M. K., Soszynski I., Poleski R., 2008, *Acta Astronomica*, 58, 69
- Udalski A., Kubiak M., Szymanski M., 1997, *Acta Astronomica*, 47, 319
- Vallenari A., Chiosi E., Sordo R., 2010, *A&A*, 511, A79
- van der Marel R. P., Cioni M.-R. L., 2001, *AJ*, 122, 1807
- van der Marel R. P., 2006, in Livio M., Brown T. M., eds, *The Local Group as an Astrophysical Laboratory Vol. 17*, p. 47
- Vijh U. P., Meixner M., Babler B., Block M., Bracker S., Engelbracht C. W., For B., Gordon K., Hora J., Indebetouw R., Leitherer C., Meade M., Misselt K., Sewilo M., Srinivasan S., Whitney B., 2009, *AJ*, 137(2), 3139
- Vorobyov E. I., Basu S., 2010, *ApJ*, 719(2), 1896
- Ward J. L., Oliveira J. M., van Loon J. T., Sewilo M., 2017, *Mon. Not. R. astr. Soc.*, 464(2), 1512
- Ward-Thompson D., Whitworth A. P., 2015, *An Introduction to Star Formation*

Welty D. E., Xue R., Wong T., 2012, *ApJ*, 745(2), 173

Werner M. W., Roellig T. L., Low F. J., Rieke G. H., Rieke M., Hoffmann W. F., Young E., Houck J. R., Brandl B., Fazio G. G., Hora J. L., Gehrz R. D., Helou G., Soifer B. T., Stauffer J., Keene J., Eisenhardt P., Gallagher D., Gautier T. N., Irace W., Lawrence C. R., Simmons L., Van Cleve J. E., Jura M., Wright E. L., Cruikshank D. P., 2004, *ApJS*, 154, 1

Westerlund B., 1961, *Uppsala Astronomical Observatory Annals*, 5, 1

Whitney B. A., Sewilo M., Indebetouw R., Robitaille T. P., Meixner M., Gordon K., Meade M. R., Babler B. L., Harris J., Hora J. L., Bracker S., Povich M. S., Churchwell E. B., Engelbracht C. W., For B.-Q., Block M., Misselt K., Vijn U., Leitherer C., Kawamura A., Blum R. D., Cohen M., Fukui Y., Mizuno A., Mizuno N., Srinivasan S., Tielens A. G. G. M., Volk K., Bernard J.-P., Boulanger F., Frogel J. A., Gallagher J., Gorjian V., Kelly D., Latter W. B., Madden S., Kemper F., Mould J. R., Nota A., Oey M. S., Olsen K. A., Onishi T., Paladini R., Panagia N., Perez-Gonzalez P., Reach W., Shibai H., Sato S., Smith L. J., Staveley-Smith L., Ueta T., Van Dyk S., Werner M., Wolff M., Zaritsky D., 2008, *AJ*, 136, 18

Wofford A., Charlot S., Bruzual G., Eldridge J. J., Calzetti D., Adamo A., Cignoni M., de Mink S. E., Gouliermis D. A., Grasha K., Grebel E. K., Lee J. C., Östlin G., Smith L. J., Ubeda L., Zackrisson E., 2016, *Mon. Not. R. astr. Soc.*, 457(4), 4296

Wolk S. J., Rice T. S., Aspin C., 2013, *ApJ*, 773(2), 145

Wong T., Hughes A., Ott J., Muller E., Pineda J. L., Bernard J.-P., Chu Y.-H., Fukui Y., Gruendl R. A., Henkel C., Kawamura A., Klein U., Looney L. W., Maddison S., Mizuno Y., Paradis D., Seale J., Welty D. E., 2011, *ApJS*, 197, 16

Wright N. J., Parker R. J., Goodwin S. P., Drake J. J., 2014, *Mon. Not. R. astr. Soc.*, 438(1), 639

Wu T., Li Y., Deng Z.-m., 2018, *ApJ*, 867(1), 47

- Yasui C., Kobayashi N., Tokunaga A. T., Saito M., Tokoku C., 2010, *ApJL*, 723, L113
- Yasui C., Kobayashi N., Tokunaga A. T., Saito M., Izumi N., 2016, *AJ*, 151, 50
- Yorke H. W., 1986, *Annu. Rev. Astron. Astrophys.*, 24, 49
- Zaritsky D., Harris J., Thompson I. B., Grebel E. K., Massey P., 2002, *AJ*, 123, 855
- Zaritsky D., Harris J., Thompson I. B., Grebel E. K., 2004, *AJ*, 128, 1606
- Zeidler P., Preibisch T., Ratzka T., Roccatagliata V., Petr-Gotzens M. G., 2016, *A&A*, 585, A49
- Zhang Q., Fall S. M., 1999, *ApJL*, 527, L81
- Zinnecker H., Yorke H. W., 2007, *Annu. Rev. Astron. Astrophys.*, 45(1), 481
- Zinnecker H., McCaughrean M. J., Rayner J. T., Wilking B. A., Moneti A., 1993, in Klare G., ed., *Reviews in Modern Astronomy*, *Reviews in Modern Astronomy Vol. 6*, p. 191
- Zivkov V., Oliveira J. M., Petr-Gotzens M. G., Cioni M.-R. L., Rubele S., van Loon J. T., Bekki K., Cusano F., de Grijs R., Ivanov V. D., Marconi M., Niederhofer F., Ripepi V., Sun N.-C., 2018, *A&A*, 620, A143
- Zuckerman B., Palmer P., 1974, *Annu. Rev. Astron. Astrophys.*, 12, 279